


2008

## Design And Fabrication Of Chemiresistor Typemicro/nano Hydrogen Gas Sensors Usinginterdigitated Electrodes

Peng Zhang  
*University of Central Florida*

 Part of the [Mechanical Engineering Commons](#)  
Find similar works at: <https://stars.library.ucf.edu/etd>  
University of Central Florida Libraries <http://library.ucf.edu>

This Doctoral Dissertation (Open Access) is brought to you for free and open access by STARS. It has been accepted for inclusion in Electronic Theses and Dissertations, 2004-2019 by an authorized administrator of STARS. For more information, please contact [STARS@ucf.edu](mailto:STARS@ucf.edu).

---

### STARS Citation

Zhang, Peng, "Design And Fabrication Of Chemiresistor Typemicro/nano Hydrogen Gas Sensors Usinginterdigitated Electrodes" (2008). *Electronic Theses and Dissertations, 2004-2019*. 3705.  
<https://stars.library.ucf.edu/etd/3705>

# DESIGN AND FABRICATION OF CHEMIRESISTOR TYPE MICRO/NANO HYDROGEN GAS SENSORS USING INTERDIGITATED ELECTRODES

by

PENG ZHANG

B.S. Ocean University of China, 1998

M.S. University of Science and Technology of China, 2004

A dissertation submitted in partial fulfillment of the requirements  
for the degree of Doctor of Philosophy  
in the Department of Mechanical, Materials and Aerospace Engineering  
in the College of Engineering and Computer Science  
at the University of Central Florida  
Orlando, Florida

Fall Term  
2008

Major Professor: Hyoung Jin Cho

@2008 Peng Zhang

## ABSTRACT

Hydrogen sensors have obtained increased interest with the widened application of hydrogen energy in recent years. Among them, various chemiresistor based hydrogen sensors have been studied due to their relatively simple structure and well-established detection mechanism. The recent progress in micro/nanotechnology has accelerated the development of small-scale chemical sensors. In this work, MEMS (Micro-Electro-Mechanical Systems) sensor platforms with interdigitated electrodes have been designed and fabricated. Integrating indium doped tin dioxide nanoparticles, these hydrogen sensors showed improved sensor characteristics such as sensitivity, response and selectivity at room temperature. Design parameters of interdigitated electrodes have been studied in association with those sensor characteristics. It was observed that these parameters (gap between the electrodes, width and length of the fingers, and the number of the fingers) imposed different impacts on the sensor performance. In order to achieve small, robust, low cost and fast hydrogen micro/nano sensors with high sensitivity and selectivity, the modeling and process optimization was performed. The effect of humidity and the influence of the applied voltage were also studied. The sensors could be tuned to have high sensitivity ( $10^5$ ), fast response time (10 seconds) and low energy consumption (19 nW). Incorporating the developed sensor, a portable hydrogen instrument integrated with a micro sensor, display, sound warning system, and measurement circuitry was demonstrated based on the calibration data of the sensor.

This work is dedicated to my beloved family.

## ACKNOWLEDGMENTS

I wish to express the great appreciation to my supervisor, Dr. Hyoung Jin Cho, for providing me the opportunity to continue my study and research at UCF and advising me on various interesting projects during my research. Without his support and guide, this work would not have been possible.

I am very grateful to Dr. Sudipta Seal, and his former students, Dr. Satyajit Shukla, Dr. Sameer Deshpande and graduate student, Abihilash Vincent for the cooperation.

I also thank the former and current members in Nanofab and BioMEMS lab, Dr. Hyungseok Bang, Dr. Ghanashyam Londe, Andrea Wesser and Matthew Montgomery, for their assistance.

## TABLE OF CONTENTS

LIST OF FIGURES .....	viii
LIST OF TABLES .....	xiii
CHAPTER 1 INTRODUCTION .....	1
1.1 Hydrogen economy .....	1
1.2. Current status of hydrogen micro/nano sensors .....	3
1.2.1 Chemiresistor based hydrogen sensors .....	3
1.2.1.1 Tin dioxide based hydrogen sensors .....	3
1.2.1.2 Palladium based hydrogen sensors .....	6
1.2.1.3 Carbon nanotube based hydrogen sensors .....	9
1.2.1.4 Other sensing materials .....	10
1.2.2. Microelectronics based hydrogen sensors .....	11
1.2.2.1 Schottky diode hydrogen sensors .....	11
1.2.2.2 Field effect transistor hydrogen sensors .....	13
1.2.3 Surface acoustic wave based hydrogen sensors .....	16
1.2.4. Optical hydrogen sensors .....	18
1.2.5 Other types of hydrogen sensors .....	20
1.3 Electrical properties of SnO <sub>2</sub> and In-doped SnO <sub>2</sub> .....	21
1.3.1 Conduction models of SnO <sub>2</sub> .....	21
1.3.2 Fundamentals of the In-doped SnO <sub>2</sub> .....	28
1.3.2.1 Type of In-doped SnO <sub>2</sub> .....	29
1.3.2.2 Effects of In-doping on room temperature hydrogen sensing .....	30
CHAPTER 2 MODEL ANALYSIS OF MEMS HYDROGEN SENSORS .....	33
2.1 From macro to MEMS sensors .....	33

2.2 Working principle of In-doped SnO <sub>2</sub> hydrogen sensors .....	36
2.3 Theoretical analysis of the MEMS hydrogen sensor .....	39
2.3.1 Theoretical model of IDEs.....	40
2.3.2 Diffusion-reaction model of gas sensors.....	48
2.3.3 Model analysis on thin film micro-gap sensors .....	51
2.3.3.1 Sensitivity .....	51
2.3.3.2 Response time .....	55
2.3.4 Model analysis on thin film nano-gap sensor .....	56
CHAPTER 3 FABRICATION AND TESTING OF HYDROGEN MICRO SENSORS .....	61
3.1 Fabrication of micro sensors.....	61
3.2 Testing of the micro-gap sensors .....	65
3.2.1 Gap effect.....	68
3.2.2 Length effect .....	70
3.2.3 Width effect .....	71
3.2.4 Humidity effect.....	73
3.3 Portable Instrument.....	77
CHAPTER 4 NANO—GAP HYDROGEN SENSORS.....	81
4.1 Fabrication of nano-gap sensors .....	81
4.2 Testing of the sensor response .....	83
4.2.1 Sensitivity, repeatability and response time.....	83
4.2.2 Effect of the applied voltage .....	86
CHAPTER 5 CONCLUSION.....	100
APPENDIX: PUBLICATIONS.....	102
REFERENCES .....	105



## LIST OF FIGURES

Figure 1: Area of potential hydrogen detection: 1, Ambient/Garage, 2 Passenger compartment, 3 Fuel storage area & High-pressure piping, 4 Fuel cell system area, 5A Fuel cell oxidant outlet, 5B Vehicle exhaust [3].	2
Figure 2: Hydrogen sensors integrated with SnO <sub>2</sub> (a) nanobelt [15], (b) nanocomposite [16], (c) nanowire [18], and (d) nanocrystalline power [5].	5
Figure 3: Working principle of Pd nanowire hydrogen sensor [28].	8
Figure 4: The measurements (wiring) of FET based hydrogen sensors (a) for obtaining drain-source I-V characteristic with floating gate, (b) for obtaining response curves with given drain-source current or gate-source voltage [83].	14
Figure 5: Schematic representation of the SnO <sub>2</sub> single-nanobelt FET device [92].	16
Figure 6: Optical image of two sets of SAW hydrogen sensors and the schematic view of top and cross section of a SAW hydrogen sensor [95, 97].	17
Figure 7: Conduction models based on grain sizes and contacts with metals in SnO <sub>2</sub> thin film and the equivalent circuitries. $E_C$ is the minimum of the conduction band; $E_V$ the maximum of the valence band; $E_F$ the Fermi level; $L_D$ the Debye length [130].	24
Figure 8: Effect of the grain size on the conduction mechanism [131].	25
Figure 9: Neck control model for the porous large grain SnO <sub>2</sub> thin film: (a) $z_n > 2z_0$ and (b) $z_n < 2z_0$ [131].	27
Figure 10: (a) Carrier type vs. In/Sn ratio, (b) Carrier type vs. processing temperature [137].	30

Figure 11: Bulk hydrogen sensors. (i) fiber-glass board, (ii) Cu connectors, (iii) sensor areas: In-doped SnO <sub>2</sub> thin films on Pyrex glass substrates (iv) Ag-electrodes with the gap of 1 cm, and (v) Cu-connectors for the heater-circuit (for high temperature testing, not used) [140].	33
Figure 12: Sensitivity of In-doped SnO <sub>2</sub> macro sensors (a) in high concentration, (b) in ppm level [138].	34
Figure 13: First generation MEMS sensors. (a) packaged sensor platform. (i) interdigitated electrodes (ii) resistive temperature sensor to monitor the temperature. (b) multicycle tests. (c) the individual cycle with a sensing signal reaching a saturated value [134].	35
Figure 14: Working principle of the In <sub>2</sub> O <sub>3</sub> doped SnO <sub>2</sub> hydrogen sensors.	36
Figure 15: Relationship of the response time ( $t_{90}$ ) and the sensitivity	38
Figure 16: Schematic view of IDEs (top view). g is the gap. w, the width, l, the length of the fingers and N, the number of electrodes.	40
Figure 17: A cross-section view of x-y plane with a pair of IDEs placed (a) at the bottom with applied voltage of $V_0$ , (b) on side, and (c) on top of the sensing layer.	41
Figure 18: Potential ( $V_a(x,y)$ ) distribution on IDEs with 10 $\mu\text{m}$ in gap, 50 $\mu\text{m}$ in width and applied voltage ( $V_0$ ) of 2 volts at various heights (distance from the electrode surface in y direction).	43
Figure 19: Electric field ( $E_a(x,y)$ ) distribution on IDEs with 10 $\mu\text{m}$ in gap , 50 $\mu\text{m}$ in width and applied voltage ( $V_0$ ) of 2 volts at various heights.	44
Figure 20: Distribution of surface charge density $\sigma(x)$ on IDEs with 10 $\mu\text{m}$ in gap and 50 $\mu\text{m}$ in width and applied voltage ( $V_0$ ) of 2 volts.	44
Figure 21: Current fraction in the sensing layer as a function of a thickness of t.	46

Figure 22: Schematic view of the current distribution in the sensing film. ....	47
Figure 23: Numerical calculation results on (a) gas concentration inside the sensing film and (b) effects of the electrode gap on fraction change conductance of the sensing film [6]. ....	51
Figure 24: (a) Schematic view of the micro-gap sensor. $E_a$ and $E_b$ are the electric fields above and between the electrodes, respectively. (b) equivalent circuitry. ....	52
Figure 25: Electric field distribution in the 120 nm thin film on top of the electrodes. $g$ and $w$ are 5 $\mu\text{m}$ and 50 $\mu\text{m}$ , respectively. ....	53
Figure 26: Schematic view of a one-dimension conduction model of the hydrogen sensor. $N_p$ and $R_g$ are the number of the nanoparticles and resistance at each grain-grain boundary, respectively. ....	53
Figure 27: Total resistance change Vs. the resistance change of the first layer in $\Delta t$ . ....	56
Figure 28: Schematic view of the nano-gap sensors with an electrode thickness ( $t_{\text{Au}}$ ) of 50 nm and a sensing film thickness of 120 nm. Sensing film with a thickness of 70 nm is on top of the IDEs. ....	57
Figure 29: Electric field distribution above the IDEs with 5 nm in gap and 5 nm in width. ....	57
Figure 30: Electric field above the electrodes with 100 nm and in gap 1000nm in width. ....	58
Figure 31: Current fraction in the layer with thickness of $t$ . ....	59
Figure 32: Fabrication steps: (a) Si wafer cleaning, (b) Thermal oxidation, (c) Au/Cr deposition, (d) Electrode patterning, (e) Nanoparticle deposition, and (f) Packaging. ....	62
Figure 33: AFM image of In-doped $\text{SnO}_2$ nanoparticles on the sensor surface. ....	64
Figure 34: Packaged sensors showing interdigitated electrodes. ....	65

Figure 35: (a) Schematic illustration of a test setup for hydrogen sensors and (b) software interface for control and measurement. ....	66
Figure 36: A typical testing result of a MEMS hydrogen sensor. The gap, length and width of fingers are 5 $\mu\text{m}$ , 1000 $\mu\text{m}$ , and 50 $\mu\text{m}$ , respectively.....	67
Figure 37: Effect of the electrode gap on the sensitivity of the micro-gap sensors.....	68
Figure 38: Effect of the electrode gap on the response time.....	70
Figure 39: Effect of the electrode length on the sensitivity. ....	71
Figure 40: Effect of sensor electrode length on the response time. ....	71
Figure 41: Initial resistance change in vacuum and humidity. ....	75
Figure 42: Humidity effect on PMMA coated and uncoated sensors.....	76
Figure 43: Comparison of the sensors with and without PMMA coating. ....	77
Figure 44: MEMS sensors fabricated for a portable hydrogen instrument (a) View of the wafer lever (b) a signal diced chip (c) enlarged IDEs (d) a packaged sensor with the size of 3 mm $\times$ 3 mm. ....	78
Figure 45: Sensor testing for portable instrument.....	78
Figure 46: Portable H <sub>2</sub> detecting instrument with a H <sub>2</sub> microsensor inside. ....	80
Figure 47: Fabrication steps of nano-gap sensors: (a) SiO <sub>2</sub> grown, (b) fabrication of contact pads, (c) e-beam writing, (d) Au/Cr deposition and lift-off, (e) protection layer coating, (f) In-doped SnO <sub>2</sub> coating, and (g) lift-off and wire-bonding.....	82
Figure 48: SEM images of PMMA patterns (a) in detail and (b) overview, and images of Au/Cr electrodes (c) in detail and (d) overview.....	83
Figure 49: Resistance variation of the 200-nm gap hydrogen sensor in response to 900 ppm hydrogen at room temperature. ....	84
Figure 50: Effect of gap size on the sensitivity of the nano-gap sensors.....	85

Figure 51: Multi-circle testing to test the repeatability of the nano-gap sensors in 900 ppm H <sub>2</sub> at room temperature. ....	85
Figure 52: Effect of applied voltage on the sensor performance (a) resistance change and (b) sensitivity change with applied voltages.....	87
Figure 53: Sensitivity change with applied voltages on a 200 nm-gap sensor. ....	88
Figure 54: Changes of Initial resistance of nano-gap sensors with applied voltages. ....	89
Figure 55: I/V curves of the 100-nm gap sensor (a) before exposed to H <sub>2</sub> (in Air) and (b) in H <sub>2</sub> . ....	90
Figure 56: A proposed model based on the Schottky diode assumption. The electrode/material interfaces are considered as Schottky diodes and the sensing film (In-doped SnO <sub>2</sub> ) is considered as a uniform varistor. $V_{\text{Forw}}$ , $V_m$ and $V_{\text{Rev}}$ are the potential drop over the left Schottky diode (D <sub>1</sub> ), the sensing material and the right Schottky diode (D <sub>2</sub> ), respectively. $V$ is the applied voltage. $R_b$ is the bulk resistance of In-doped SnO <sub>2</sub> . $\rho$ is the resistivity of In-doped SnO <sub>2</sub> . $g$ and $A$ are the gap and area of the cross-section, respectively. ....	91
Figure 57: Sensitivity as a function of applied voltages: (a) experimental result of 100-nm gap sensor and (b) analytical prediction based on equation 4.14. ....	96
Figure 58: Sensitivity as a function of a gap parameter: (a) experimental result of micro sensors and (b) analytical prediction based on equation 4.14, where, $x = K\rho_g g$ , the variable $x$ contains electrode gap ( $g$ ) and the constants $K$ and $\rho_g$ for given material and testing conditions. ....	98

## LIST OF TABLES

Table 1 Sensitivity and resistances of 5 $\mu\text{m}$ gap sensors with various width. ....	73
Table 1 Sensitivity and response time of 100 nm gap sensors .....	89

## CHAPTER 1 INTRODUCTION

### 1.1 Hydrogen economy

Current issues of global warming, air pollution and energy consumption have drawn wide public attention. Carbon dioxide (CO<sub>2</sub>), the main greenhouse gas, contributes most of the observed increase in globally averaged temperature, which is expected to cause sea level elevation, an increased frequency of extreme weather events, and a retreat of the glaciers in the arctic sea. In 2006, the emission of CO<sub>2</sub> was 5,890 million metric tons and will be as high as 6,851 million metric tons in 2030 in the United State [1]. According to Ref [2], one-third of CO<sub>2</sub> emission is from transportation. The use of fossil based fuel not only generates greenhouse gas, but also significantly degrades air quality. It has been reported that about 50% people in USA suffer from high levels of air pollutants that affect public health and the environment [2]. At the same time, the demand of energy is growing rapidly since the mid-1990s and the outlook of fossil fuel supplies is dismal. This discrepancy promoted a public and private spending increase and started imposing a huge burden to economic growth recently.

All these concerns drive the expanded use of hydrogen energy as a promising candidate for a next generation clean energy source. Hydrogen energy is renewable and pollution-free. Hydrogen can be extracted from numerous available sources, for example, water by electrolysis. By-products of hydrogen energy are just water vapor and heat, not CO<sub>2</sub> or any other air pollutants. Due to these benefits, hydrogen powered products have been actively developed. One good example is hydrogen fuel cell powered vehicles. In 2007, Honda

unveiled the FCX Clarity, the first production model. Obviously, use of hydrogen powered vehicles could reduce the greenhouse gas emission and improve air quality.

However, safety issues are one of the main challenges in the development of hydrogen energy. Hydrogen itself is colorless, odorless and explosive. Hydrogen can be ignited easily with a very small amount of energy, as small as 0.02 mJ. The explosive range is wide, from 4% to 75%, and the hydrogen flame is invisible. Therefore, hydrogen sensors or detectors are needed to rigorously monitor the hydrogen leak for safe applications of hydrogen energy. Figure 1 shows hydrogen sensor locations for a hydrogen fuel cell vehicle [3].

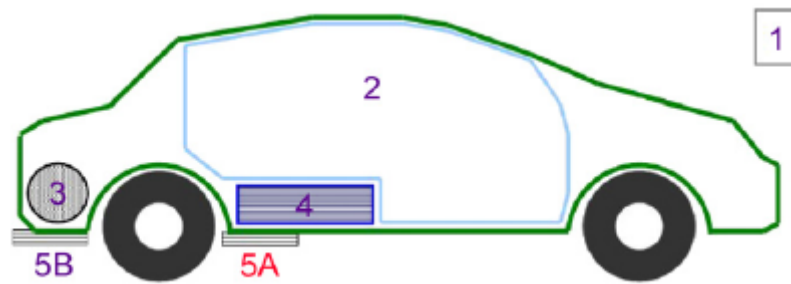


Figure 1:Area of potential hydrogen detection: 1, Ambient/Garage, 2 Passenger compartment, 3 Fuel storage area & High-pressure piping, 4 Fuel cell system area, 5A Fuel cell oxidant outlet, 5B Vehicle exhaust [3].

At least five hydrogen sensors are required to be installed in a car to monitor the hydrogen leak suggested by The Canadian Hydrogen Safety Program (CHSP) [3]. Miniaturized, robust and low cost hydrogen sensors with high sensitivity and fast response are in great demand for these preventive warning systems.



## 1.2. Current status of hydrogen micro/nano sensors

A variety of hydrogen sensors have been studied recently. Based on the detection mechanism, there are four main types of hydrogen sensors: chemiresistor based sensors, microelectronics based sensors, surface acoustic wave based sensors, and optical sensors.

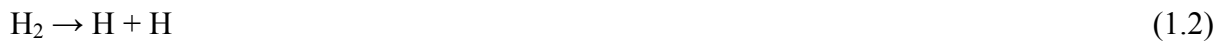
### 1.2.1 Chemiresistor based hydrogen sensors

Chemiresistor hydrogen sensors detect hydrogen by monitoring the resistance change of the sensing materials. The basic structure of the sensors is relatively simple including electrodes with sensing materials on top of or between them (sensors working at elevated temperature have extra heating elements). Sensors do not require specialized or complex measurement system. Currently, most of the hydrogen micro/nano sensors are based on this chemiresistor type. A variety of sensing materials have been developed including metal oxide semiconductor (MOS), metal, carbon nanotube (CNT), polymer and others. Applying nanotechnology, sensors integrated with nanostructured materials have been increasingly reported.

#### 1.2.1.1 Tin dioxide based hydrogen sensors

Tin dioxide ( $\text{SnO}_2$ ) is the most popular hydrogen sensing material. Its sensing mechanism has been extensively studied. In principle, when the  $\text{SnO}_2$  is exposed to air, the oxygen molecules absorbed on the surface change to  $\text{O}_2^-$  and/or  $\text{O}^-$  by picking up the electrons from the conduction band of  $\text{SnO}_2$  [4]. With the assistance of high temperature or catalysts (such as Au, Pd and Pt), hydrogen gas introduced on the  $\text{SnO}_2$  surface becomes

dissociated. Hydrogen atoms react with adsorbed oxygen ions, releasing water and electrons. These free electrons contribute to the conductivity of the sensing material. The reactions can be summarized as [4]:



The early hydrogen sensors using pure SnO<sub>2</sub> showed low sensitivity, slow response, poor selectivity, and in most cases worked only at high temperature. Surface modification and doping have been applied to improve the performance of the SnO<sub>2</sub> hydrogen sensors [5-13]. The doping materials include palladium (Pd) [9-11], platinum (Pt) [7, 9], gold (Au) [9], phosphorus (P) [9], boron (B) [9], indium (In) [5, 12], aluminum (Al) [12], erbium (Er) [12], yttrium (Y) [12], antimony (Sb) [12], niobium (Nb) [12], cobalt (Co) [12], nickel (Ni) [13], iron (Fe) [13], Copper (Cu) [13] silver (Ag) [13]. Among them, Pt [7, 9] and Pd [10] doping showed improvements in sensitivity and/or selectivity at high temperatures. In-doped SnO<sub>2</sub> sensors [6] could be made to work at room temperature with high sensitivity and fast response. The small size has proved to help improve the sensitivity and response time because of the large surface to volume ratio [4]. For SnO<sub>2</sub>, especially when the critical size is comparable to the Debye length, the rapid transduction from surface reaction leading to measurable resistance change could be achieved [14]. Sensors based on SnO<sub>2</sub> nanoparticles [4, 6], nanobelts [15], nanocomposites [5, 16] and nanowires [17] were reported, showing enhanced sensitivity and response time. Figure 2 shows SnO<sub>2</sub> hydrogen sensors with various platforms [5, 15, 16, 18].

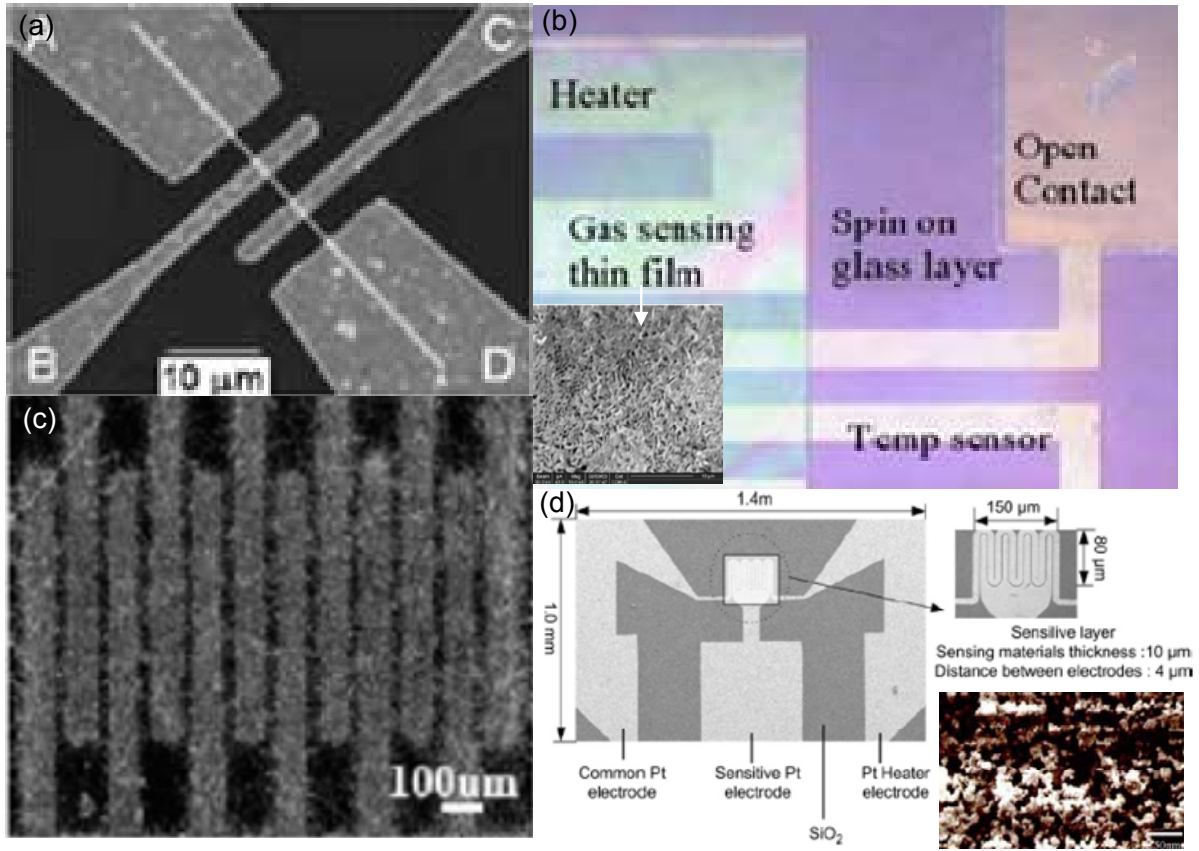


Figure 2: Hydrogen sensors integrated with SnO<sub>2</sub> (a) nanobelt [15], (b) nanocomposite [16], (c) nanowire [18], and (d) nanocrystalline power [5].

Figure 2 (a) shows the sensor based on a single SnO<sub>2</sub> nanobelt. The four electrodes were used to measure the contact resistance at the interface of the SnO<sub>2</sub> nanobelt and Pt electrodes. In the hydrogen sensing test, only two of them were used. The device could sense hydrogen at room temperature with power consumption as low as 10 nW, but the sensitivity is less than 0.8 [15]. Figure 2 (b) shows the hydrogen detector integrated with the heater, temperature sensor and SnO<sub>2</sub> thin film embedded with single wall carbon nanotubes (SWCNTs). These embedded SWCNTs provided the nanopasses assisting hydrogen diffusion and enhanced the sensitivity [16]. Figure 2 (c) shows the SnO<sub>2</sub> nanowire grown on top of the interdigitated electrodes with a 20 μm gap. The sensor could detect 10 ppm H<sub>2</sub> with a sensitivity of 0.4 at

300 °C [18]. Figure 2 (d) shows the sensor with nano-crystalline  $\text{SnO}_2\text{--Ag}_2\text{O--PtO}_x$ . The sensor used a common electrode for both heating and measurement to simplify the fabrication.  $\text{Ag}_2\text{O}$  acted as adsorption sites at high temperature to pick up electrons from  $\text{SnO}_2$ . When  $\text{H}_2$  was present,  $\text{Ag}_2\text{O}$  was reduced to Ag and released electrons contributing to conductance.  $\text{PtO}_x$  was supposed to interact with  $\text{SnO}_2$  to produce an extra electron deficient space charge layer which would enhance the gas sensitivity [5].

#### 1.2.1.2 Palladium based hydrogen sensors

Palladium (Pd) has an extraordinary ability to absorb (or dissolve into itself) hydrogen. When the hydrogen gas gets dissociated to hydrogen atoms on the Pd surface, these hydrogen atoms diffuse into the Pd to form a solid solution of Pd/H. Hydrogen absorption in Pd results in lattice expansion, and a consequent increase in volume and resistance. When hydrogen gas is removed from the ambient, hydrogen atoms diffuse to the surface and recombine to form hydrogen molecules, which desorb from the surface, causing a recovery in resistance. It is believed that the resistance of Pd increases linearly with hydrogen concentration, which can be utilized to monitor hydrogen [19]. For the bulk (dense) Pd, the change in resistance is small, limiting the sensitivity of these sensors. Although nanoporous Pd film with a large surface to volume ratio was developed to improve the detection range and sensitivity, the sensitivity is still low (less than 0.2) [20]. In order to reduce the consumption of expensive Pd and to improve the physicochemical strength and resistance to poisoning by other chemical species, Pd alloys are used to replace pure Pd as the sensing materials. Sensors based on Pd-Cr [21], Pd-Cu [21], Pd-Al [21], Pd-Mg [21-22], Pd-Ni [23-25], Pd-Ag [26], Pd-Au [27] were explored, which showed improved sensitivity.

The first Pd nanowire hydrogen sensor was reported based on the swelling property (volume increase) of Pd in Science in 2001 [28]. The nanowires were prepared by electrodeposition on graphite substrates. As shown in Fig. 3 [28], when hydrogen is presented and dissolved into Pd, the hydrogen-swollen Pd grains expended to “close” the nano-scale gaps in-between. The grain chains connected and provided a current pass that decreased the resistance of the Pd nanowires. These gaps “re-opened” when the Pd grains in the nanowire returned to their equilibrium dimensions in the absence of hydrogen. Atomic force microscopy (AFM) images provided direct evidences of the “open” and “closed” behaviors of Pd nanowires with and without hydrogen and confirmed this “break junction” mechanism [28]. The sensor current changed between approximately 1000 nA (closed gaps) and 10 nA (open gaps), showing the “switch” characteristic with 75 millisecond response time and high sensitivity. Control of the size of the nano-gap is complex, and this type of sensors can only work for high concentration hydrogen (1% and above) detection, which might limit its application.

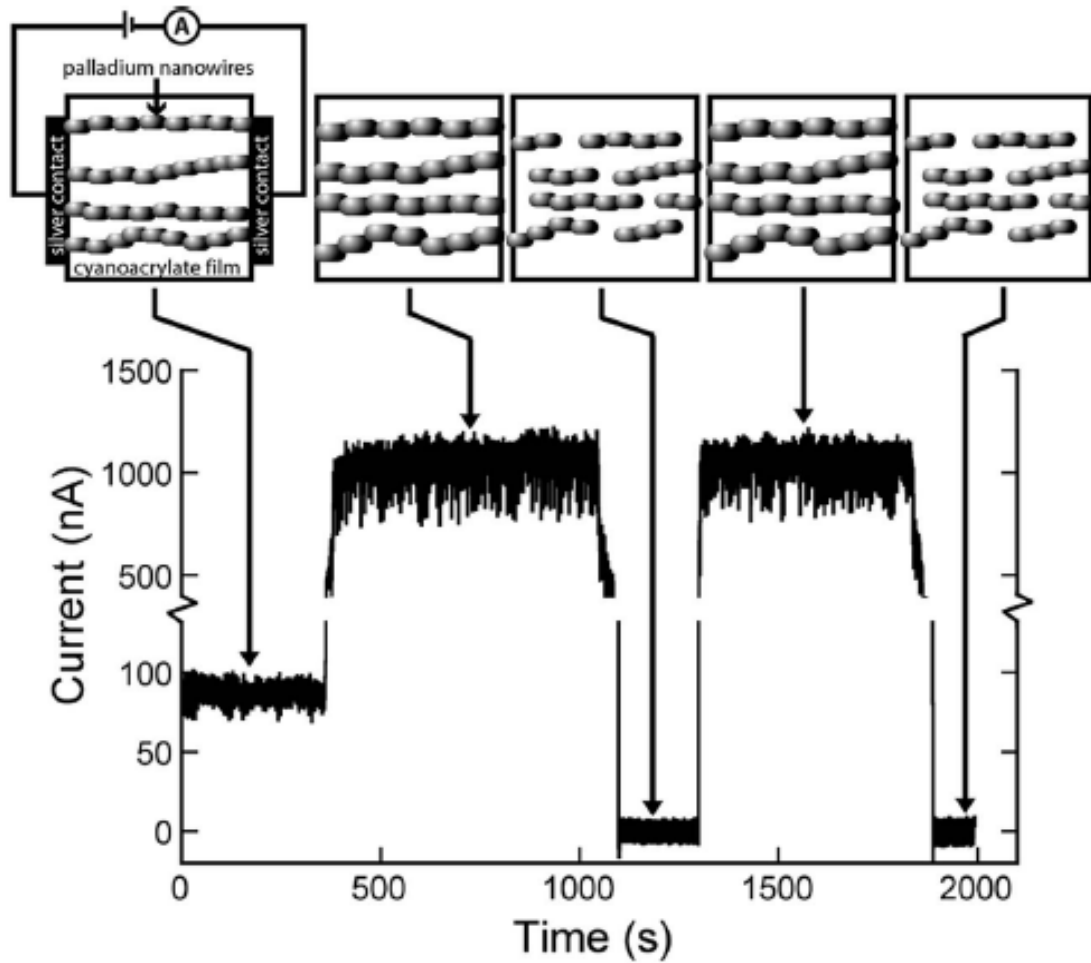


Figure 3: Working principle of Pd nanowire hydrogen sensor [28].

A Pd nanocluster hydrogen sensor based on tunneling mechanism was developed, in which the conductance of the sensor was controlled by both the tunneling phenomenon and the swelling property of Pd in hydrogen [29]. Pd nanoclusters were fabricated and controlled by sputtering and in-suit resistance measurement. The sensor did not show the “switch” feature of the Pd nanowire sensor, though the fabrication was simplified.

A vertical Pd nanowire sensor was fabricated by using anodized aluminum oxide (AAO) template and growing Pd through it. The size of the nanowires and the gap in-between were controlled by the pore dimension of AAO, typically 80 nm in diameter and 3-5 nm in gap.

The sensing mechanism is based on the swelling effect of Pd and the sensor showed a fast response time of 70 milliseconds in high concentration hydrogen (1%) [30].

#### 1.2.1.3 Carbon nanotube based hydrogen sensors

Carbon nanotube (CNT) has attracted research interest intensively since its discovery in 1991 [31] due to its unique structure and properties. CNT is sensitive towards changes in their local chemical environment because interactions between CNT and target molecules can significantly change the electronic properties of CNT [31]. This chemical sensitivity has made CNT suitable for chemical sensors. CNT shows the sensitivity to gases [32] such as ammonia ( $\text{NH}_3$ ), nitrogen dioxide ( $\text{NO}_2$ ), methane ( $\text{CH}_4$ ), carbon monoxide ( $\text{CO}$ ), sulfur dioxide ( $\text{SO}_2$ ), hydrogen sulfide ( $\text{H}_2\text{S}$ ), and oxygen ( $\text{O}_2$ ). For  $\text{H}_2$  detection, bare CNT does not exhibit appreciable sensitivity, so surface modification of CNT has been performed by integrating  $\text{H}_2$  sensing materials [33-38]. The most promising candidate is Pd due to its catalytic nature and feature of dissolving hydrogen. By dissolving hydrogen, the work function of Pd becomes low. Electrons transfer from Pd to p-type semiconductor CNT and reduce the density of the hole-carriers resulting increased resistance [36]. The resistance could recover when hydrogen atoms diffuse to the surface, react with oxygen and release water. Pd functionalization resulted in the dramatic increase of the sensing capability of CNT based sensors toward hydrogen molecules and could detect 10 ppm hydrogen gas at room temperature. Nevertheless most of them showed low sensitivity less than 1. Both single wall carbon nanotube (SWNT) [33, 35, 36-40] and multiwall carbon nanotube (MWNT) [34, 41] based hydrogen sensors have been developed. SWNT hydrogen sensors have better performance compared to MWNT hydrogen sensors while preparation of MWNT is easier.

The advantages of CNT (SWNT and MWNT) hydrogen sensors are attributed to CNT's high surface to volume ratio. In addition, CNT itself is chemically inert, which means the initial resistances of CNT based hydrogen sensors are more stable compared to other chemiresistor based sensors.

#### 1.2.1.4 Other sensing materials

Zinc oxide (ZnO) is another attractive hydrogen sensing material. Sensors based on the ZnO nanobelts [42], nanopillars (vertical nanorods) [43], nanorods [44-45], nanoparticles [46] were developed. The sensing behavior of ZnO is similar to that of SnO<sub>2</sub>: Surface absorbed oxygen traps electrons from the conduction band of ZnO and releases electrons when hydrogen presents contributes to conductivity change.

Titania (TiO<sub>2</sub>) nanotube based sensors show the distinguished advantage of self-clearing and high sensitivity [47-51]. TiO<sub>2</sub> is an n-type semiconductor and could generate electron-hole pairs by absorbing ultraviolet light, which induces the redox reactions that clean the surface by dissociating contaminates to CO<sub>2</sub> and water [47]. This photocatalytic property results in the self-clean ability. TiO<sub>2</sub> nanotubes with Pd catalysts showed the sensitivity of 10<sup>7</sup> at room temperature in 1,000 ppm hydrogen [48]. This was explained by both the intrinsic resistance of TiO<sub>2</sub> and the barrier height at the interface with the presence of H<sub>2</sub>. Further research from the same group indicated that this giant sensitivity might due to the Ti layer underneath the TiO<sub>2</sub> nanotube because the TiO<sub>2</sub> nanotube without metal layer underneath showed sensitivity of 10<sup>4</sup> instead of 10<sup>7</sup> in the same testing conditions [49]. One challenge of fabricating nanotube based micro sensors is the integration of the measurement



electrodes. TiO<sub>2</sub> nanotubes are brittle and a small force can easily break them. This makes the fabrication steps incompatible with current IC or MEMS fabrication process.

Other hydrogen sensing materials such as the Pd-decorated Si nanowire [52] and nanoporous Si [53], Pd-coated gallium nitride (GaN) nanowire [54], nanocrystalline tungsten oxide (WO<sub>3</sub>) [55], conductive polymers (polypyrrole nanofiber [56], polyaniline nanofiber [57], and pyridylimidazopyrrole or pyridylimidazonaphthalene [58]) were also explored and reported for the improved sensor performance.

### 1.2.2. Microelectronics based hydrogen sensors

#### 1.2.2.1 Schottky diode hydrogen sensors

Schottky diodes are a device based on the metal-semiconductor junction as the Schottky barrier. Current/voltage (I/V) characteristic of a Schottky diode depends on the work function of the metal, band gap, type (n-type or p-type), main carrier concentration of the semiconductor, and others. In other words, it depends on the Schottky barrier height. I/V relationship are given as [59-60]:

$$I = I_0 \exp\left(\frac{qV}{\eta kT}\right) \left[1 - \exp\left(-\frac{qV}{kT}\right)\right] \quad (1.4)$$

$$I_0 = A A^{**} T^2 \exp\left(-\frac{q\phi_b}{kT}\right) \quad (1.5)$$

$$A^{**} = \frac{4\pi q k^2 m_n^*}{\eta^3} = 120 \left(\frac{m_n^*}{m_n}\right) \quad (1.6)$$

where  $I$  is the forward-biased conducting current,  $I_0$ , the reverse saturation current,  $\eta$ , the ideality factor,  $V$ , the applied voltage,  $A$ , the Schottky contact area,  $A^{**}$ , the effective Richardson constant,  $k$ , the Boltzmann constant,  $T$ , the absolute temperature,  $m_n^*$  and  $m_n$ , the electron effective mass and free electron mass in the vacuum, respectively.

$I_0$  and  $\eta$  can be determined from interception and the slope of  $\ln(I)$  versus  $V$  plot. When  $V$  is larger than  $3kT/q$  (0.077V at 300 K), the Schottky barrier height  $\Phi_b$  can be derived from Equation 1.5 as:

$$\phi_b = \frac{kT}{q} \ln \left( \frac{AA^{**}T^2}{I_0} \right) \quad (1.7)$$

From these equations, it is concluded that the current is controlled by Schottky contact area ( $A$ ), applied voltage ( $V$ ), temperature ( $T$ ) and the Schottky barrier height ( $\Phi_b$ ).

Schottky diodes with a catalytic metal have been studied extensively in hydrogen sensing with the advance of the semiconductor technology. In principle, hydrogen molecules are first dissociated and adsorbed on the catalytic metal. Then, the hydrogen atoms penetrate through the metal thin film to the metal-semiconductor interface. Hydrogen atoms are polarized which causes a dipolar layer when a bias voltage is applied; thus an excess of charge states at the interface is generated and the effective Schottky barrier height is reduced. Current/voltage ( $I/V$ ) characteristics represent the change in Schottky barrier height, which is strongly related to the hydrogen concentration. Based on this mechanism, the  $I/V$  characteristics are used to monitor the hydrogen leak [13]. Various material pairs were investigated in the Schottky diode hydrogen sensors, such as Pd/SiC [61], Pd/InP [62-63], Pt/SiC [64], Pt/In<sub>0.5</sub>Al<sub>0.5</sub>P [65], Ni/n-Si [66], Pd/GaN [6-70], Pt/GaN [71], Pd/AlGaN [72],

Pt/AlGaIn/GaN [73], Au-ZnO [74], and such sensors exhibited improved sensitivity and response time. If the sensors work at high temperature and /or are used for a long time, there might be reactions between the metal and semiconductor which could induce a shift in the I/V curve [75]. This shift might cause the wrong sensing signals. To overcome this drawback, the metal-insulator-semiconductor (MIS) or metal-oxide-semiconductor (MOS) structure was developed [59-60, 75-82]. Studies showed that the thin layer of oxide or insulator improved not only the thermal (chemical) stability of the diodes, but also the sensitivity [80-82]. The introduction of the oxide or insulator structure increased the Schottky barrier height between the metal and semiconductor [81] and provided the adsorption sites for atomic hydrogen at the metal/insulator (oxide) interface [82]. Formation of the hydrogen-induced dipole layer could reduce the Schottky barrier height more effectively and enhance the sensitivity.

#### 1.2.2.2 Field effect transistor hydrogen sensors

Field effect transistor (FET) based hydrogen sensors are similar in structure to conventional FET devices, except that catalytic materials such as Pt and Pd are used as the gate electrode. When introduced onto the gate electrode, hydrogen atoms penetrate through the electrode and accumulate at the interface of the metal and semiconductor (or the interface of metal and oxide layer), leading to a change in the electronic properties of the gate contact, such as the work function of the electrode material. This process is the same as that of the Schottky diodes hydrogen sensor. The property change of the gate contact induces variation of the depletion region at the gate/semiconductor interface [83], or the width (shape) of the current channel between drain and source, and hence the output of the device. There are a

couple of different methods to monitor the hydrogen induced changes, as shown in Fig.4 [83].

Figure 4 shows two wirings of the FET based sensors to obtain different corresponding signals. In Fig. 4 (a), the drain is given a positive bias, the source is grounded, and the gate is floating. The hydrogen induced change could be monitored by measuring the I/V curves [83-85]. In Fig. 4 (b), the constant current between the drain and source is maintained. Hydrogen could be monitored by measuring the voltage change between the gate and source [83, 86-88] or by obtaining the common source output (I/V) characteristics with a given gate voltage [89-94].

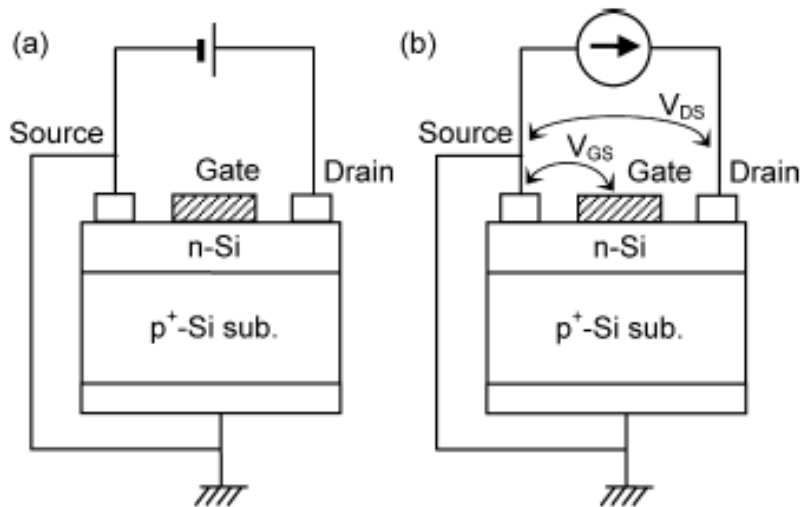


Figure 4: The measurements (wiring) of FET based hydrogen sensors (a) for obtaining drain-source I-V characteristic with floating gate, (b) for obtaining response curves with given drain-source current or gate-source voltage [83].

Keiji Tsukada [84] developed a Pd-Nafion-Pt- FET based hydrogen sensor which monitored hydrogen by measuring hydrogen induced change of the Pt work function. The

FET served as a transducer which transformed the shift of the work function into the corresponding signal output. In principal, dissociated hydrogen atoms passed thorough the Pd and Nafion film, which could block the electrons coming from the Pd film causing them to accumulate on the Pt gate surface and thus change the Pt work function. A voltage-follower-circuit was used to maintain a constant drain-source voltage and current. The output voltage change of the circuit equaled to the Pt work function change as the hydrogen sensing signal. The advantages of the sensor are low testing limit of 1 ppm and self-checking (The output signal can be modulated by changing the bias frequency).

P. Andrei et. al. [92] presented a  $\text{SnO}_2$  single-nanobelt based FET device. The schematic view of the device is shown in Fig. 5. It is similar in structure to a back-gated metal-oxide-semiconductor field-effect transistor (MOSFET) with metal-to-semiconductor interface (drain and source). The  $\text{SnO}_2$  nanobelt provided the current channel which was controlled by the gate voltage. The interesting testing and calculation results showed the sensor behaved like a linear resistor ( $I_{\text{ds}}$  was proportional to  $V_{\text{ds}}$ .  $I_{\text{ds}}$  and  $V_{\text{ds}}$  are the drain to source current and voltage, respectively) in the hydrogen environment. In this case, the device became two Schottky diodes connected back-to-back with a series resistance from the  $\text{SnO}_2$  nanobelt separating the diodes. The entire resistance was controlled by the source and drain Schottky contacts, which imply highly sensitive hydrogen sensor could be built based on the metal oxide semiconductor Schottky contacts.

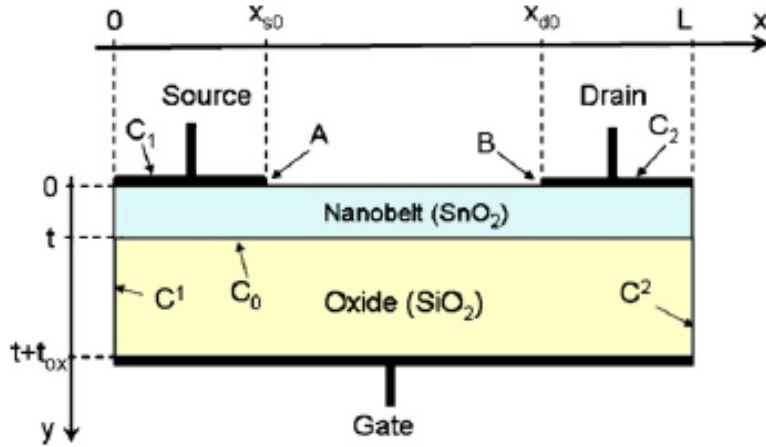


Figure 5: Schematic representation of the SnO<sub>2</sub> single-nanobelt FET device [92].

### 1.2.3 Surface acoustic wave based hydrogen sensors

In a surface acoustic wave (SAW) device, the change in electrical conductivity of the sensing layer perturbs the velocity of the propagating acoustic wave due to the acoustoelectric effect. The center frequency of a SAW device is given by the equation [95]:

$$v = f \cdot p \quad (1.8)$$

where  $v$  is the surface wave velocity,  $f$  the resonant frequency, and  $p$  the interdigitated transducer period.

The variation in velocity can be monitored by measuring the changes in resonant frequency of the SAW device. For the SAW based hydrogen sensor with the hydrogen sensing layer on top, adsorbed hydrogen atoms act as dipoles at the sensing film/substrate interface and modulate the conductance of the interface. These variations in the interface conductivity can cause a considerable fluctuation in the SAW velocity, which finally leads to a modification of the measuring frequency and differential frequency. The change in

frequency is proportional to the concentration of hydrogen present in the environment and could be used to detect hydrogen [96]. Figure 6 shows a SAW based hydrogen sensor [95, 97].

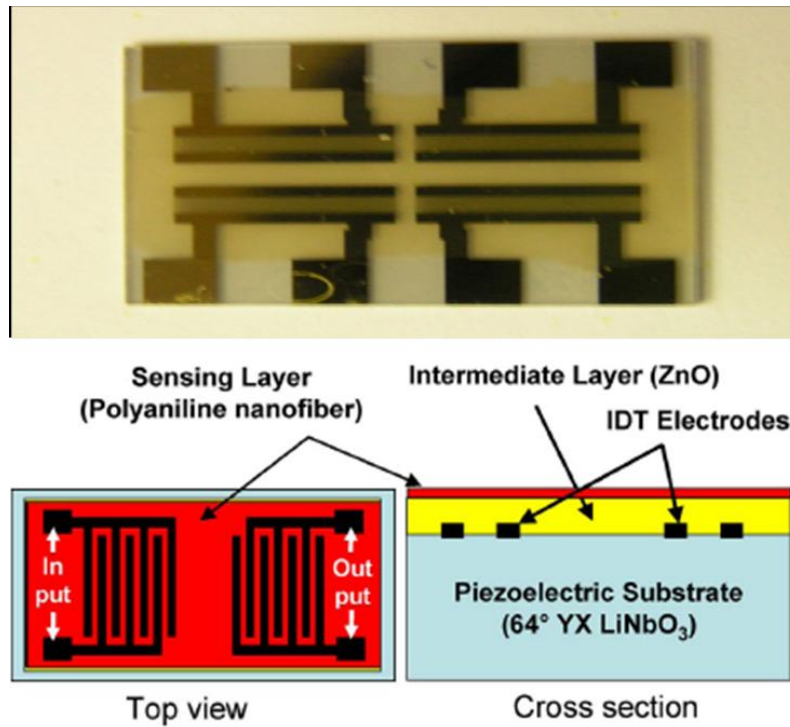


Figure 6: Optical image of two sets of SAW hydrogen sensors and the schematic view of top and cross section of a SAW hydrogen sensor [95, 97].

In the device shown in Fig. 6, a bilayer ( $\text{ZnO}/64^\circ \text{ YX LiNbO}_3$ ) was used as the substrate which had a much stronger acoustoelectric effect. Polyaniline nanofiber was used as the hydrogen sensing layer. Interdigitated electrodes (IDEs) were employed to convert the surface acoustic wave to electrical signal or visa versa by utilizing the piezoelectric effect of the substrate material. The sensing materials used in SAW based hydrogen sensors could be polyaniline [95], Pd [96], polyaniline/ $\text{WO}_3$  nanofiber composite [97], ZnO nanorod [98],  $\text{WO}_3$  thin film [99-100]. Advantages of these planar SAW hydrogen sensors include fast

response and recovery, good repeatability and baseline stability, but the low detection limit is high (>1%).

#### 1.2.4. Optical hydrogen sensors

Most optical hydrogen sensors are based on optical fibers coated with Pd or Pd alloy. As mentioned in section 1.2.1.2, Pd and its alloys have a distinguished ability to dissolve hydrogen atoms, resulting in volume increase and a decrease of the carrier density. The reflectivity ( $R_{ref}$ ) or reflective index of the Pd and Pd alloys depends on the carrier density. The following equations reveal the relationship [101]:

$$R_{ref} = \frac{(n_R - 1)^2 + n_I^2}{(n_R + 1)^2 + n_I^2} \quad (1.9)$$

$$n^* = \frac{c}{\omega} \left( \frac{1}{\delta} - \frac{i}{\delta} \right) \quad (1.10)$$

$$\delta = \sqrt{0.5 \times (\omega \varepsilon_0 \sigma)} \quad (1.11)$$

where  $n_R$  and  $n_I$  are the real and imaginary parts of the refractive index, respectively,  $n^*$ , the complex refractive index of a metal,  $\sigma$ , the conductivity of the material,  $\omega$ , the frequency of light,  $\varepsilon_0$ , the permeability of free space.  $\delta$ , the damping of an incident electromagnetic wave, and  $c$ , the speed of light.

Equation 1.9 indicates reflectivity could be modulated by changing the charge density. The exposure of the Pd or Pd alloy to hydrogen causes a decrease in conductivity ( $\sigma$ ) and hence the real and imaginary parts of the refractive index [102]. Most Pd based optical



hydrogen sensors utilize this mechanism to detect hydrogen by measuring the change of reflectance [103], transmittance [104-108], and optical power [102, 109] induced by Pd/H hybrid.

The Pd-coated FBG (fiber Bragg grating) hydrogen sensors detected hydrogen by using the swelling feature of Pd or Pd alloy in the presence of hydrogen [110]. FBG is a type of optical filter that reflects light with a particular wavelength and transmits all others. The change of the grating structure or period can alter the reflected wavelength. Pd coated onto the FBG expands by absorbing hydrogen atoms and subsequently induces mechanical strain in the grating. Induced strain shifts the reflected Bragg wavelength toward a longer wavelength. This spectral shift could be accurately measured and used to characterize the hydrogen concentration [110].

C. Caucheteur et. al. reported another type of FBG hydrogen sensor coated with a layer of Pt doped WO<sub>3</sub> thin film [111]. The doped WO<sub>3</sub> reacted with hydrogen, generated heat due to the exothermic reaction and elevated the local temperature (could be as high as 200 °C), which induced the wavelength shift. The sensor was fast (response time was in the range of 1 second) and had no response to other gases such as O<sub>2</sub>, CH<sub>4</sub>, N<sub>2</sub> and H<sub>2</sub>O.

Optical hydrogen sensor based on the gasochromic effect were reported [112-113]. WO<sub>3</sub> thin film was transparent in air and changed to blue in hydrogen. The reaction mechanism is given as [112]:



In a hydrogen environment, the oxidation number of W<sup>6+</sup> gradually reduced to W<sup>5+</sup> due to the insertion of H atoms, and accordingly, the color of WO<sub>3</sub> then changed to blue. The

reaction was reversible and the color of the  $\text{WO}_3$  thin film could change back to transparent in air. The device detected the hydrogen by measuring the transmission response or colorations spectra.

The main advantage of most optical hydrogen sensors is environmental ruggedness, especially since they are resistant to electromagnetic interference. The disadvantage is the need of light (laser) sources and complex optical measurement systems.

#### 1.2.5 Other types of hydrogen sensors

Micro cantilever hydrogen sensors detect hydrogen by measuring the bending of the cantilever beam coated with Pd or Pd alloy, which expands into a hydrogen environment and induces bending. Both the optical [114-115] and electrical [116] methods were applied to measure the bending of the beam with relatively high sensitivities. However, the sensors are subject to humidity and temperature.

Capacitor hydrogen sensors are based on metal-insulator-semiconductor (MIS) [117-119]. The dissociated hydrogen atoms penetrate through the catalytic metal (typically Pd), form a dipole layer at the metal/insulator interface and change the work function of the metal, which induces the capacitance change. The advantage of this type sensor is low power consumption due to no current.

Micro thermoelectric hydrogen sensors ( $\mu$ -THS) utilize the exothermic oxidation of hydrogen. Heat from the catalytic reaction on the catalyst (Pt or Pd) surface elevates the temperature on one end of the thermoelectric sensing line (typically SiGe line). The thermoelectric material could transfer the temperature difference to the output voltage to detect the hydrogen concentration.  $\mu$ -THS have showed very high selectivity over  $\text{CH}_4$ , CO,

ethane (C<sub>2</sub>H<sub>6</sub>), methanol (CH<sub>3</sub>OH), ethanol (C<sub>2</sub>H<sub>5</sub>OH), and tetrahydrene (C<sub>4</sub>H<sub>4</sub>), but the detection limit is high. Most of the testing was carried out in hydrogen concentrations higher than 0.5% [120-123]

### 1.3 Electrical properties of SnO<sub>2</sub> and In-doped SnO<sub>2</sub>

As shown in section 1.2.1.1, SnO<sub>2</sub> chemiresistor hydrogen sensors are based on the measurement of resistance change. Understanding the electrical properties and conduction models is the key to employing the detection mechanism, designing sensors and improving sensor performance.

#### 1.3.1 Conduction models of SnO<sub>2</sub>

SnO<sub>2</sub> is a wide band gap semiconductor with a band gap of 3.5-3.7 eV [124-126] at 300 K. The advantages of wide band gap materials are strong breakdown strength and large saturation current. Conventionally, SnO<sub>2</sub> is considered an n-type semiconductor due to its intrinsic point defects (Sn interstitial and oxygen vacancy [124]), though it is not very clearly demonstrated [125]. The missing of oxygen atoms in the SnO<sub>2</sub> matrix makes SnO<sub>2-x</sub> more conductive and is the main contributor to the high level of electron density (up to 10<sup>20</sup> cm<sup>-3</sup> [124-125]). The value of x is between 10<sup>-3</sup> and 10<sup>-5</sup> [126]. The oxygen vacancy could be treated as n-type doping with the “doping” concentration of 2[V<sub>o</sub><sup>2+</sup>] [126]. The possible mechanism of the formation of oxygen vacancies is expressed as [126]:

$$O_o = O_{surf} + V_o \quad (1.13)$$

$$V_o = V_o^{2+} + 2e \quad (1.14)$$

In atmosphere, the adsorbed oxygen molecules oxidize the SnO<sub>2</sub> surface by trapping free electrons from the bulk SnO<sub>2</sub> and thus form a negative charged surface and positive charged donor layer underneath. In the n-type SnO<sub>2</sub>, there are not enough positive free charges (holes) at the surface to compensate all the negative charges. Therefore, the uncompensated negative charges build the negative potential, preventing free electrons from diffusing from the bulk to the positive charged donor layer. This forms a stable free electron depletion layer (space charge layer) at the surface (similar as a p-n junction). In the space charge layer, an electric field is developed with a built-in voltage of  $V_s$ , corresponding to the energy band bending at the surface. Only the free electrons with energy higher than  $qV_s$  ( $q$  is electron charge) can penetrate the space charge layer. The thickness of the space charge layer can be characterized by the Debye length ( $L_D$ ) [127]:

$$L_D = \sqrt{\frac{\epsilon_r \epsilon_0 kT}{q^2 N}} \quad (1.15)$$

where  $\epsilon_r$  and  $\epsilon_0$  are relative dielectric constant and dielectric constant of vacuum, respectively.  $N$  is the concentration of free charge carriers.

A more accurate value of the space charge layer thickness ( $z_0$ ) is given as [127]:

$$z_0 = \left( \frac{qV_s}{kT} - 1 \right)^{1/2} \cdot L_D \quad (1.16)$$

Equation 1.16 depicts how the build-in voltage or Schottky barrier effect the thickness of the space charge layer. The larger  $V_s$ , the thicker the  $z_0$ .

Conduction models were proposed based on the variation of the geometries of  $\text{SnO}_2$  thin film [128] and still have been studied nowadays [129-133] as shown in Fig. 7 [130].

Case (a) The first model shown in Fig. 7 is the surface/bulk model for compact  $\text{SnO}_2$  film. Due to the adsorption of the oxygen molecules, the energy bands bend at the surface and the total resistance is described as two parallel resistances, the surface (space charge layer) resistance and bulk resistance. In the space charge layer, free electron concentration is very low resulting in huge resistivity. Because of this, the total resistance is controlled by bulk resistance (bulk control). The presence of hydrogen has the ability to change the resistance of the surface layer, but does not affect the bulk resistance. As a result, the compact film is not suitable for high sensitivity hydrogen sensor. The negative charged surface and positive charged donor layer also form a capacitor as shown in the Fig. 7. Most  $\text{SnO}_2$  chemiresistor based gas sensors measure the resistance by DC; the effects of capacitors are ignored.

Case (b) When the film consists of the grains with the grain size  $D \gg L_D$ , the resistance is controlled by the high potential barriers at the interface of the grains (grain boundary control).

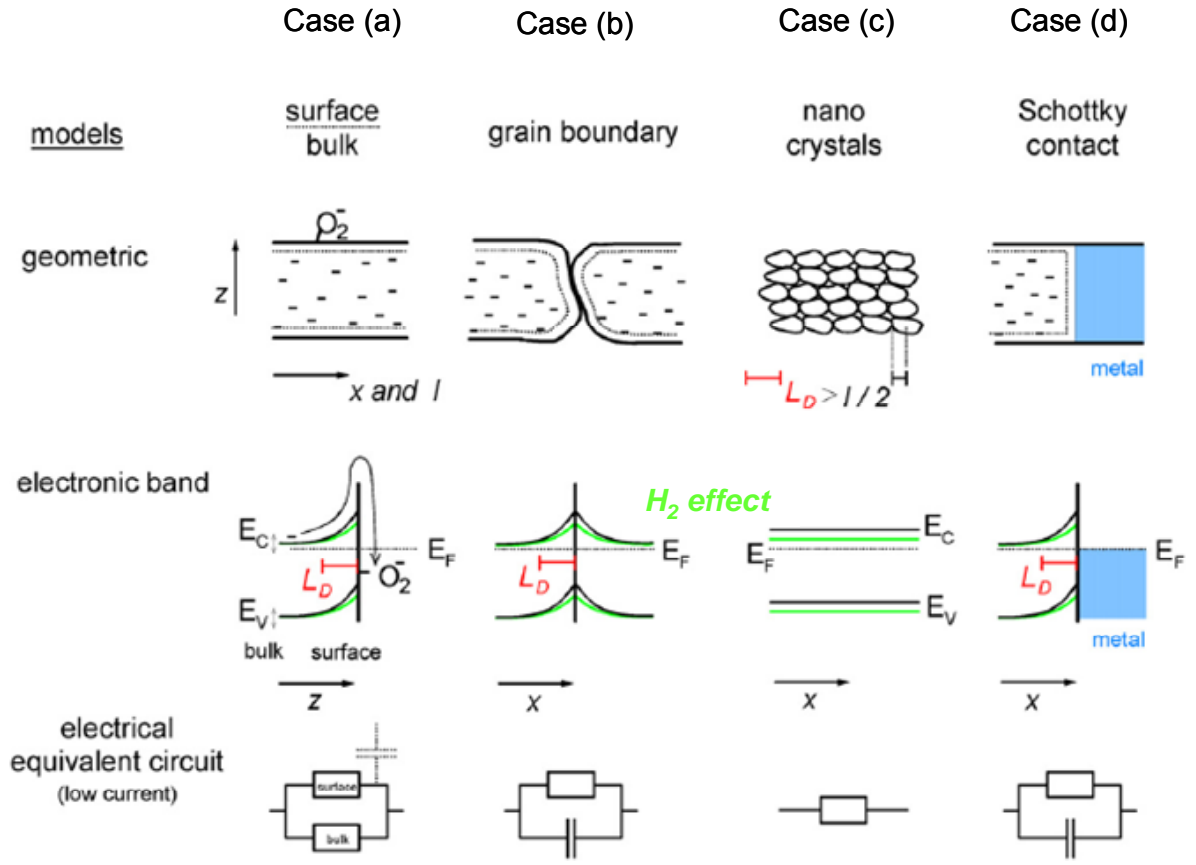


Figure 7: Conduction models based on grain sizes and contacts with metals in SnO<sub>2</sub> thin film and the equivalent circuitries.  $E_C$  is the minimum of the conduction band;  $E_V$  the maximum of the valence band;  $E_F$  the Fermi level;  $L_D$  the Debye length [130].

Case (c) If the grain size is small enough,  $D < 2L_D$ , the whole grain is in the space charge region (grain control). Because  $D$  is small, the potential drop ( $\Delta V_s$ ) from the grain surface to the grain center is low ( $q\Delta V_s < kT$  [131]), forming a flat energy band. Figure 8 shows this difference of the band diagram between large grains (Case (b)) and small grains (Case (c) SnO<sub>2</sub> [131-132].

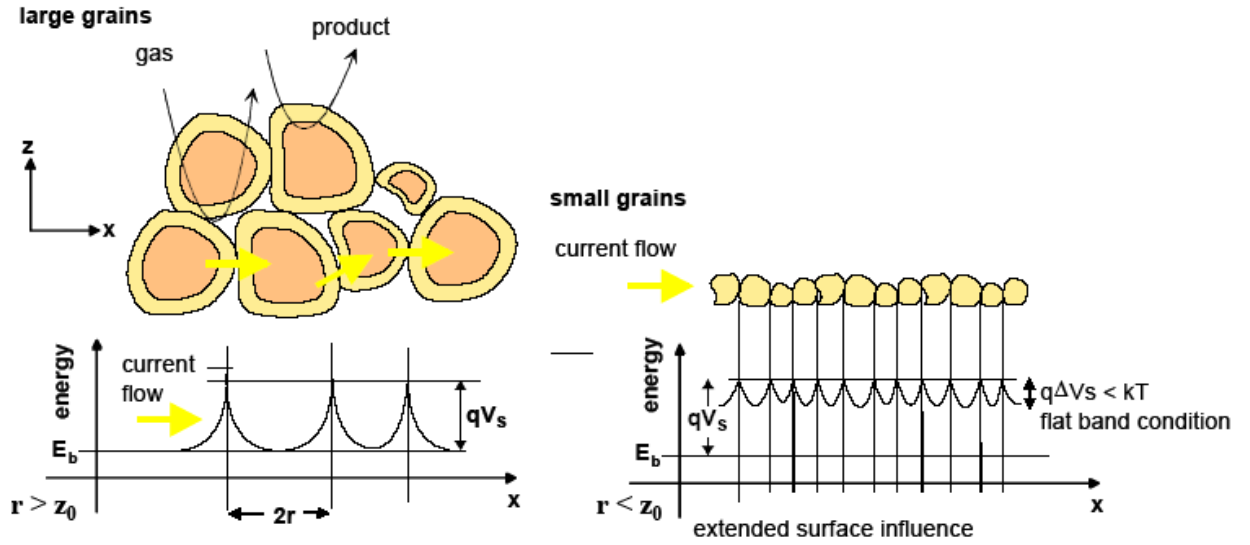


Figure 8: Effect of the grain size on the conduction mechanism [131].

In Fig 8, for large grain  $\text{SnO}_2$ , the resistivity at the grain-grain interface (space charge layer) is much larger than the bulk resistivity considering bulk  $\text{SnO}_2$  is an n-type semiconductor with a high electron concentration. Thus, the total resistance is controlled by potential barriers (or resistances) at grain-grain interfaces. For fully depleted small grain  $\text{SnO}_2$ , electrons are adsorbed to the surface and the bulk electron density is lowered, resulting in high bulk resistivity. Because of the flat band condition (small  $q\Delta V_s$ ), not much difference exists between bulk and interface conductivity, and the total resistance is controlled by the bulk resistivity (or surface resistivity).

Case (d) At the interfaces of  $\text{SnO}_2$  and the metal, in most cases, Schottky contact exists due to the discrepancy in work functions. Free electrodes move from  $\text{SnO}_2$  to the metal leaving a positive charged donor layer inside the  $\text{SnO}_2$  which corresponds to the energy band bending at the interface. As described in section 1.2.2.1, the Schottky barrier height depends on the work function of the metal for the given  $\text{SnO}_2$  thin film (Schottky control). It should be noted that the potential barriers at the grain-grain interface are affected by the contamination

from the atmosphere (such as  $H_2O$ ), but the Schottky barrier height at metal-grain surface is not [131].

Further discussion about the grain boundary control model (Case (b)) was presented by N. Barsan et. al. [129]. For the porous film with the grain size equal or larger than the Debye length ( $D \geq L_D$ ), conduction of the  $SnO_2$  is determined by the connection (neck) between the grains, as shown in Fig. 9 [131]. These necks act like the current path between  $SnO_2$  grains. The current flow is controlled by the neck width ( $z_n$ ), depletion depth ( $z_0$ ) and neck length. Surface reaction does not change the bulk free electron density, but does change the current channel width ( $z_n - 2z_0$ ) by change the thickness of the depletion layer ( $z_0$ ). When neck size is large enough ( $z_n \gg 2z_0$ ), the bulk/surface model (Case (a)) applies. When  $z_n \leq 2z_0$  (Fig. 9 (b)), the resistance is mainly controlled by the Schottky barriers at the grain/grain interfaces. In this case, the total resistance depends on the number of the grains in the x direction, and the potential barriers at the grain/grain interface.

A more complex situation happens when  $z_n > 2z_0$  and  $z_n$  is comparable to the mean free path of the free electrons (Fig. 9 (a)) because the chance of a collision with the grain surface increases and surface adsorbed species may act as additional scattering centers [129]. The relationship between the electron mobility and mean free path could be expressed as [133]:



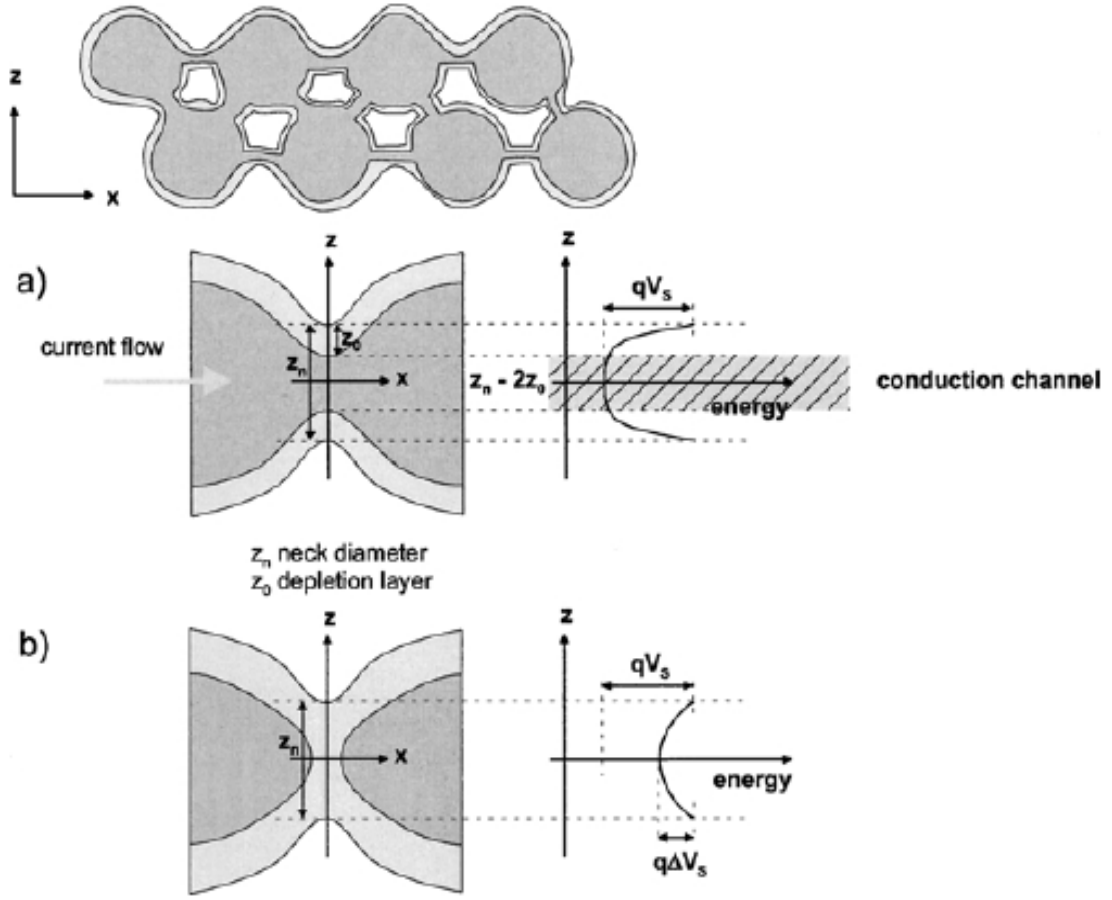


Figure 9: Neck control model for the porous large grain  $\text{SnO}_2$  thin film: (a)  $z_n > 2z_0$  and (b)  $z_n < 2z_0$  [131].

$$\mu_{neck} = \frac{\mu_{bulk}}{1 + \theta(l_{MFP} / z)} \quad (1.17)$$

$$\theta = 1 - \frac{n_s}{n_{bulk}} \quad (1.18)$$

$$l_{MFP} = \frac{\sqrt{(8/\pi)kTm^*}}{q} \mu_{bulk} \quad (1.19)$$

where  $\mu_{\text{neck}}$  is the mobility in the neck area,  $\mu_{\text{bulk}}$  the bulk mobility,  $l_{\text{MFP}}$  the mean free path,  $\theta$  the surface coverage degree (number of O-ion occupied sites divided by number of possible sites on the surface) and  $n_{\text{bulk}}$  the bulk electron concentration.

Equation 1.17 shows both surface property ( $\theta$ ) and size of the neck ( $z_n$ ) could modulate the mobility at the neck area and therefore change the resistivity of the neck. The smaller the  $z$ , the smaller the mobility and hence the larger resistivity.

In summary, oxygen adsorption on the  $\text{SnO}_2$  surface induces the surface charge layer and a built-in voltage which is responsible for the energy band bending at the surface. For the compact sensing film, resistance depends on the bulk resistance. For the granular  $\text{SnO}_2$ , Schottky barriers at the grain-grain interface dominate the whole conductivity if the  $D$  is not too small ( $D > 2L_D$ ). With  $D \leq 2L_D$ , grains are fully depleted showing huge resistivity. Schottky barriers exist at the  $\text{SnO}_2$ /metal interfaces which could modulate the total resistance.

### 1.3.2 Fundamentals of the In-doped $\text{SnO}_2$

One of the issues of  $\text{SnO}_2$  chemiresistor based hydrogen sensors is the low sensitivity at room temperature. Integrating micro heaters will not only make sensors consume more energy, but also bring extra concerns about safety. One way to improve the sensitivity at room temperature is to introduce dopants. As shown in section 1.2.1.1, various dopants have been studied by different methods. Among them, In-doped  $\text{SnO}_2$  nanocrystalline showed giant sensitivity up to  $10^5$  with the assistance of MEMS sensor platforms at room temperature [6,131-135].

### 1.3.2.1 Type of In-doped SnO<sub>2</sub>

In the view of semiconductors, when impurities (such as In) with its number of valence electron, one less than Sn, substitute Sn in the matrix of SnO<sub>2</sub>, acting as acceptors, the hole density increases and free electron density decreases. Considering SnO<sub>2</sub> itself is an n-type semiconductor with large free electron density, a small amount of In doping concentration will not change the main carrier type but probably reduce the free charge concentration. When the In-doping concentration exceeds a certain value, SnO<sub>2</sub> may transform to a p-type semiconductor. Both experiments [136-137] and simulation work [125] have proven that In-doped SnO<sub>2</sub> can be p-type. If the doping concentration continuously increases, In-doped SnO<sub>2</sub> could convert to n-type again like tin-doped indium oxide (ITO), a well-known transparent n-type semiconductor, because the In<sub>2</sub>O<sub>3</sub> of cubic structure exists [137]. Figure 10 (a) shows the change of type with In-doping concentration (material processing temperature is 700 °C). When the doping concentration is between certain values (In/Sn ratio is between 0.05 and 0.25 in Fig. 10 (a)), In-doped SnO<sub>2</sub> did show p-type characteristics. Processing temperature is another tuning parameter as seen in Fig. 10 (b). For In/Sn = 0.2, the type changed at a temperature of 575 °C from n-type to p-type. The reason might due to that at low temperature of the acceptor function has not been activated [137].

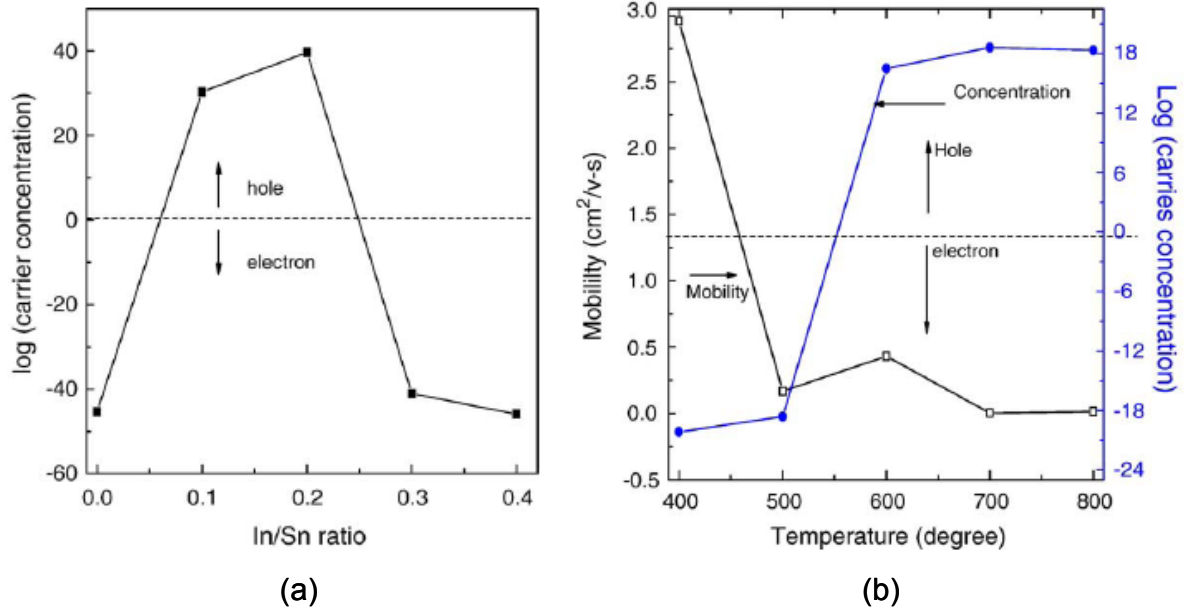


Figure 10: (a) Carrier type vs. In/Sn ratio, (b) Carrier type vs. processing temperature [137].

### 1.3.2.2 Effects of In-doping on room temperature hydrogen sensing

Room temperature hydrogen sensing capability of In-doped SnO<sub>2</sub> is attributed to In<sup>3+</sup> doping [134-135, 138-140]. This trivalent doping is believed to increase the concentration of oxygen vacancy in SnO<sub>2</sub> providing more oxygen adsorption sites [138]. The reaction of the doping is expressed as [141-142]:



The benefits of the increase in oxygen adsorption are:

(1) At room temperature, the number of active surface sites (oxygen ions) is considered to be low [138]. It is a reasonable assumption because at low temperature, both moisture and oxygen adsorptions dominate and they are competitive. Increase of the surface adsorption of oxygen ions drives the Reaction 1.3 (see section 1.2.1.1) to the forward direction which increases the sensitivity.

(2) Higher oxygen-ion adsorption concentration makes the surface more negatively charged. As discussed in section 1.3.1, this could increase the built-in voltage and extend the space charge layer further into the bulk. The contact resistance is simplified and given as [143]:

$$R_c = \frac{A}{q\mu_{bulk}N_d} \exp\left(\frac{qV_s}{kT}\right) \quad (1.22)$$

where  $R_c$  is contact resistance at the grain-grain interface,  $A$  the constant determined by the semiconductor geometry,  $N_d$  the density of the donors.

In the grain boundary control model, the larger built-in voltage ( $V_s$ ) results in higher contact resistance. Higher sensitivity could be achieved by reducing this higher contact resistance to the bulk resistance with the presentation of hydrogen.

3) In-doping lowers the band gap energy of  $\text{SnO}_2$ . The band gap energy of pure  $\text{SnO}_2$  is 3.5-3.7 eV [124-126]. The measured values of In-doped  $\text{SnO}_2$  were 2.55 eV ~ 3.44 eV [142]. This lowering enhances the “ability for nanocrystalline In- $\text{SnO}_2$  to be used in gas sensor applications at room temperature, since the potential barrier required for charge to move between grains is now reduced with lower band gap energy” [142].

In this work, the proposed nanoparticle/MEMS hydrogen sensor is based on In-doped SnO<sub>2</sub> nanocrystalline with Pt as the catalyst. With the optimized design, the MEMS sensor platform enhanced the sensitivity from less than 1 [138] to 10<sup>5</sup> [6, 135] and reduced the response time from several tens of minutes [138] to less than 10 seconds.

## CHAPTER 2 MODEL ANALYSIS OF MEMS HYDROGEN SENSORS

### 2.1 From macro to MEMS sensors

The novel hydrogen sensing material, polycrystalline In-doped  $\text{SnO}_2$  nanoparticles, has been developed by Dr. Seal's group at UCF [138,]. Bulk hydrogen sensors as shown in Fig 11 [140] exhibited good hydrogen sensing ability at room temperature [138].

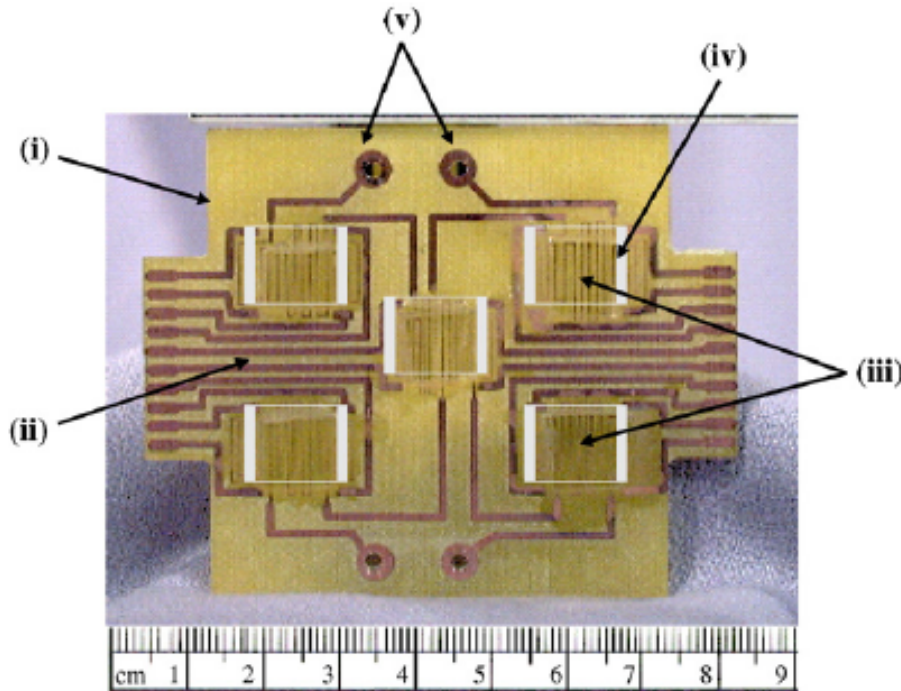


Figure 11: Bulk hydrogen sensors. (i) fiber-glass board, (ii) Cu connectors, (iii) sensor areas: In-doped  $\text{SnO}_2$  thin films on Pyrex glass substrates (iv) Ag-electrodes with the gap of 1 cm, and (v) Cu-connectors for the heater-circuit (for high temperature testing, not used) [140].

Figure 11 shows the macro sensor platform. In-doped  $\text{SnO}_2$  nanoparticles were dip-coated on thin Pyrex glass substrates, and then were mounted on the fiber-glass board with Cu lines by epoxy. Silver (Ag) paste was used to connect the sensors to the Cu lines

while keeping an approximately 1 cm gap between Ag electrodes manually. Figure 12 shows the testing results of the macro sensors at room temperature [138]. The sensors could sense hydrogen at room temperature, but the sensitivity was no more than 0.5, even at a high concentration of 2% hydrogen. The response time of the sensor tested in 4% hydrogen was 2,000 seconds [138]. The hydrogen sensing characteristics of the material had not been fully exploited due to the limitation imposed by the macro sensor platform.

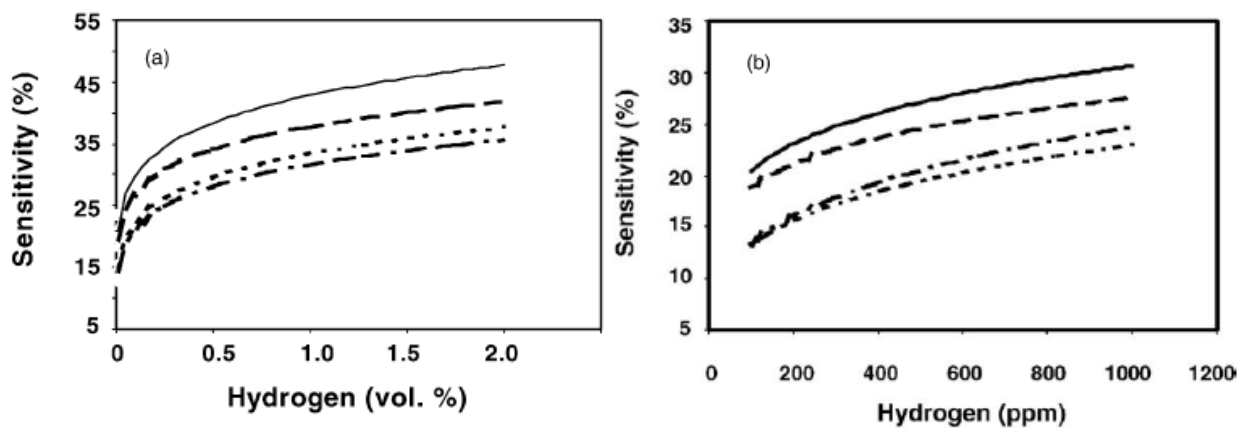


Figure 12: Sensitivity of In-doped SnO<sub>2</sub> macro sensors (a) in high concentration, and (b) in ppm level [138].

The first generation MEMS sensors integrating In-doped SnO<sub>2</sub> nanoparticles and micromachined IDEs were fabricated and tested as shown in Fig 13 by the collaborative research between Dr. Seal and Dr. Cho [134].



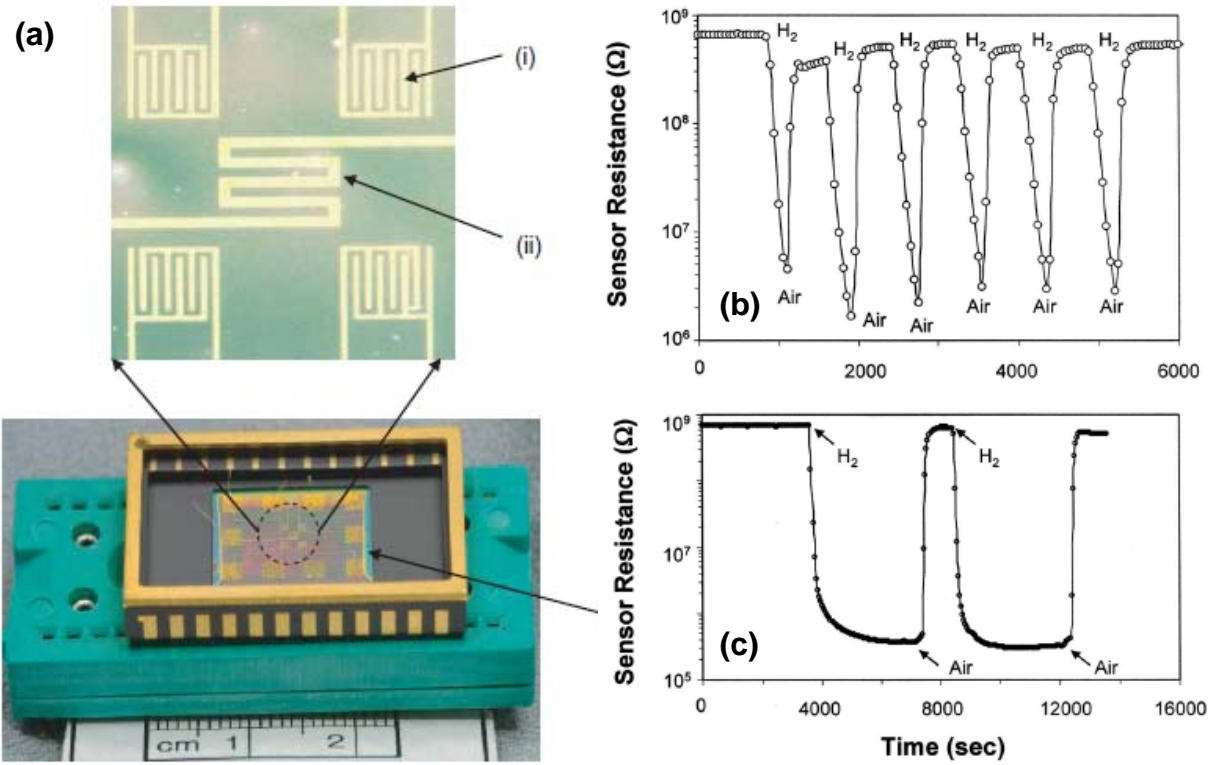


Figure 13: First generation MEMS sensors: (a) packaged sensor platform - (i) interdigitated electrodes (ii) resistive temperature sensor to monitor the temperature, (b) multicycle test results, and (c) the individual cycle with a sensing signal reaching a saturated value [134].

Figure 13 (a) shows the packaged MEMS hydrogen sensors and micromachined IDEs with 4 fingers separated by a  $50\text{ }\mu\text{m}$  gap in each electrode. The finger is  $50\text{ }\mu\text{m}$  wide and  $1000\text{ }\mu\text{m}$  long. Figure 13 (b) shows the multicycle test with the testing time of 350 seconds. Sensors showed good repeatability. Figure 13 (c) shows the individual cycles with a full span of sensor signals from maximum to minimum values. The maximum sensitivity was 2,200 and response time was less than 100 seconds. Compared to the macro sensors with sensitivity of less than 0.5 and response time of larger than 2000 seconds, MEMS sensors did show much improved sensor performance.

## 2.2 Working principle of In-doped SnO<sub>2</sub> hydrogen sensors

For the sensor design and analysis, understanding of sensor working principles in detail helps optimize the design for better sensitivity and response time. Figure 14 shows the schematic view of a sensor with a sensing film and the interdigitated Au electrodes lying on the Si/SiO<sub>2</sub> substrate. Discontinuous Pt nanoclusters are on top of the sensing film, which is sputter-deposited as the catalyst. Adsorbed oxygen binds the electrons in the conduction band of SnO<sub>2</sub> surface and transfers to O<sup>-</sup> or O<sup>2-</sup>. O<sup>2-</sup> is not stable and transfers to O<sup>-</sup> unless it can occupy the oxygen vacancy immediately [143]. When introduced onto the Pt-catalyst surface which lowers the reaction energy, hydrogen molecules become dissociated by the catalytic reaction. The hydrogen atoms are then decomposed to hydrogen ions (protons) and free electrons. The generated protons react with adsorbed oxygen ions forming OH groups. Two adjacent OH groups combine with each other releasing water and an oxygen ion. During the whole process, one net electron is generated and contributes to the free electron density in SnO<sub>2</sub>. The reactions are given in [4, 138]:

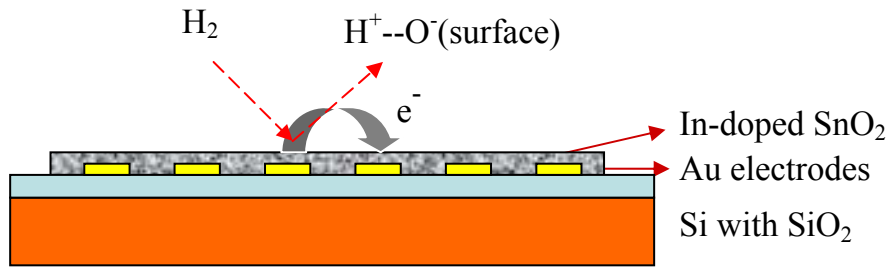


Figure 14: Working principle of the In<sub>2</sub>O<sub>3</sub> doped SnO<sub>2</sub> hydrogen sensors.





The net reaction is:



Reaction 2.1 happens before the hydrogen gas is introduced as the initial condition for the following reactions. Reaction 2.3 shows the electrons are from the dissociation of nascent hydrogen atoms, and this determines the increase rate of electron concentration on the surface for given  $[O_{ads}^{-}]$ . Doped  $In^{3+}$  cations helps to increase the concentration of surface-adsorbed oxygen ions which favor the forward reaction presented in Reaction. 2.7 and increase the sensitivity of the sensing material (See section 1.3.2.2). The IDEs are used as the transducer to collect the electrons (electrical signal).

Two main parameters are used to characterize the sensor performance, sensitivity (S) and response time. The sensitivity (S) is defined as:

$$S = \frac{R_a}{R_g} \quad (2.8)$$

where  $R_a$  and  $R_g$  are the measured resistance of the sensor in air and in  $H_2$  gas, respectively. In a MEMS sensor shown in Fig. 13 (a) or Fig. 14, both  $R_a$  and  $R_g$  consist of resistance of the material and the resistances at material/electrode interfaces.

Generally, in chemiresistor based hydrogen sensors, the response time ( $t_{90}$ ) is defined as the time duration to reach 90% signal change (resistance change or sensitivity change) [46, 49, and 51]. According to the definition, the response time is associated with the sensitivity. For the sensors with the same resistance change (drop) rate, sensors with higher sensitivity always show longer response time as shown in Fig. 2.5.

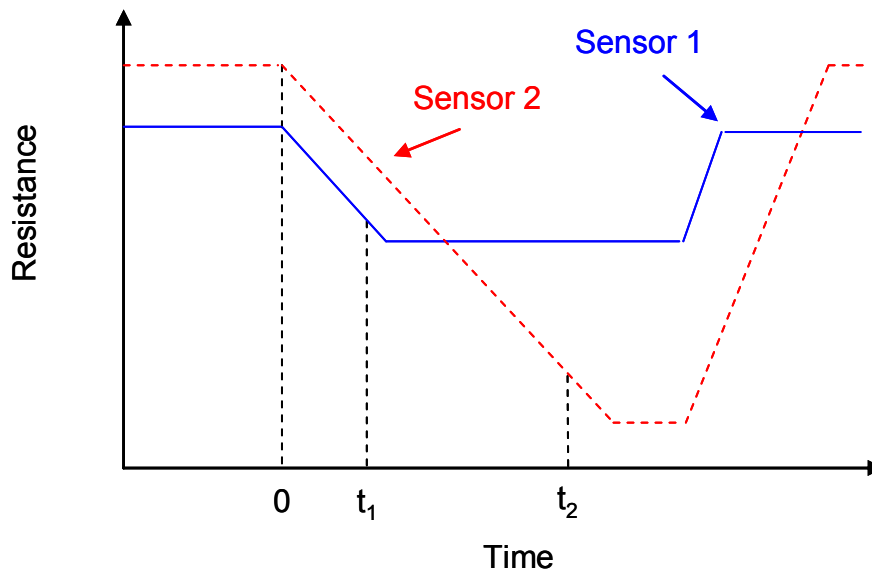


Figure 15: Relationship of the response time ( $t_{90}$ ) and the sensitivity.

Figure 15 shows the typical response of two chemiresistor based hydrogen sensors. Assume that Sensor 1 and Sensor 2 have the same resistance drop rate; Sensor 1 shows smaller response time just because of its lower sensitivity. But obviously, the response of Sensor 2 is not slower than Sensor 1. In this case, resistance change rate is more suitable to

represent the sensor's response time. For the sensors with high sensitivity (larger than 10), the time ( $t_r$ ) to reach one order magnitude change (drop) in sensitivity or resistance could be used as the response time with a slightly larger value than  $t_{90}$ . Because almost all the proposed sensors in this work have the sensitivity larger than 10,  $t_r$  was used as the response time throughout.

### 2.3 Theoretical analysis of the MEMS hydrogen sensor

Conventionally, chemiresistor type sensor uses a pair of electrodes. Sensor signal comes from the current between the electrodes. The transfer of the conduction electrons is affected by the free charge losses due to the defects, various scattering centers and potential barriers at the grain-grain interfaces [146]. A large gap between two electrodes means a large sensitive area or more active adsorption sites, which enhances the sensitivity, though the current path becomes long and free charge losses are greater [146]. If using IDEs with small gap, large sensing areas may be maintained by using long fingers and a large number of fingers. The small finger gap might reduce the free charge losses by shortening the current path, and thus enhance the sensing signal (sensitivity). Advantages of fabricating micro IDEs using MEMS technique include precise control of the geometry and dimension in batch production, which leads to good reproducibility and low cost.

### 2.3.1 Theoretical model of IDEs

The main design parameters of interdigitated electrodes are the gap ( $g$ ), finger width ( $w$ ) finger length ( $l$ ), and number of fingers ( $N$ ) as shown in Fig, 16.

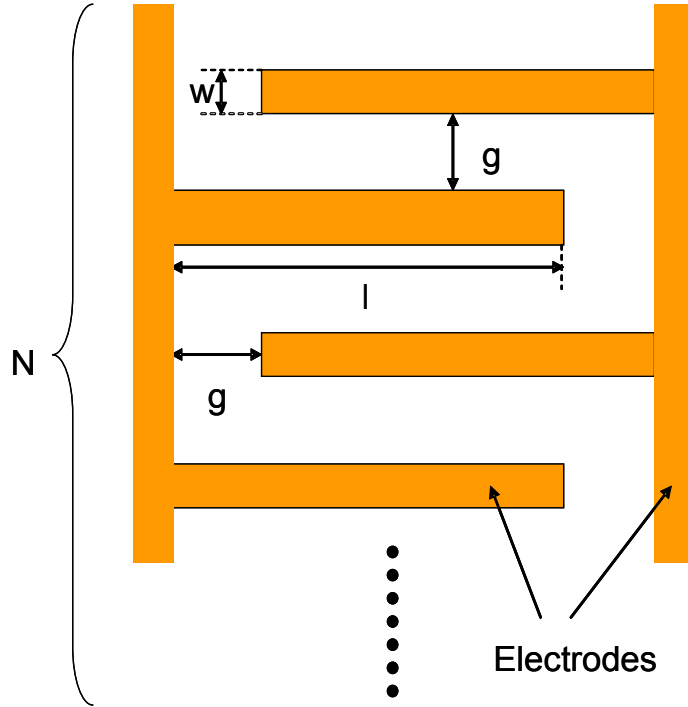


Figure 16: Schematic view of IDEs (top view).  $g$  is the gap.  $w$ , the width,  $l$ , the length of the fingers and  $N$ , the number of electrodes.

When electrical power is applied, the potential distribution  $V(r)$  is given as [150]:

$$V(\vec{r}) = \int_{-\infty}^{\infty} \int_{-\infty}^{\infty} \int_{-\infty}^{\infty} \frac{\sigma(\vec{r}')}{4\pi\epsilon|\vec{r} - \vec{r}'|} d^3\vec{r}' \quad (2.10)$$

where  $\sigma(r)$  is the distribution of the surface charges and  $\epsilon$  is the dielectrical constant.

For long finger IDEs which have a periodic structure (edge effects at the finger tips are ignored), the potential distribution in the  $z$  direction (the direction along the finger length) is the same:

$$V(x, y, z) = V(x, y, 0) \quad (2.11)$$

Therefore, by getting  $V(x, y, 0)$  on the  $x$ - $y$  plane, the whole distribution  $V(x, y, z)$  could be obtained by repeating  $V(x, y, 0)$  in  $z$  direction directly. The following discussion is focused on  $V(x, y)$  in  $x$ - $y$  plane.

Basically, there are three ways to place the electrodes as showed in Fig. 17.

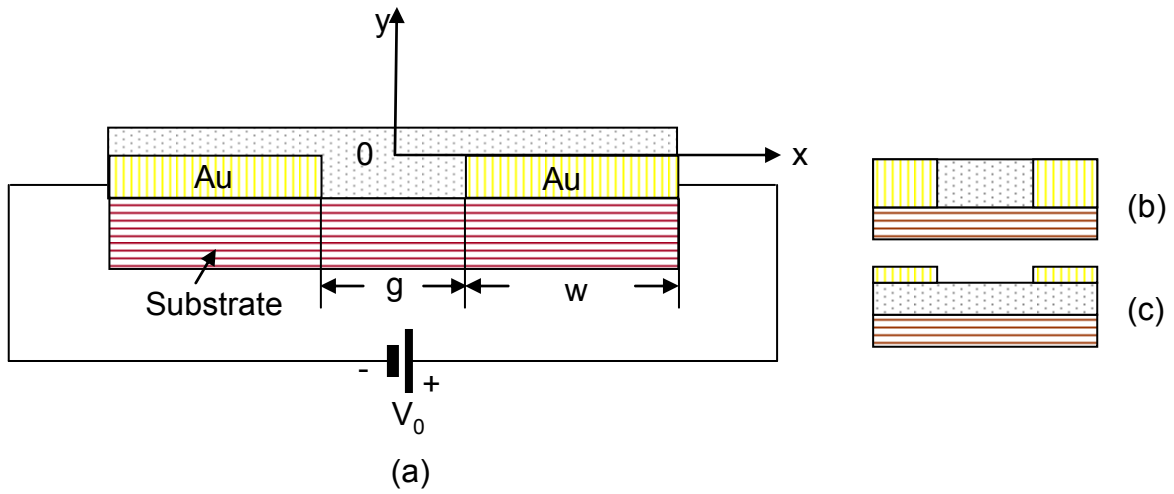


Figure 17: A cross-section view of  $x$ - $y$  plane with a pair of IDEs placed (a) at the bottom with applied voltage of  $V_0$ , (b) at the side, and (c) at the top of the sensing layer.

Figure 17 shows three possible configurations for placing the electrodes with respect to the sensing layer: at the bottom (Fig. 16 (a)), at the side (Fig. 16(b)) or at the top (Fig. 16 (c)) of the sensing layer. The configuration in Fig. 16 (b) has the simplest potential and electric

field distribution. In the area between the electrodes, the distribution of potential  $V_b(x,y)$  and electric field  $E_b(x,y)$  are:

$$V_b(x, y) = \frac{V_0}{g} x \quad (2.12)$$

$$E_b(x, y) = \frac{\partial V(x, y)}{\partial x} = \frac{V_0}{g} \quad (2.13)$$

For configurations shown in Fig 16 (a) and (c), mathematically, the distribution of  $V(x,y)$  and  $E(x,y)$  in the sensing film are similar. Analysis is focused on the IDEs at the bottom (Fig. 16 (a)), which is the most possible case. By using Fourier series and applying the boundary conditions, Equation 2.10 is expressed as [150]:

$$V_a(x, y) = \frac{4V_0}{\pi} \sum_{n=1}^{\infty} \frac{1}{2n-1} J_0\left(\frac{(2n-1)\pi g}{2(w+g)}\right) \sin\left(\frac{(2n-1)\pi x}{2(w+g)}\right) \exp\left(-\frac{(2n-1)\pi |y|}{2(w+g)}\right) \quad (2.14)$$

where  $V_0$  is the applied voltage,  $J_0$  the zeroth Bessel function of the first kind.

The electric field  $E_a(x,y)$  and surface charge distribution ( $\sigma(x)$ ) are calculated as [150]:

$$\vec{E}_a(x, y) = -\vec{\nabla} V_a(x, y) \quad (2.15)$$

$$\sigma(x) = -2\varepsilon \lim_{y \rightarrow 0} \left( \frac{\partial^2 V(x, y)}{\partial^2 y} \right) \quad (2.16)$$



The calculation was carried out with the following parameters:  $V_0$  is 2 volts,  $g$  and  $w$  are 10 micron and 50 micron, respectively. Fig. 18 and Fig. 19 show the calculated results of the potential and electric field distribution along  $x$ -direction at a different height (in  $y$  direction). These results exhibit two interesting things. One is that at the edges of the electrodes, the maximum potentials are -1.2 Volts and 1.2 volts ( $y = 0$  curve). The total potential drop is 2.4 volts, which is even larger than the applied voltage (2 volts). A similar phenomenon is observed on the electric field distribution. At the electrode edges, the electric field is much higher. The reason for this is that the surface charge distribution on the electrode surface is not uniform and that most charges accumulate at the edges (See Fig. 120).

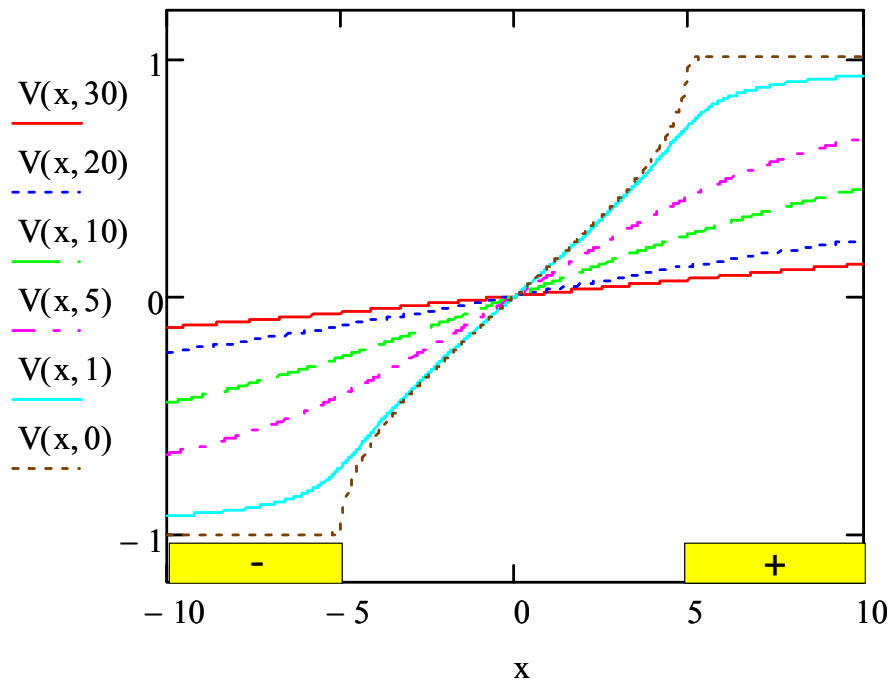


Figure 18: Potential ( $V_a(x, y)$ ) distribution on IDEs with 10  $\mu\text{m}$  in gap, 50  $\mu\text{m}$  in width and applied voltage ( $V_0$ ) of 2 volts at various heights (distance from the electrode surface in  $y$  direction).

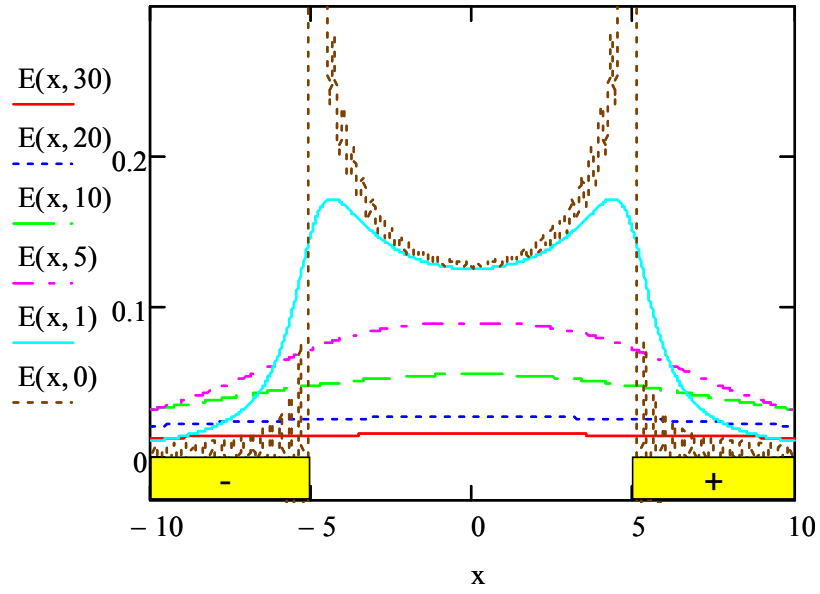


Figure 19: Electric field ( $E_a(x,y)$ ) distribution on IDEs with 10  $\mu\text{m}$  in gap , 50 $\mu\text{m}$  in width and applied voltage ( $V_0$ ) of 2 volts at various heights.

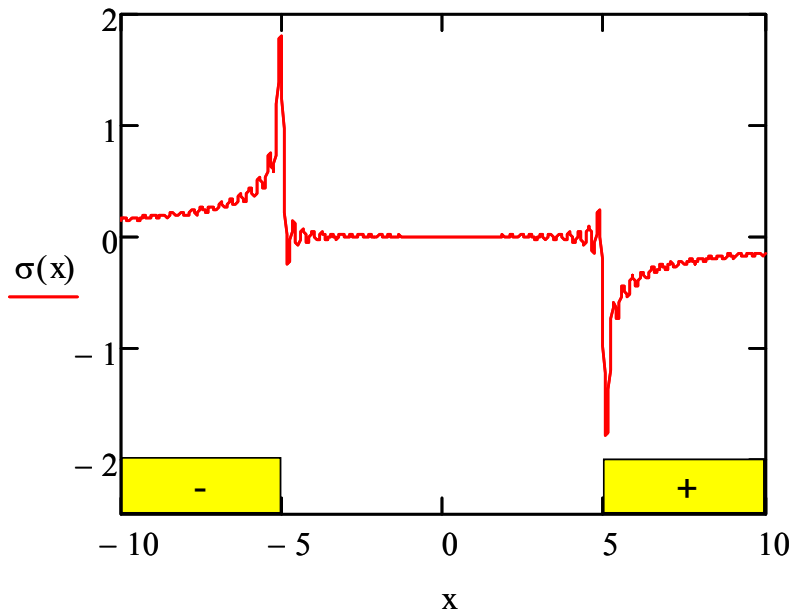


Figure 20: Distribution of surface charge density  $\sigma(x)$  on IDEs with 10  $\mu\text{m}$  in gap and 50 $\mu\text{m}$  in width and applied voltage ( $V_0$ ) of 2 volts.

Figure 20 shows, at the edges, that the surface charge density is much higher than that in the middle of the electrodes and drops rapidly from the edge to the center. This explains why electric field at the edge (near the surface) is much larger.

Another interesting observation is that the distribution of  $E_a(x,y)$  in the y direction is not uniform. With an increase in y (vertical distance from the electrode surface),  $E_a(x,y)$  drops rapidly. At the distance of 30  $\mu\text{m}$  and above, intensity of the electric field  $E_a(x,y)$  is much smaller than that on the electrode surface.

For n-type metal oxide semiconductors (such as In-doped  $\text{SnO}_2$ ), the local current density ( $J$ ) and the current ( $i$ ) are expressed as:

$$J = \sigma_0 \cdot E \quad (2.17)$$

$$i = \int J ds = \int \sigma_0 E ds \quad (2.18)$$

where  $\sigma_0$  is the local conductivity and  $E$  is the electric field.

If the cross-section is chosen at  $x = 0$  in Fig. 17 (a), where  $V_a(0,y) = 0$ , the direction of vector  $E_a(x,y)$  is along x-direction and Equation 2.15 becomes:

$$\vec{E}_a(x,y)\Big|_{x=0} = -\frac{\partial V(x,y)}{\partial x}\Big|_{x=0} \cdot \vec{i} - \frac{\partial V(x,y)}{\partial y}\Big|_{x=0} \cdot \vec{j} = -\frac{\partial V(x,y)}{\partial x}\Big|_{x=0} \cdot \vec{i} \quad (2.19)$$

Current ( $i(t)$ ) flowing in the layer with the height of  $t$  is:

$$i(t) = V_0 \frac{l}{\pi} \int_{y=0}^{y=t} \sigma_0(x, y) E_a(x, y) \Big|_{x=0} dy \quad (2.20)$$

If  $I$  is the total current flowing through the sensing film, current fraction,  $i(t)/I$ , predicts effective sensing film thickness. Figure 21 shows the calculated current fraction ( $i(t)/I$ ) versus thickness of the sensing film. For the given sensing film with a thickness of 100 micron, 84.8% of the current flows in the 30  $\mu\text{m}$  thick layer and 96.9% in 50  $\mu\text{m}$  as shown in Fig.22. If the sensor shown in Fig. 22 is exposed to hydrogen, the local conduction,  $\sigma_0(x, y)$ , of the top surface of the sensing film changes. Due to the small electric field,  $E_a(x, y)$ , on the top surface, the current change is small, which means the resistance change is small for the given applied voltage at this particular time interval. Thus, to achieve fast response, a thin sensing film is preferred because even a small variation in the conductivity ( $\sigma_0(x, y)$ ) could be amplified by a large factor of  $E_a(x, y)$  near the electrode surface, contributing to the sensing signals (See Equation 2.18).

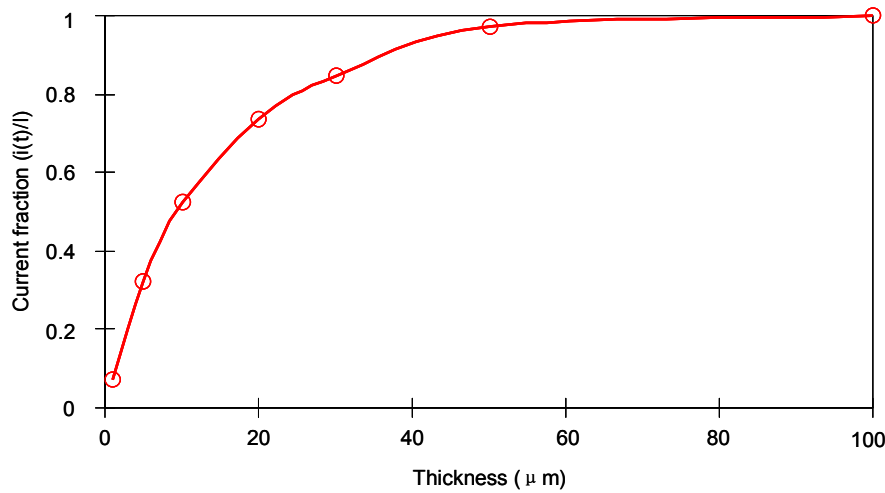


Figure 21: Current fraction in the sensing layer as a function of a thickness of  $t$ .

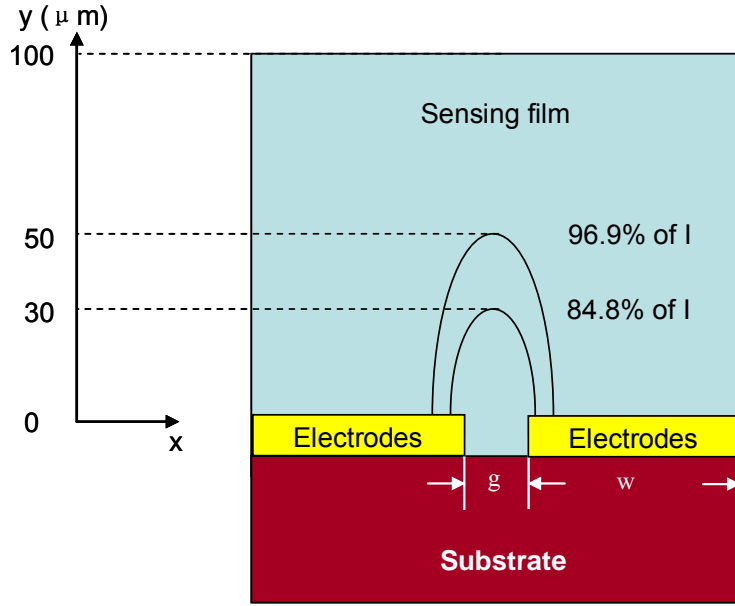


Figure 22: Schematic view of the current distribution in the sensing film.

Based on this analysis, the structure shown in Fig. 16(c) (IDEs on top) has an advantage because target gas ( $H_2$ ) is introduced from the top and conductivity change happens at the top surface first. However, microfabrication of electrodes on the top of the porous sensing materials may introduce defects and/or contaminations. The fabrication steps that involve the use of photoresist, developer and etchants have a chance of damaging or degrading the sensing film. Some of the steps also involve thermocycling, which can lead to compromised properties. The drawback of the structure shown in Fig. 17 (a) (IDEs at the bottom) could be overcome by using a thin sensing film.

The expression of sensitivity, Equation 2.8, could be rewritten by utilizing the Equation 2.17 and 2.18 as:

$$S = \frac{R_a}{R_g} = \frac{I_g}{I_a} = \frac{\int \sigma(x, y) E(x, y) |_{x=0} dy}{\sigma_0 \int E(x, y) |_{x=0} dy} \quad (2.21)$$

where  $I_a$  and  $I_g$  are the current in air and current in  $H_2$ , respectively.  $\sigma_0$  and  $\sigma(x,y)$  are the local conductivity in air and in  $H_2$ , respectively.

In order to obtain the sensitivity of the sensor using Equation 2.21, the local conductivity  $\sigma(x,y)$  should be derived ( $\sigma_0$  is fixed for a given material and can be measured). Modeling of IDEs provide the distribution of  $E(x,y)$ , but do not give the information of  $\sigma(x,y)$ . The diffusion-reaction model shown in next section provides a way to get  $\sigma(x,y)$ .

### 2.3.2 Diffusion-reaction model of gas sensors

The diffusion-reaction model of sensor response was developed by Julian W. Gardner [147-148], especially for  $SnO_2$  gas sensors. The mechanism is based on the following: the target gas is free to diffuse and react chemically at the grain surface, modifying the energy band and the conductance. The mathematical expression for the change in electron concentration is associated with the gas concentration by a power law [147-148]:

$$\Delta n(x, y) = k_1 C_{H_2}^m \quad (2.22)$$

$$n(x, y) = n_0 \cdot [1 + f(C_{H_2})] \quad (2.23)$$

where  $\Delta n(x,y)$  is the change of the electron concentration,  $f(C_{H_2})$  the function of the hydrogen concentration which is controlled by gas diffusion and the properties of the sensing film,  $k_1$  the gas-sensitive parameters,  $m$  a constant, typically,  $0.3 < m < 0.9$ ,  $n(x,y)$  the local concentration of the electrons, and  $n_0$  the concentration of electrons when the sensor is placed in air.

By solving the diffusion equation with boundary conditions,  $f(C_{H_2})$  could be expressed as [148]:

$$f(C_{H_2}) = 1 - \frac{4}{\pi} \sum_{n=0}^{\infty} \frac{(-1)^n}{2n+1} \cdot e^{-D_e(2n+1)^2 \pi^2 t / 4t_0^2} \cdot \cos \frac{(2n+1)\pi \cdot y}{2t_0} \quad (2.24)$$

where  $D_e$  is the effective diffusion coefficient, and  $t_0$  is the thickness of the sensing film.

The local conductivity of the sensing film  $\sigma(x,y)$  is:

$$\sigma(x, y) = \mu q n(x, y) \quad (2.25)$$

where  $\mu$  is the electron mobility and may be considered to be constant ( $\mu = 6.24 \times 10^{-3} \text{ cm}^2/\text{V}\cdot\text{s}$ ) for a pure  $\text{SnO}_2$  film [149].

The sensitivity (S) is derived from Equation 2.21:

$$S = \frac{R_a}{R_g} = \frac{\int_{y=0}^{y=t} \sigma(x, y) E(x, y) \Big|_{x=0} dy}{\sigma_0 \int_{y=0}^{y=t} E(x, y) \Big|_{x=0} dy} = \frac{\int_{y=0}^{y=t} f(C_{H_2}) E(x, y) \Big|_{x=0} dy}{\int_{y=0}^{y=t} E(x, y) \Big|_{x=0} dy} + 1 \quad (2.26)$$

To simplify this expression of sensitivity, the expressions of  $E(x,y)|_{x=0}$  (Equation 2.19) could be replaced by Equation 2.27, which is the electric field of a semi-infinite pair of electrodes with the assumption that the width of electrode is infinite [148]:

$$E_a = \frac{V}{\pi} \left[ (y/t_0)^2 + \frac{g^2}{4t_0^2} \right]^{-\frac{1}{2}} \quad (2.27)$$

The sensitivity, Equation 2.26, becomes [147]:

$$S = \frac{\int_{y/t=0}^{y/t=1} \left\{ F(C_{H_2}) / \left[ (y/t)^2 + (g/2t)^2 \right]^{1/2} \right\} d(y/t)}{\ln \left\{ \left[ 1 + \left( 1 + g^2 / 4t^2 \right)^{1/2} \right] / (g/2t) \right\}} + 1 \quad (2.28)$$

Equation 2.28 shows that the parameters of IDEs do affect the sensitivity. Numerical calculations were carried out based on Equation 2.28 as shown in Fig. 23 [6]. Figure 21 (a) shows the gas concentration profile at various times as the fraction of the diffusion time constant  $t_0^2/D_e$ .  $D_e$  is not known for the In-doped  $\text{SnO}_2$ . If using the value reported in [152],  $D_e$  is  $7.6 \times 10^{-6} \text{ cm}^2/\text{s}$ . So within  $10^{-4}$  seconds, the concentration at the bottom of the sensor reaches 90% of the concentration on the surface when the thickness  $t_0$  is 120 nm. Figure 23 (b) shows the sensitivity versus time with different electrode gap sizes. The size of the gap does affect the sensitivity.



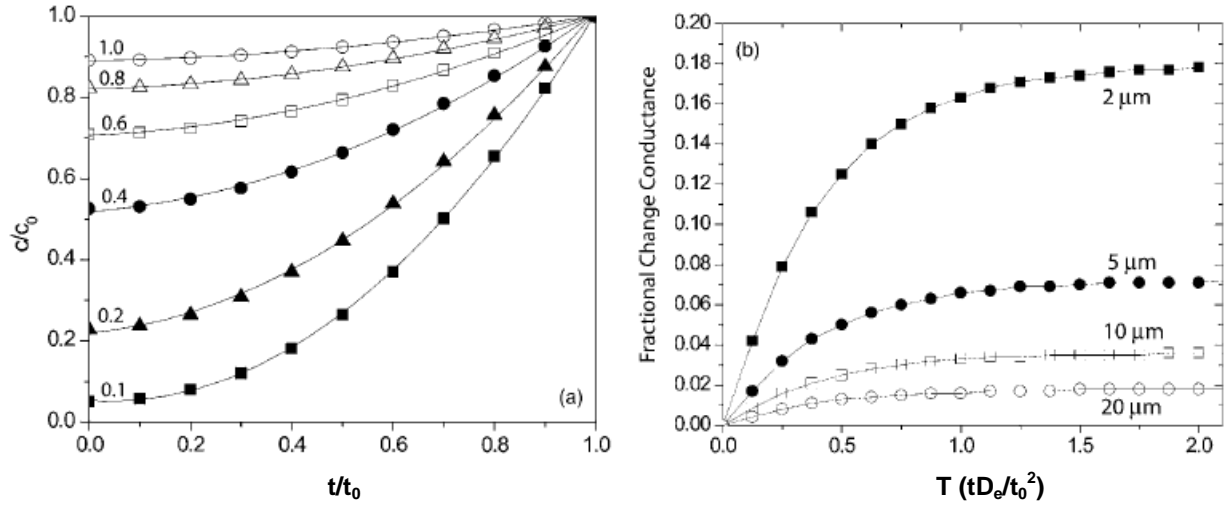


Figure 23: Numerical calculation results on (a) gas concentration inside the sensing film and (b) effects of the electrode gap on fraction change conductance of the sensing film [6].

However, the diffusion-reaction model is based on the thick porous film and the semi-infinite assumption is not suitable for some IDE designs, especially where the electrode width is comparable to other parameters. For a thin sensing film with a limited electrode width, there is a need to find a new model to analyze the sensor's performance.

### 2.3.3 Model analysis on thin film micro-gap sensors

#### 2.3.3.1 Sensitivity

The structure (electrode at the bottom) shown in Fig 16 (a) is used in this work to avoid introducing defects and/or contaminations and to increase the sensing area. Based on the analysis in Section 2.3.1, IDEs can transfer the conductance change to sensing signal more effectively using a thin sensing film. However, when the film thickness is below 200 nm, the porosity drops dramatically [138]. The compact film may reduce the reaction sites and result

in low sensitivity. The optimized thickness is 120 nm according to previous results [138]. In this work, the thickness of the sensing film used in all the devices was controlled to be around 120 nm.

Figure 24 shows the schematic view of the proposed micro-gap sensors and the equivalent circuitry. The thickness of the sensing film and Au electrodes are 120 nm and 200 nm, respectively, for all the micro-gap sensors.

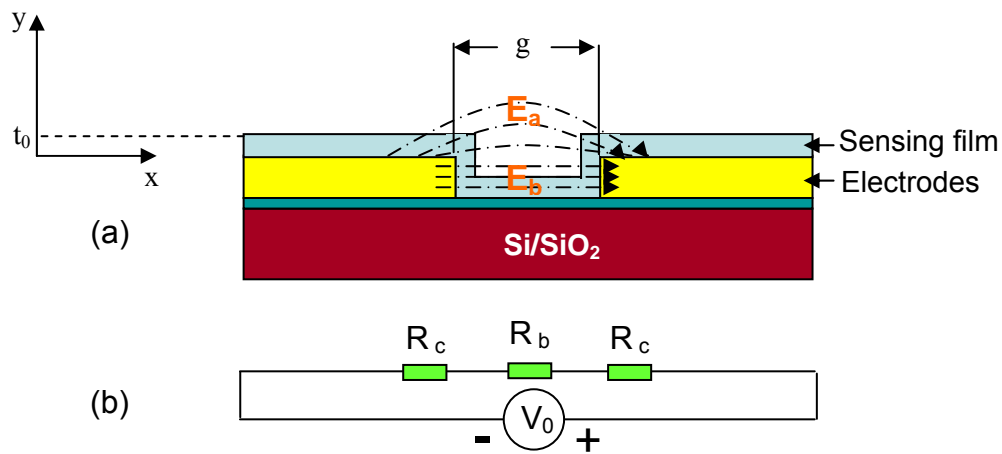


Figure 24: (a) Schematic view of the micro-gap sensor.  $E_a$  and  $E_b$  are the electric fields above and between the electrodes, respectively. (b) equivalent circuitry.

In Fig. 24 (a), because the thickness of the sensing film is smaller than the thickness of the electrodes, some sensing materials are on top of the electrodes and some are in between after a dip-coating process (Details in Chapter 3). As shown in Fig. 25, the electric field on the electrode is weak except at the edges, the sensing material on the electrodes does not contribute much to the total resistance. Most of the current flows through the material between the electrodes, therefore, the resistance of the material on the electrodes is ignorable. Figure 24 (b) shows the simplified equivalent circuitry. The resistance of the device consists of two contact resistances plus the bulk resistance of the sensing film between the electrodes.

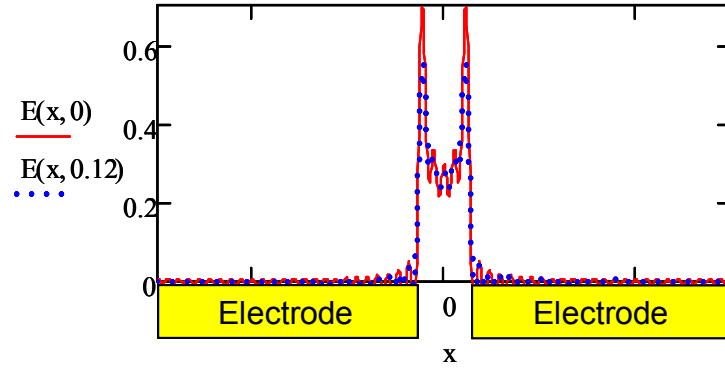


Figure 25: Electric field distribution in the 120 nm thin film on top of the electrodes.  $g$  and  $w$  are  $5\ \mu\text{m}$  and  $50\ \mu\text{m}$ , respectively.

Because the grain size of the In-doped  $\text{SnO}_2$  was measured to be 10 nm, the grain boundary control model (See Section 1.3.1) is applied. A one-dimension model [153] is shown in Fig 26.

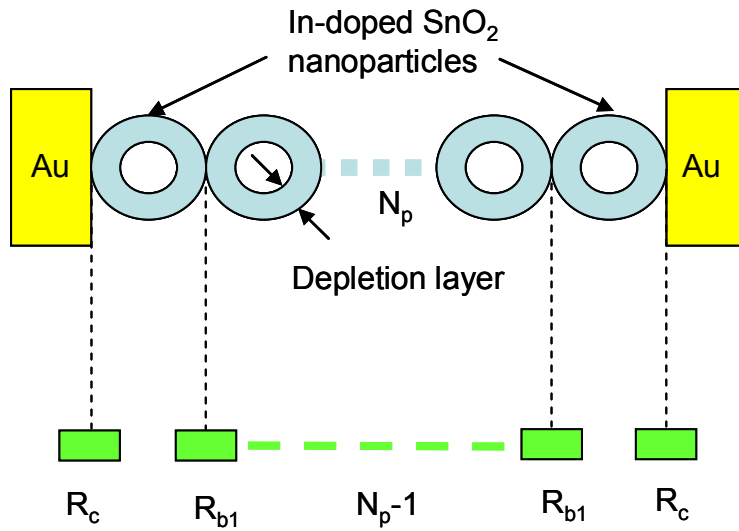


Figure 26: Schematic view of a one-dimension conduction model of the hydrogen sensor.  $N_p$  and  $R_g$  are the number of the nanoparticles and resistance at each grain-grain boundary, respectively.

The total resistance  $R_t$  and the bulk resistance  $R_b$  are:

$$R_t = 2R_c + (N_p - 1)R_g \quad (2.29)$$

$$R_b = (N_p - 1)R_g \quad (2.30)$$

So the sensitivity derived from 2.8 is:

$$S = \frac{R_a}{R_g} = \frac{R_{t-a}}{R_{t-g}} = \frac{2R_{c-a} + (N_p - 1)R_{g-a}}{2R_{c-g} + (N_p - 1)R_{g-g}} = \frac{2}{2 + (N_p - 1) \frac{R_{g-g}}{R_{c-g}}} S_c + \quad (2.31)$$

$$\frac{(N_p - 1)}{2 \frac{R_{c-g}}{R_{g-g}} + (N_p - 1)} S_g$$

$$S_c = \frac{R_{c-a}}{R_{c-g}} \quad (2.32)$$

$$S_g = \frac{R_{g-a}}{R_{g-g}} \quad (2.33)$$

where  $R_{c-a}$  and  $R_{c-g}$  are the contact resistances in air and in hydrogen gas, respectively.  $R_{g-a}$  and  $R_{g-g}$  are the grain-grain interface resistances in air and in hydrogen gas, respectively.  $S_c$  and  $S_g$  are the sensitivity of the contact and grain-grain interface, respectively.

All of the eight unknowns,  $S$ ,  $R_{c-a}$ ,  $R_{c-g}$ ,  $R_{g-a}$ ,  $R_{g-g}$ ,  $S_c$ ,  $S_g$  and  $N_p$ , can be measured or calculated. The advantage of the model is it involves the effects of contact resistances at the

electrode/material interfaces which helps understand the sensors performance and optimize the sensor design..

### 2.3.3.2 Response time

In the diffusion-reaction model (Section 2.3.2), the response time is controlled by the diffusion time in the thick film. For the particular In-doped SnO<sub>2</sub> nanoparticle thin film, there is no data for the diffusion constant. It is unknown how long the diffusion process will be. Considering the sensitivity of most of the proposed micro-gap sensors in this work are larger than 1,000, the diffusion might not be the controlling factor of the response time ( $t_r$ ). For the micro-gap sensors (Fig. 24 (a)), the electric field between electrodes is uniform. If the material between the electrodes is divided into 12 uniform layers with a thickness of 10 nm, the resistances of each layer is equal, due to the uniform electric field  $E_b(x,y)$ .

It is reasonable to divide the sensing film into 12 layers because the total thickness of the film is 120 nm and nanoparticle size is around 10 nm. The total resistance ( $R_t$ ) is expressed as:

$$\frac{1}{R_t} = \sum_{n=0}^{11} \frac{1}{R_{bn}} \quad (2.34)$$

where  $R_{bn}$  is the bulk resistance of the nth layer.

Assume in the time interval  $\Delta t$ , chemical reactions induced by the introduction of H<sub>2</sub> are completed (in equilibrium status) in the first (top) layer and the resistance of the first layer,  $R_{b0}$ , drops to its saturated value. The total resistance change in  $\Delta t$  is shown in Fig.27.

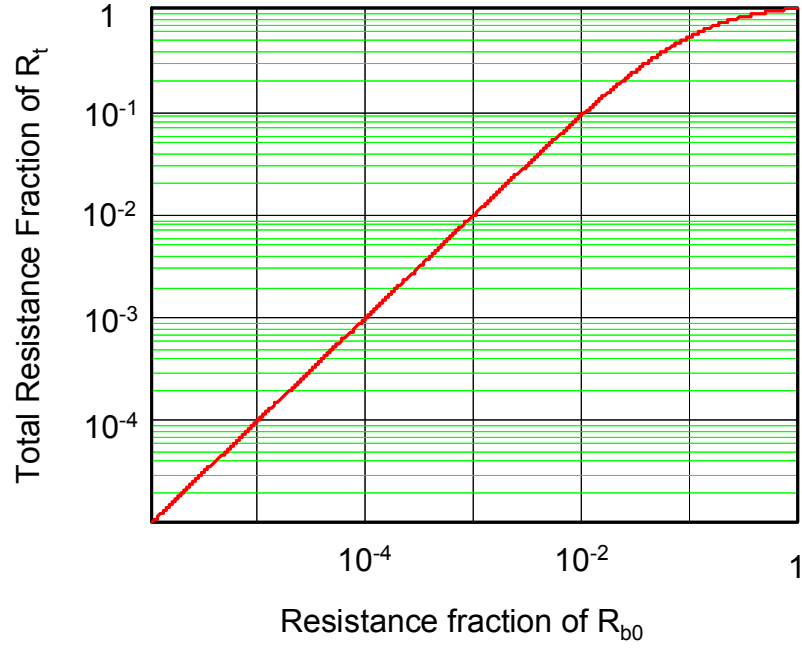


Figure 27: Total resistance change Vs. the resistance change of the first layer in  $\Delta t$ .

Figure 27 shows that if the sensitivity is larger than 100, in  $\Delta t$ , the  $R_{b0}$  drops to less than  $10^{-2}R_{b0}$ , and the total resistance change is more than one order of magnitude. So the response time ( $t_r$ ), is not larger than  $\Delta t$ . Obviously, the time to reach the saturated resistance in  $H_2$  is determined by diffusion, but according to the definition of the response time,  $t_r$  is not controlled by the diffusion but is determined by the chemical reactions on the top surface of the sensing film.

#### 2.3.4 Model analysis on thin film nano-gap sensor

For the nano-gap sensors, the dimension of the IDEs are comparable to the thickness of the sensing film (120 nm) as shown in Fig 28.

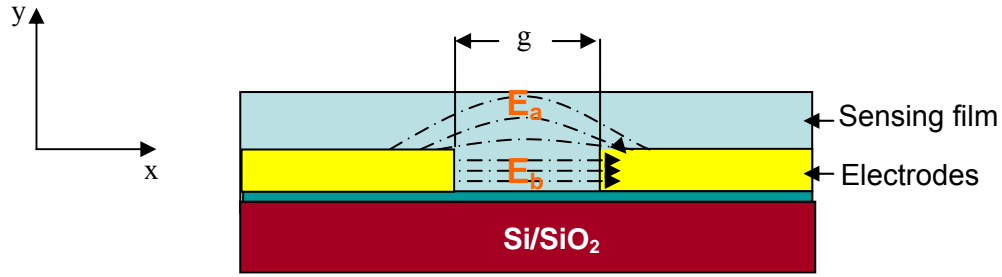


Figure 28: Schematic view of the nano-gap sensors with an electrode thickness ( $t_{Au}$ ) of 50 nm and a sensing film thickness of 120 nm. Sensing film with a thickness of 70 nm is on top of the IDEs.

For IDEs with 5 nm in gap and 5 nm in width, the distribution of the electric field above the electrode is not uniform as shown in Fig 29.

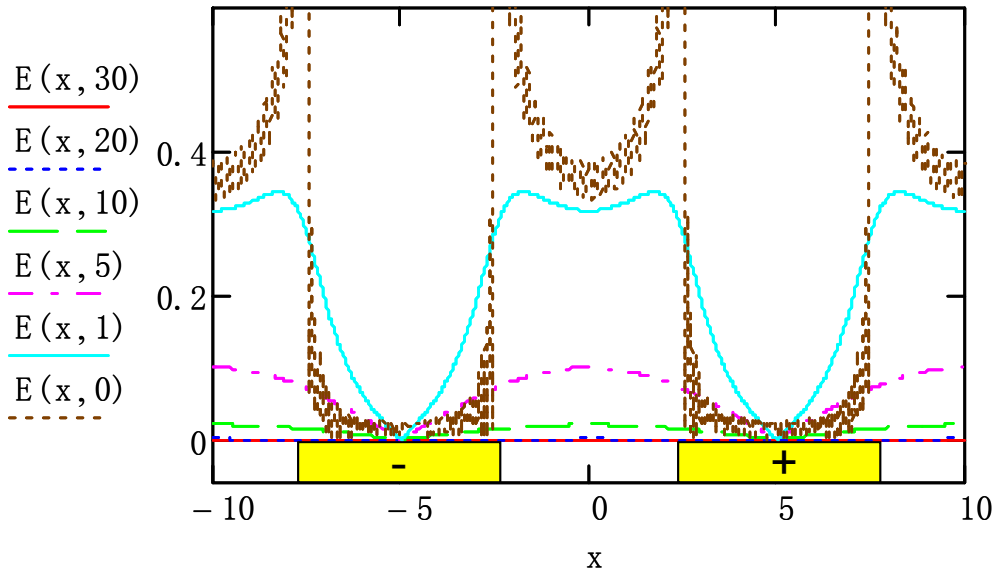


Figure 29: Electric field distribution above the IDEs with 5 nm in gap and 5 nm in width.

In Fig 29, when the height ( $y$ ) is larger than 5 nm, the electric field is very weak. The same phenomenon discussed in Section 2.3.1 happens, i.e., most of the current flows through the layer within the thickness of 5 nm above the IDEs. The nano-gap sensors have to wait for the hydrogen to diffuse from the top to the bottom layer in order to obtain good sensitivity.

This increases the response time, therefore, a larger width and/or a larger gap are desirable for nano-gap sensors

For the IDEs with 1000 nm in finger width and 100 nm in gap, the electric field above the electrodes is shown in Fig 30 and the current contribution from layers with different thickness is shown in Fig 31.

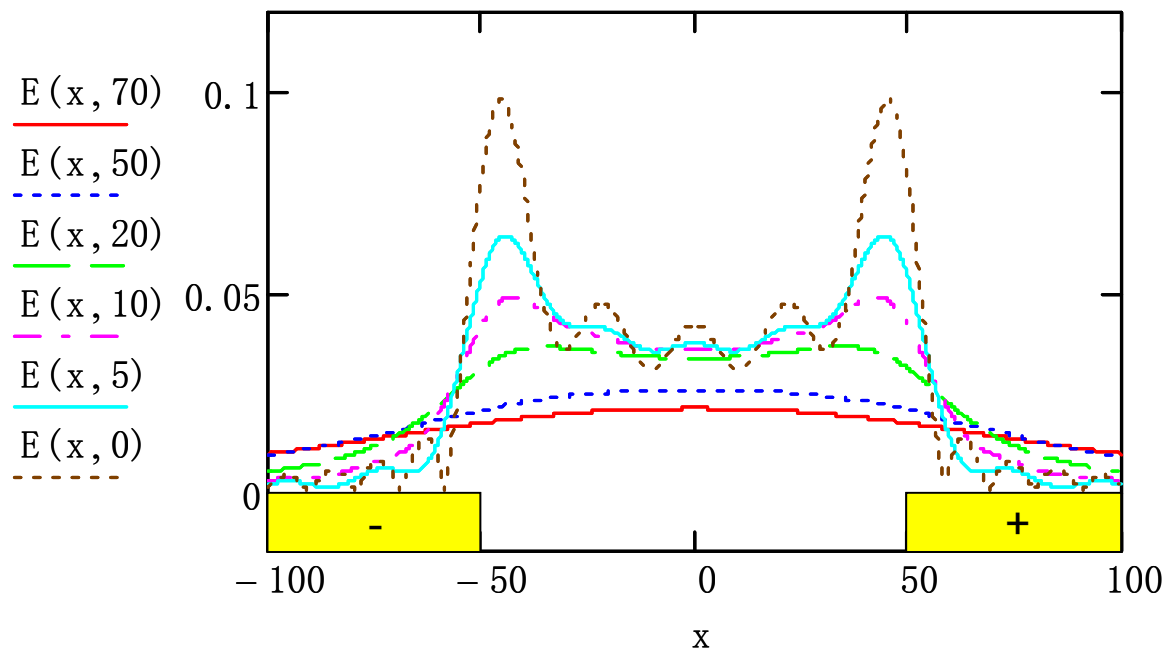


Figure 30: Electric field above the electrodes with 100 nm and in gap 1000nm in width.



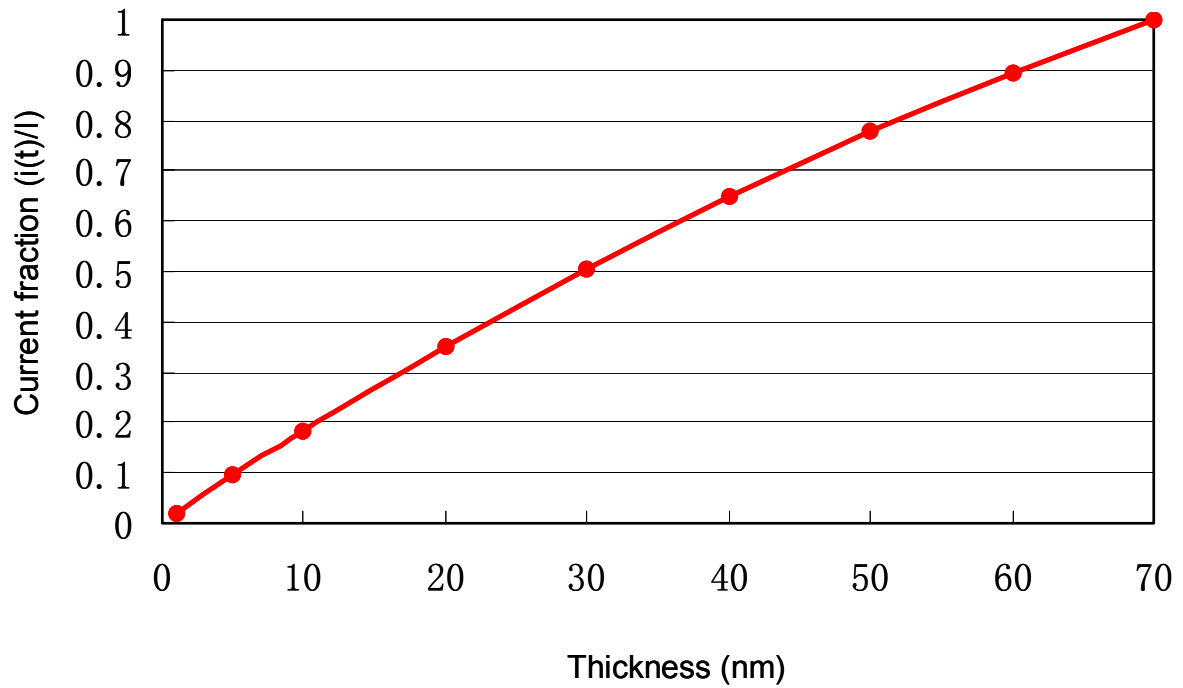


Figure 31: Current fraction in the layer with thickness of  $t$ .

As show in Fig.30, the distribution of the electric field in the film (70 nm in thickness) above the electrodes are relatively uniform compared to Fig 29. The current fraction is linear with thickness of the sensing film, which means the conductivity change on the top surface of the sensing film could be converted to sensing signal, effectively contributing to fast response.

As showed in Fig. 28, in the nano-gap sensors, the sensing film above the IDEs can not be ignored like with micro-gap sensors, because electrons can take a different path to reach the cathode, bypassing the area between the electrodes. The sensitivity for the nano-gap sensors derived from Equation 2.21 becomes:

$$S = \frac{R_a}{R_g} = \frac{\int_{y=0}^{y=t} \sigma(x, y) E(x, y) dy}{\sigma_0 \int_{y=0}^{y=t} E(x, y) dy} = \frac{\int_{y=-t_{Au}}^{y=0} \sigma(x, y) E_b(x, y) dy + \int_{y=0}^{y=t_0-t_{Au}} \sigma(x, y) E_a(x, y) dy}{\sigma_0 \int_{y=-t_{Au}}^{y=0} E_b(x, y) dy + \sigma_0 \int_{y=0}^{y=t_0-t_{Au}} E_a(x, y) dy} \quad (2.35)$$

The sensitivity (S) is related to the parameters of the electrodes due to E<sub>a</sub> and E<sub>b</sub>. Unfortunately, the trend of how these parameters affect the sensitivity is not clear from the complex Equation 2.35 for the nano-gap sensors. Real experiments are needed to explore the relationship and to improve the sensors performance.

## CHAPTER 3 FABRICATION AND TESTING OF HYDROGEN MICRO SENSORS

As discussed in Chapter 2, in order to verify the validity of identified design parameters based on theoretical analysis and measure the sensor characteristics empirically, hydrogen sensors were fabricated and tested. This provides insight into the effects of design parameters of IDEs on the sensor performance due to the unknown local conductivity ( $\sigma(x,y)$ ) changes.

### 3.1 Fabrication of micro sensors

Using microfabrication techniques, the IDEs were fabricated starting with a silicon substrate.

The parameters of IDEs were:

$g$  (gap between electrodes): 2 ~ 20 microns,

$l$  (length of a finger): 100 ~ 1000 microns, and

$w$  (width of a finger): 5 ~ 50 microns.

$N$  (total number of fingers in one electrode): 8.

Figure 32 shows the fabrication steps of the sensors.

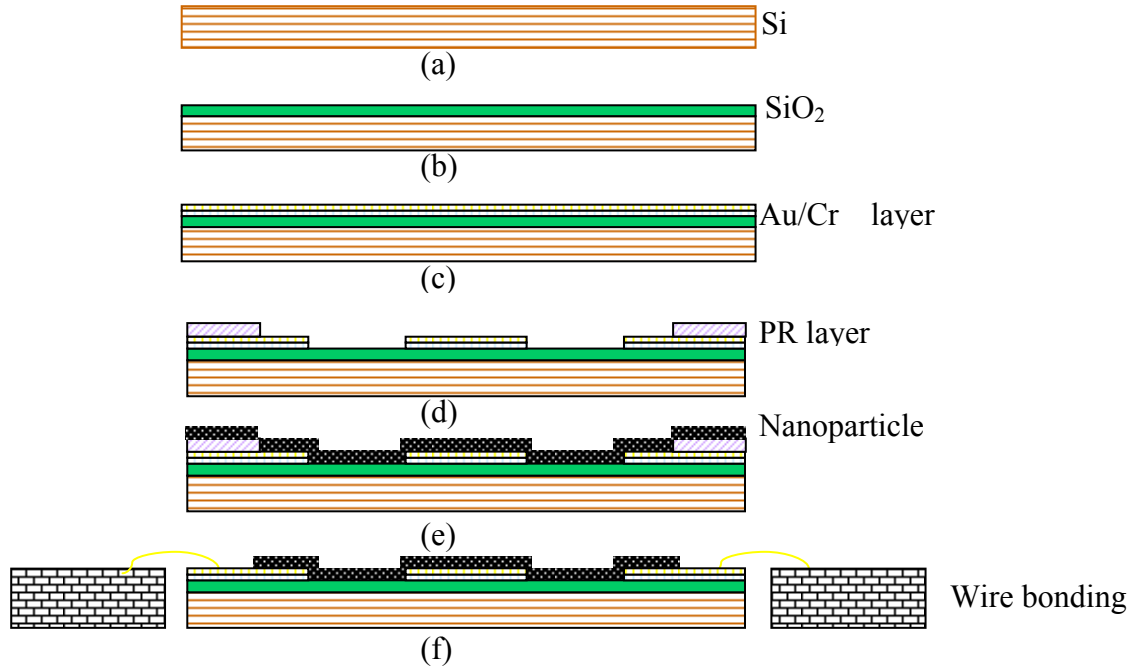


Figure 32: Fabrication steps: (a) Si wafer cleaning, (b) Thermal oxidation, (c) Au/Cr deposition, (d) Electrode patterning, (e) Nanoparticle deposition, and (f) Packaging.

A 3" single-side polished Si wafer (n-type, (100) orientation,  $380\ \mu\text{m} \pm 25\ \mu\text{m}$ , University Wafers) was used as the substrate. The wafer was cleaned with acetone, methanol and deionized (DI) water in sequence and dried by nitrogen gas ( $\text{N}_2$ ). Acetone was used to remove organic contaminations. Methanol and DI water were used to dissolve acetone and methanol, respectively. Serving as an insulation layer, silicon dioxide ( $\text{SiO}_2$ ) with the thickness of 500 nm was thermally-grown on top of the Si wafer by the wet oxidation process at  $1100^\circ\text{C}$  for 1 hour. 20 nm-thick Chromium (Cr) and 200-nm thick gold (Au) layers were deposited on the wafer by thermal evaporation as the electrode material in sequence. This thin Cr layer (20 nm) worked as the adhesion layer for Au. 1.2  $\mu\text{m}$ -thick positive photoresist (PR) (Shipley 1813) was spin-coated on the wafer at 3000 RPM for 30 seconds. PR was baked at  $100^\circ\text{C}$  in oven for 3 minutes to remove the solvent. After cooling down to room temperature, the wafer was mounted on the mask aligner (EVG620 double-side mask aligner,

EV Group Corp.) for patterning. IDEs patterns were transferred from the mask to the PR by UV-lithography with dosage of  $120 \text{ mW/cm}^2$ . After developing in the developer (CD-26) for 1 minute, the wafer was dried by  $\text{N}_2$  and the patterns in PR were checked with a microscope. The exposed Au/Cr was removed by wet chemical etching with PR as the etching mask. The Au etchant consisted of 4 g Potassium iodide (KI), 1 g Iodine ( $\text{I}_2$ ) and 40 ml DI water. The Au etching rate was 200 nm/min at room temperature. The commercial Cr etchant from Micron was used to remove the Cr layer. The Cr etching rate was 40 micron/min at  $40^\circ\text{C}$ . When the etching was done, IDEs patterns were checked again with the microscope. Then, the PR on the Au/Cr IDEs was removed by acetone. Oxygen plasma was applied to remove the PR residue on Au/Cr electrodes to obtain clean surfaces. The wafer was diced and ready for In-doped  $\text{SnO}_2$  coating.

The In-doped  $\text{SnO}_2$  nanoparticle thin films were prepared by Dr. Seal's group at UCF [134-135]. The sol-gel dip-coating method was used to deposit the In-doped  $\text{SnO}_2$  on the MEMS sensor platforms. The tin-isopropoxide ( $\text{Sn}[\text{OC}_3\text{H}_7]_4$ ) (10%, w/v) solution in isopropanol (72 vol%) and toluene (18 vol%), corresponding to the concentration of 0.23M of tin-isopropoxide, was used with the addition of calculated amount of indium(III)-isopropoxide ( $\text{In}[\text{OC}_3\text{H}_7]_3$ ) to obtain the solution of 6.5 mol % In-doped  $\text{SnO}_2$ . After one dip-coating step, a 65-nm thick film was deposited on the MEMS sensor chips. The coated chips were dried at  $150^\circ\text{C}$  for 30 min in the oven. The dip-coating and drying process were repeated one more time to obtain the 120 nm-thick film. Pt nanoclusters were deposited on the sensors by sputtering (sputter coater, K350, Emitech Ltd.) for 10 seconds as the catalyst. The sensors were baked at  $400^\circ\text{C}$  in oven for 1 hour. After cooling down to room

temperature, the sensors were inspected by AFM (Atomic Force Microscopy) and packaged for hydrogen testing.

Figure 33 shows a typical AFM image of the In-doped  $\text{SnO}_2$  nanoparticle thin film on the sensor surface. The size of the nanoparticles was established to be 10 nm. The film was porous with a large surface to volume ratio, which is expected to contribute to the high sensitivity. The sensors were wire-bonded to a 32-pin dual line ceramic package as shown in Fig 34 for testing.

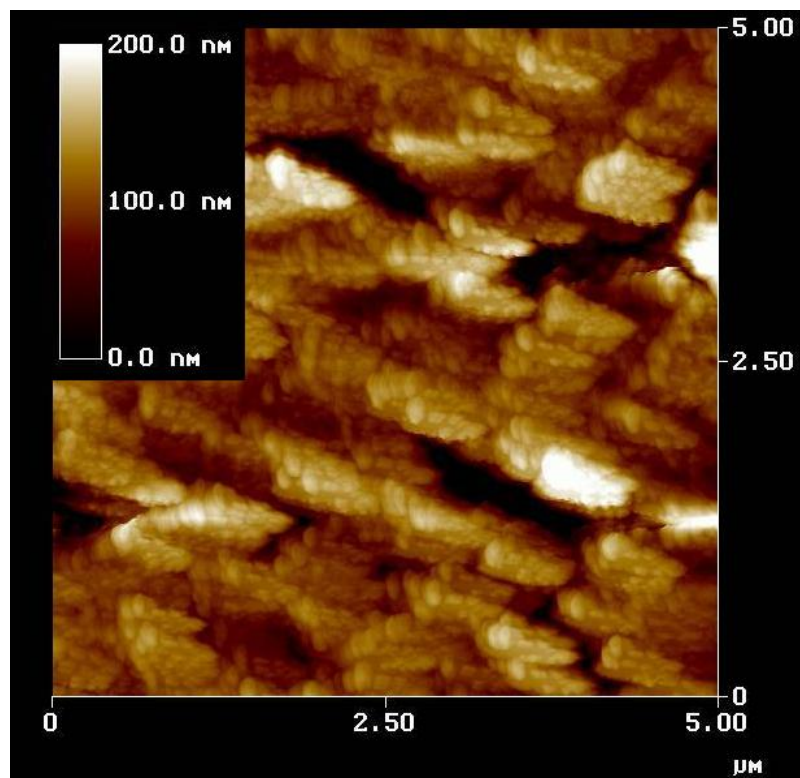


Figure 33: AFM image of In-doped  $\text{SnO}_2$  nanoparticles on the sensor surface.

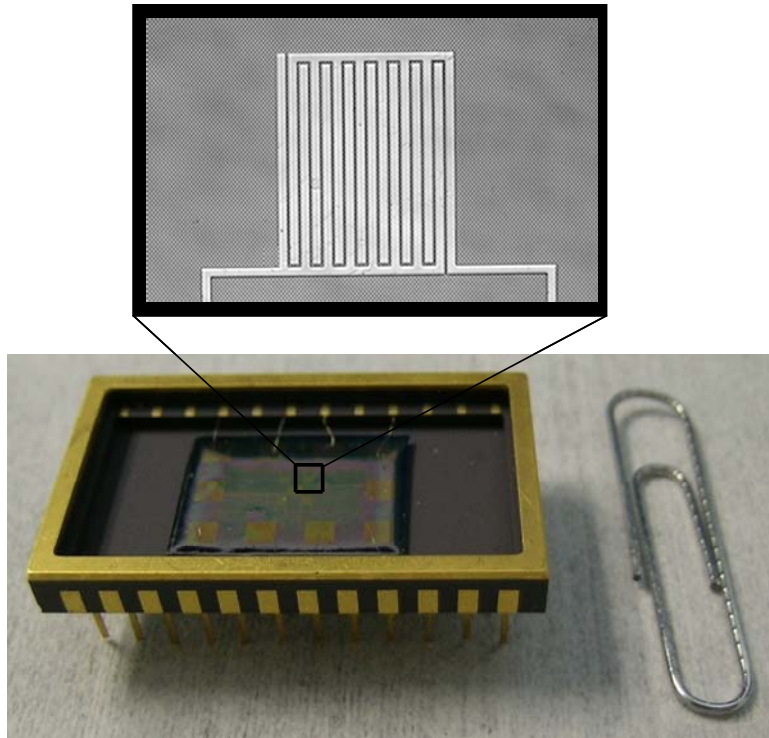


Figure 34: Packaged sensors showing interdigitated electrodes.

### 3.2 Testing of the micro-gap sensors

All the testing was carried out at the room temperature (22 °C) in a 50-litre testing chamber with the applied voltage of 10 volts. Air pressure within the test-chamber was maintained at 50 Torr using a turbo-pump. Mass-flow-controllers were used to regulate the volume of nitrogen (N<sub>2</sub>) and hydrogen (H<sub>2</sub>) into the test-chamber. The sensors were tested at hydrogen concentrations ranging from 9 ppm (parts per million) to 900 ppm. Figure 35 shows a schematic of the test setup.

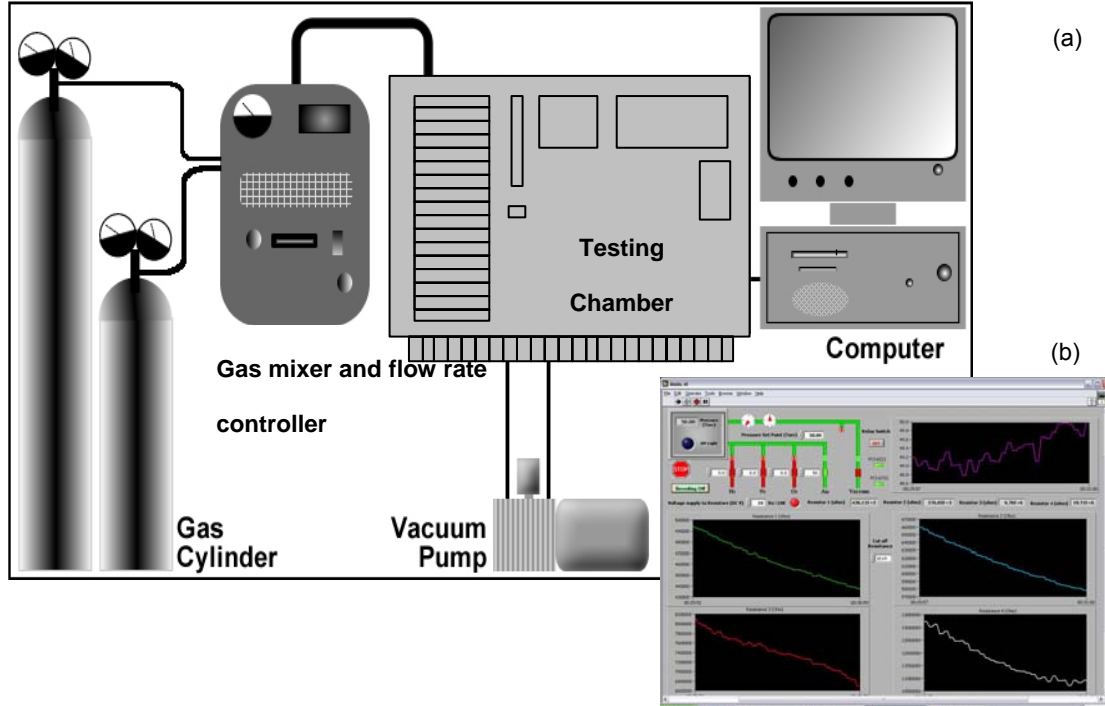


Figure 35: (a) Schematic illustration of a test setup for hydrogen sensors and (b) software interface for control and measurement.

The test setup includes gas ( $H_2$  and  $N_2$ ) cylinders, a gas mixer, flow rate controllers, the 50-litre test-chamber and a computer. The resistances of up to 4 sensors could be monitored at the same time.

A typical testing result of a hydrogen micro sensor with 5  $\mu m$  in gap at room temperature is shown in Fig. 36. When hydrogen gas was introduced into the testing chamber at time  $t_1$ , the resistance dropped dramatically with the drop rate of 827  $K\Omega/sec$ . At  $t_2$ , the resistance dropped by one order of magnitude. The response time,  $t_r$  could be calculated as:

$$t_r = t_2 - t_1 \quad (3.1)$$



After the resistance dropped to its saturated (minimum) value at  $t_3$ , hydrogen gas was stopped and compressed air was introduced. Then, the resistance started to increase and finally recovered.

The sensitivity ( $S$ ) was calculated as:

$$S = \frac{R_{t_1}}{R_{t_3}} \quad (3.2)$$

where  $R_{t_1}$  and  $R_{t_3}$  are the resistance values at time  $t_1$  and  $t_3$ , respectively.

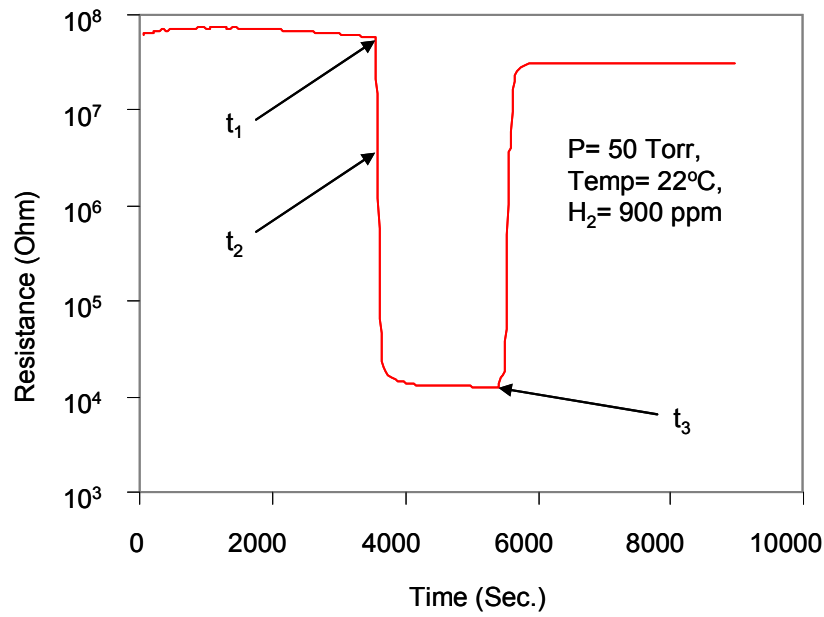


Figure 36: A typical testing result of a MEMS hydrogen sensor. The gap, length and width of fingers are  $5\text{ }\mu\text{m}$ ,  $1000\text{ }\mu\text{m}$ , and  $50\text{ }\mu\text{m}$ , respectively.

### 3.2.1 Gap effect

Figure 37 shows the trend of the gap effects on sensitivity. All the sensors have the same parameters ( $W = 50 \text{ } \mu\text{m}$ ,  $l = 1000 \text{ } \mu\text{m}$  and  $N = 8$ ) except the gap size. In Fig. 37, the sensitivity increases with an increase in gap. For the gap size of  $20 \text{ } \mu\text{m}$ , the highest sensitivity of 70,000 was achieved. A larger electrode gap means a larger sensing area and more available reaction sites. As seen in Reaction 2.7, more  $\text{O}_{\text{ads}}^-$  ions will drive the reaction in the forward direction and more electrons can be generated contributing to the resistance drop. In Fig. 13 (in Chapter 2), the  $50 \text{ } \mu\text{m}$ -gap sensors showed the sensitivity of 2200 which is less than that of the  $20 \text{ } \mu\text{m}$ -gap sensor because in the  $50 \text{ } \mu\text{m}$ -gap sensor,  $N$  is 4 and  $l$  is  $500 \text{ } \mu\text{m}$ . The sensing area is much smaller than that of a  $20 \text{ } \mu\text{m}$ -gap sensor.

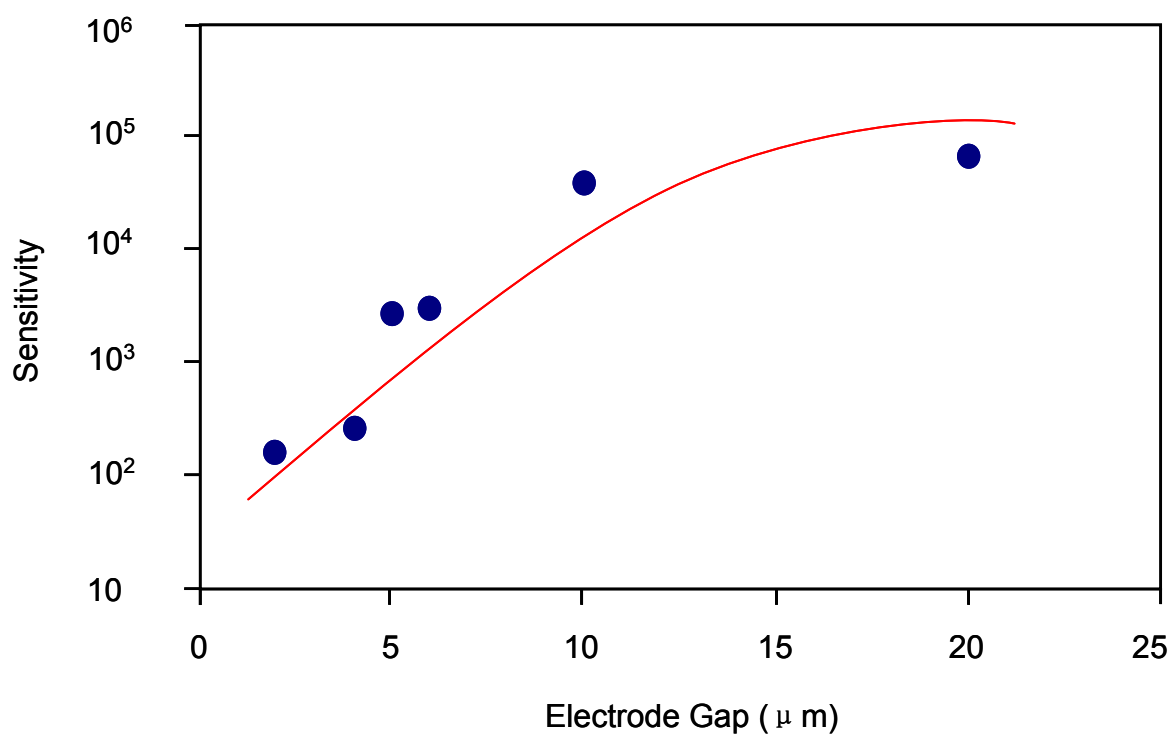


Figure 37: Effect of the electrode gap on the sensitivity of the micro-gap sensors.

Although the increased gap results in a larger sensitivity, there is a limitation in this trend. A larger gap increases the length of current path and free electron losses due to electron trapping at defect sites and scattering at various scattering centers. That is why the macro sensor (showed in Fig. 11 in Chapter 2) with 1 cm gap and much large sensing area showed a poor sensitivity of less than 0.5.

The effect of the gap size on the response time is showed in Fig.38. Sensors with the smaller gap exhibited faster response. The main reason for this can be found in a high electric field ( $E(x,y)$ ), which assists Pt to dissociate  $H_2$ . As discussed in Takahashi et al.'s work [152], when the electric field is above  $10^2 V/cm$ , Pt is found to be very effective at facilitating  $H_2$  dissociation into protons. Extra protons generated could drive the Reaction 2.3 and 2.7 to the forward direction to generate more free electrons. The higher the electric field, the more  $H_2$  is dissociated and hence the faster the resistance drop. For the interdigitated electrodes of the sensors, with a smaller electrode gap, a higher electric field (Equation 2.13) is generated under a fixed measuring potential, therefore, it is believed that the faster resistance drop happens in smaller gap sensors, showing a shorter response time.

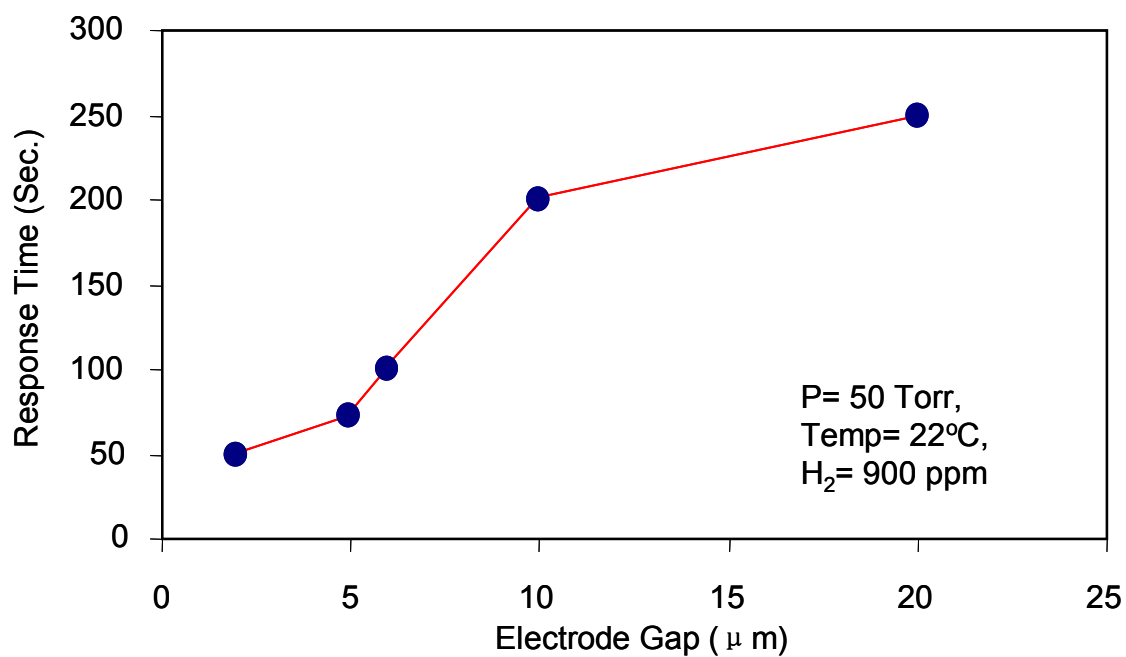


Figure 38: Effect of the electrode gap on the response time.

### 3.2.2 Length effect

Figure 39 and 40 show the length effects on sensitivity and response time, respectively. Because a longer electrode means a larger sensing area, the sensitivity increases with the length. There is no significant change in response time due to the constant gap size.

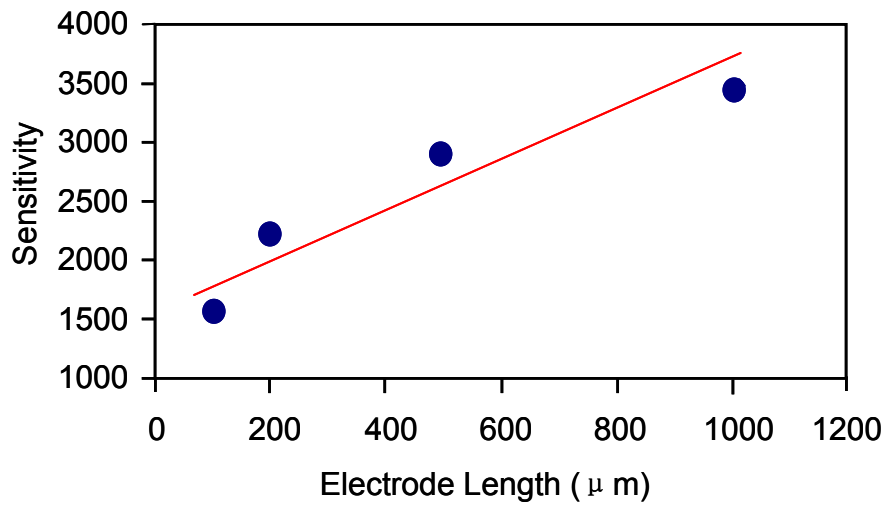


Figure 39: Effect of the electrode length on the sensitivity.

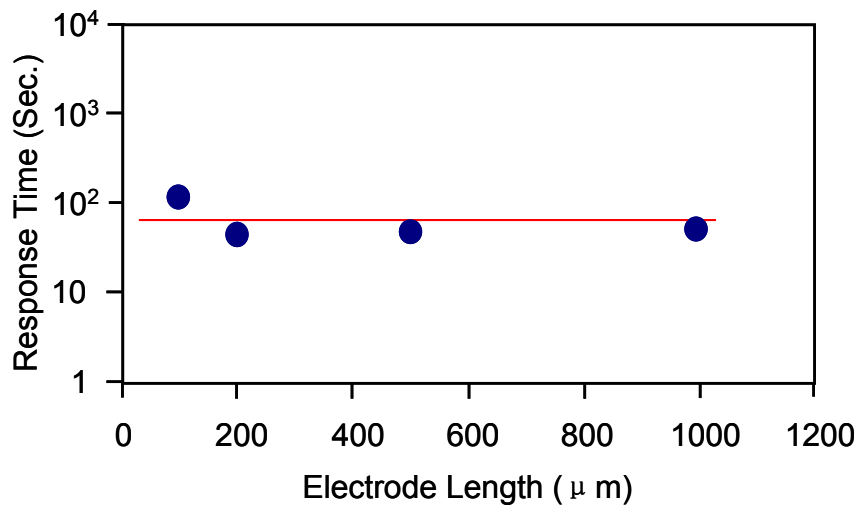


Figure 40: Effect of sensor electrode length on the response time.

### 3.2.3 Width effect

When hydrogen atoms penetrate the sensing film and accumulate at the interface of electrodes (Au) and the sensing film, the work function of the electrode is tuned. This results

in a change of height of the potential barriers at the interface. The contact resistance will change when the sensor is exposed to H<sub>2</sub> gas resulting in the change of sensitivity at the electrode/material interface [128, 130-132].

The effect of width was studied using sensors with 5 μm in gap but with a different finger width (5μm, 10μm and 50μm). As shown in Table 1, sensitivity increases with width of the electrodes. It is also found in Table 1 that the initial resistance (R<sub>a</sub>) increased with the width and the saturated resistance (R<sub>g</sub>) in H<sub>2</sub> decreased with the width. Obviously, according to the definition of the sensitivity, sensitivity increases with width. To understanding this trend, the one-dimension model introduced in Section 2.3.3.1 was applied. R<sub>a</sub> and R<sub>g</sub> are redefined as:

$$R_a = 2R_{c-a} + R_{f-a} \quad (3.3)$$

$$R_g = 2R_{c-g} + R_{f-g} \quad (3.4)$$

where R<sub>f-a</sub> and R<sub>f-g</sub> are the resistances of the sensing film between the electrodes in air and in H<sub>2</sub>, respectively.

Considering that both R<sub>f-a</sub> and R<sub>f-g</sub> should be the same for all the three sensors due to the same gap size (as discussed in Section 2.3.3.1), it is deduced from the Equation 3.3 and 3.4 that R<sub>c-a</sub> increases with the width in air and R<sub>c-g</sub> decreases with the width in H<sub>2</sub>. According to the definition of the sensitivity (S<sub>c</sub>) at the interface of the electrode and material (Equation 2.32), S<sub>c</sub> increases with the electrode width.

The total sensitivity ( $S_t$ ) originates from the contributions of the sensitivities of the interface and sensing film [151]. The larger sensitivity of the interface induced by wider electrodes, contributes to the larger sensitivity.

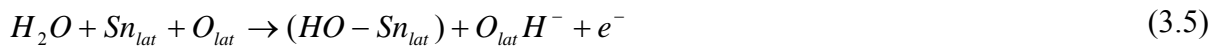
Table 1 Sensitivity and resistances of 5  $\mu\text{m}$  gap sensors with various width.

Sensor #	1	2	3
Width	5	10	50
Sensitivity	482	515	3600
Initial resistance	34 $\text{M}\Omega$	56 $\text{M}\Omega$	83 $\text{M}\Omega$
Saturated resistance in $\text{H}_2$	110 $\text{K}\Omega$	98 $\text{K}\Omega$	22 $\text{K}\Omega$

### 3.2.4 Humidity effect

The variation of the initial sensor resistance ( $R_a$ ) due to humidity was observed in our experiments as shown in Fig.41. In the testing, the environment humidity was measured as 55%. Right after the vacuum was applied, the initial resistance increased sharply. It is believed that the increase in  $R_a$  is due to the decrease in humidity. Within 1 minute, the vacuum reached 50 Torr and the humidity was monitored at 14%. In the following 8 hours, the resistance increased to 100  $\text{M}\Omega$  slowly and the humidity was reduced to 12%. Reducing the vacuum to 5 Torr, the resistance increased but became unstable. When 55 % humidity was introduced, the resistance dropped dramatically by more than two orders of magnitude. This testing result clearly showed the influence of the humidity on the initial resistance of the

sensor. It is well known that H<sub>2</sub>O acts like a reducing gas to SnO<sub>2</sub> to reduce the resistivity [129-130, 144, 153–155]. Two mechanisms have been suggested [153]: (1) Water molecules are adsorbed on the SnO<sub>2</sub> surface and become dissociated into OH<sup>-</sup> and H<sup>+</sup>; they bind themselves to lattice Sn<sub>lat</sub> and O<sub>lat</sub>, respectively, and release a free electron. The reaction is given as [153]:



(2) After H<sub>2</sub>O is adsorbed and dissociated on SnO<sub>2</sub> surface, the H<sup>+</sup> reacts with lattice O<sub>lat</sub> to form another OH<sup>-</sup> group. Two OH<sup>-</sup> groups bind with 2 lattice Sn<sub>lat</sub> and generate a surface oxygen vacancy [153]:



Oxygen vacancies could diffuse inside of SnO<sub>2</sub> acting like donors:





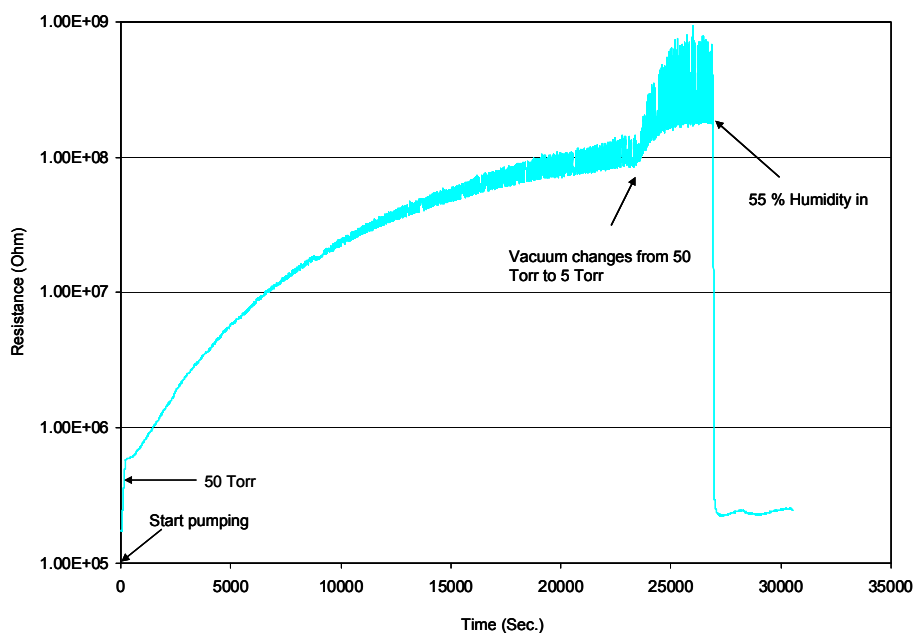


Figure 41: Initial resistance change in vacuum and humidity.

Though both of the mechanisms are based on the high temperature (400 K) assisted water dissociation [153], dissociation of water molecules could happen at low temperature [154]. The resistance change in humidity at room temperature was reported in Ref [155] and observed in our own experiments.

With the increase in humidity, water molecules could condense and form liquid water. The conduction mechanism becomes electrolytic depending on the porosity of the film.  $H^+$ ,  $OH^-$  and  $H_3O^+$  in the water layer are the main carriers in this case.

In this work, a porous thin PMMA (polymethylmethacrylate) layer was used to partially prevent humidity effects due to its water adsorption ability. Figure 42 shows that the PMMA coating did reduce the effect of humidity on resistance. In Fig. 42, when 55% humidity was introduced, the resistance of the uncoated sensor dropped by more than two orders of

magnitude. For the PMMA-coated sensor, the drop was less than one order of magnitude and this proved that a PMMA coating can reduce the humidity effect significantly.

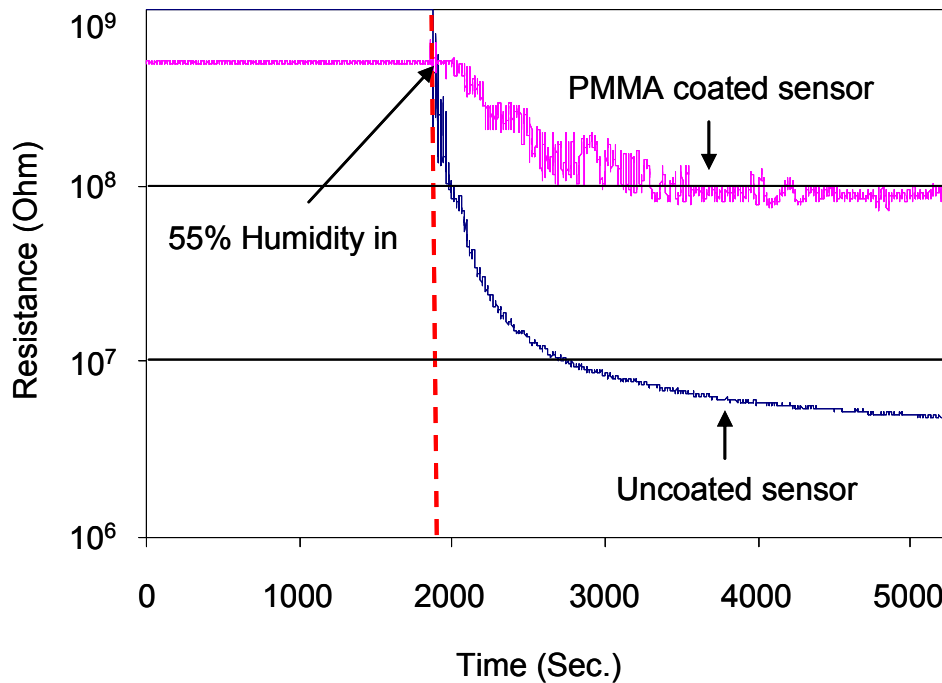


Figure 42: Humidity effect on PMMA coated and uncoated sensors.

The hydrogen sensing response of the PMMA-coated sensor was tested and is shown in Fig. 43. When hydrogen was present, the resistance dropped dramatically and recovered after hydrogen was stopped and air was introduced. The PMMA-coated sensor showed good sensor response with PMMA coating. This is believed to be due to the PMMA coating, which could block water molecules and let the hydrogen molecules pass.

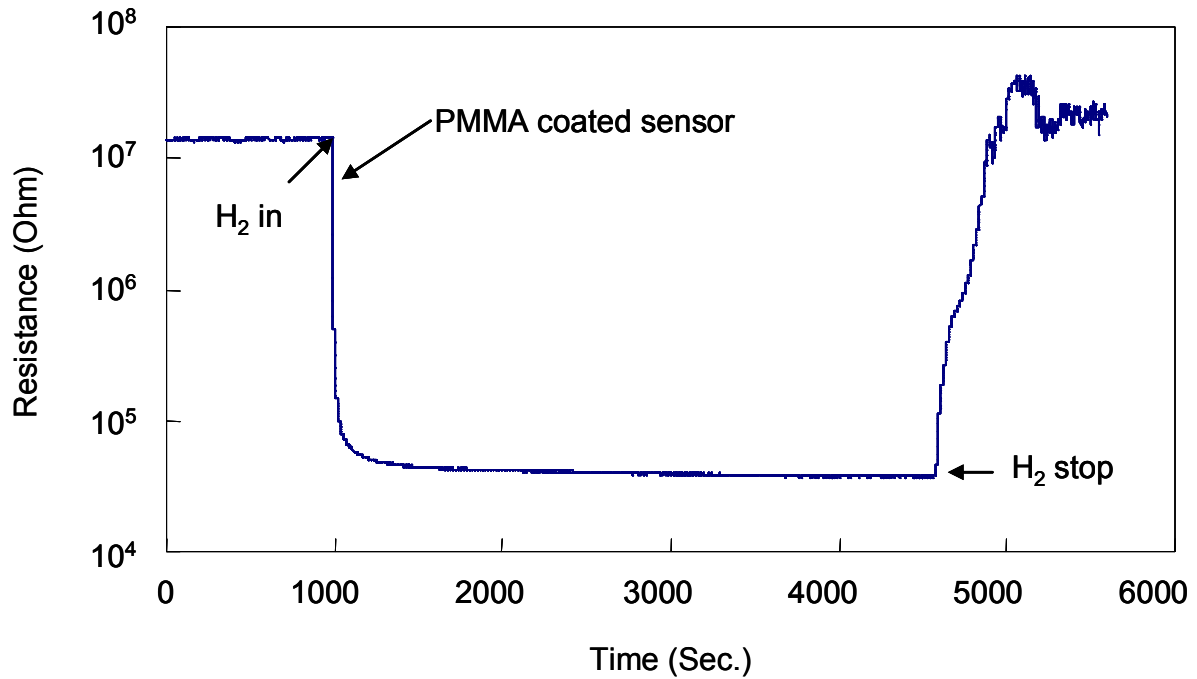


Figure 43: Comparison of the sensors with and without PMMA coating.

### 3.3 Portable Instrument

A portable hydrogen detection instrument was designed based on a linear response of the fabricated hydrogen sensors. Figure 44 shows the devices fabricated for a portable instrument. In Fig 44 (a), 112 sensors were fabricated on a 3" Si wafer. A diced single chip with a size as small as 3 mm × 3 mm is shown in Fig 44 (b). Figure 44 (c) shows a packaged micro sensor, which is ready for insertion in the portable instrument. The details of the IDEs structure are shown in Fig. 44 (d). The sensor response to various concentrations was tested as shown in Fig. 45. The sensor could detect H<sub>2</sub> with a concentration as low as 9 ppm, and the sensitivity increased linearly with the concentration from 9 ppm to 900 ppm. This linear response and low detection limit make the sensor attractive for portable instruments.

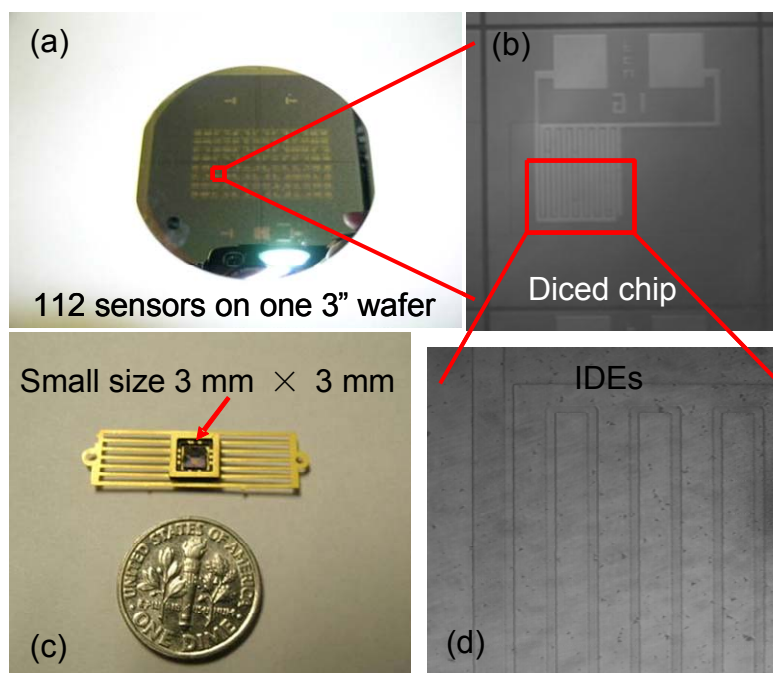


Figure 44: MEMS sensors fabricated for a portable hydrogen instrument: (a) wafer level view, (b) a diced chip (3 mm x 3 mm), (c) enlarged view of IDEs, and (d) a packaged sensor.

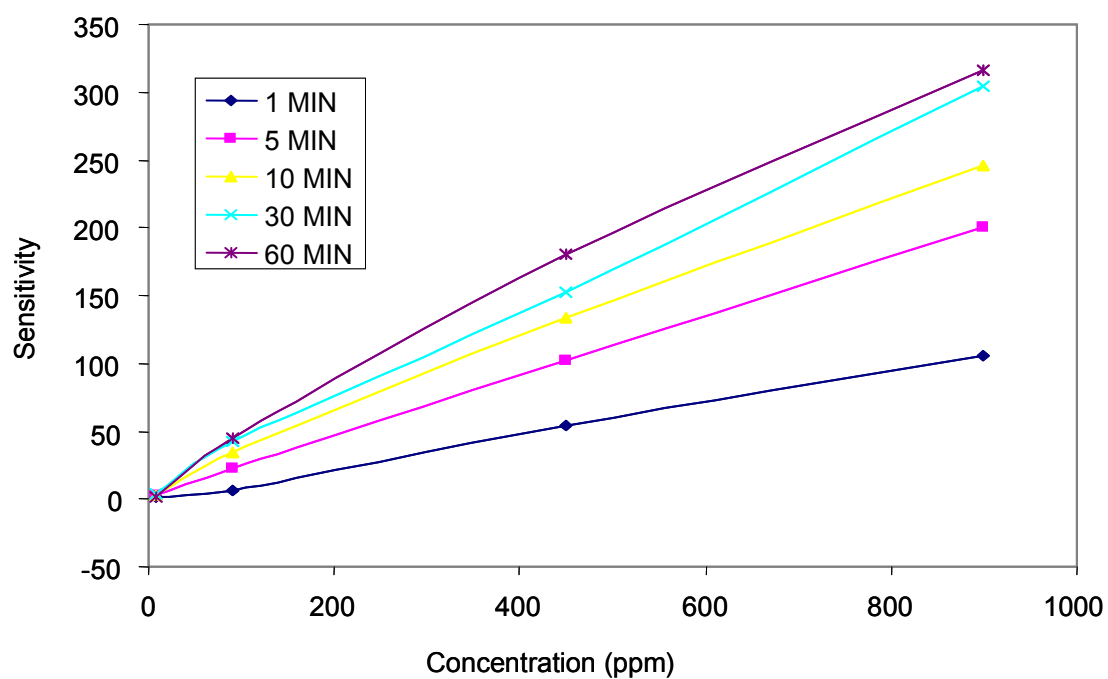


Figure 45: Calibration curve for portable instrument.

Fig 46 shows the portable hydrogen detection instrument with a hydrogen micro sensor inside. The values of resistance of the sensor at typical concentrations (400 ppm and 900 ppm) were “written” into a micro control unit (MCU) in the instrument. The MCU generated and stored a “data base” of resistance versus concentration linearly based on the recorded resistance values. MCU could transform the signal (resistances) obtained from the sensor to a signal of the concentration by comparing the collected resistances from the sensor with the data base. Converted signals were sent to the piezo buzzer for alarm signals and the liquid crystal display (LCD) circuitry shows the concentration level from 0.01 up to 0.99, in which the numerical value of 1.00 corresponds to LFL (lower flammable limit) of hydrogen gas. The whole instrument consisted of a microsensor, a MCU (ATmega48V), a LCD, a piezo buzzer, a positive voltage regulator (SPX3819) and a step-up DC/DC converter (HT7737). Testing of the instrument was carried out at room temperature without inclusion of any heating element for sensor activation. After 1 minute initialization, the instrument was ready for hydrogen detection. Upon exposure to hydrogen gas blown over the instrument, it generated a warning alarm signal and displayed concentration level immediately, due to the fast resistance drop of the sensor inside.

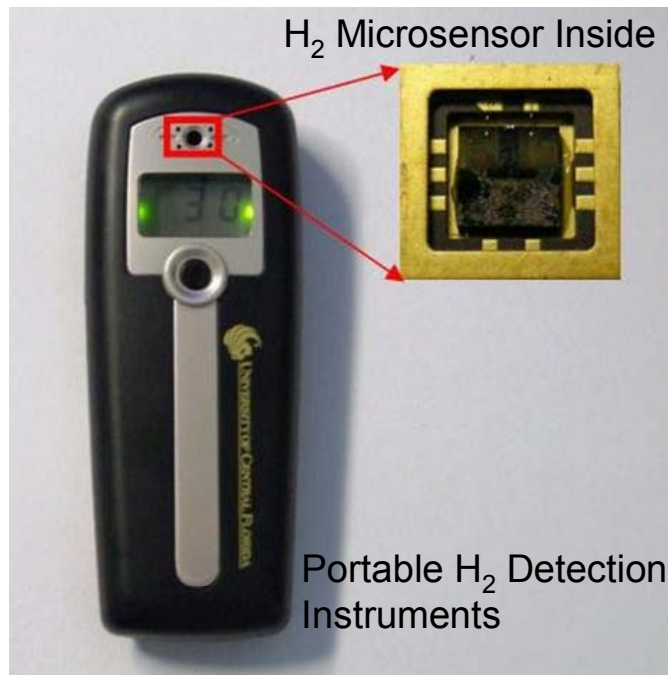


Figure 46: Portable H<sub>2</sub> detecting instrument with a H<sub>2</sub> microsensor inside.

## CHAPTER 4 NANO—GAP HYDROGEN SENSORS

In the real application of a hydrogen sensor, early warning is one of the most important requirements when there is a gas leak. Therefore fast response is a critical characteristic for any practical implementation of a hydrogen sensor. From the results of the hydrogen micro sensors, a trend was observed in which a smaller gap leads to a faster response. IDEs with various gap sizes in nanometer scale were designed and fabricated to inspect the response to hydrogen.

### 4.1 Fabrication of nano-gap sensors

The fabrication steps, as showed in Fig. 47, are similar to those of the micro sensors. A 3” single-polished Si wafer was used as the substrate. A 500 nm SiO<sub>2</sub> layer was thermally grown on the Si wafer as an insulation layer. The micro-scale Au/Cr contact pads were fabricated by UV-lithography and chemical etching. The Au/Cr contact pads were for wire-bonding and the total thickness was 220 nm. To generate nano-gap IDEs, PMMA (495 PMMA A6, MicroChem Corp.) resist was used for e-beam lithography. PMMA was spin-coated on the wafer at 4000 RPM for 45 seconds to reach the thickness of 300 nm. The wafer was baked at 170 °C on a hotplate for 10 minutes and then cooled down to the room temperature. The e-beam writing was carried out by Leica EBPG5000+ Electron Beam Lithography System with a dose of 550  $\mu\text{C}/\text{cm}^2$  and beam size of 1 nA. The sample was developed in 1:3 MIBK (methyl isobutyl ketone): IPA (isopropyl alcohol) for 30 seconds, rinsed in IPA for 1 minute, and then dried by N<sub>2</sub>. 4 nm Cr and 50 nm Au layers were

deposited on the wafer in sequence for the electrode materials by thermal evaporation. Patterns of electrodes were transferred to the Au/Cr layer by lift-off process in which PMMA was removed by acetone. The wafer with nano-gap IDEs was diced and ready for the sensing material integration. Figure 48 shows the SEM (scanning electron microscopy) images of PMMA patterns and Au/Cr IDEs with nano-gaps. 120-nm thick In-doped SnO<sub>2</sub> sensing film was deposited on the IDEs using the same process used in the micro sensor fabrication. Pt sputtering was carried out for 7 seconds, instead of 10 seconds (for the micro sensor fabrication), to avoid a continuous Pt film between the nano-gaps. The sensor was wire-bonded to a dual-line package for testing.

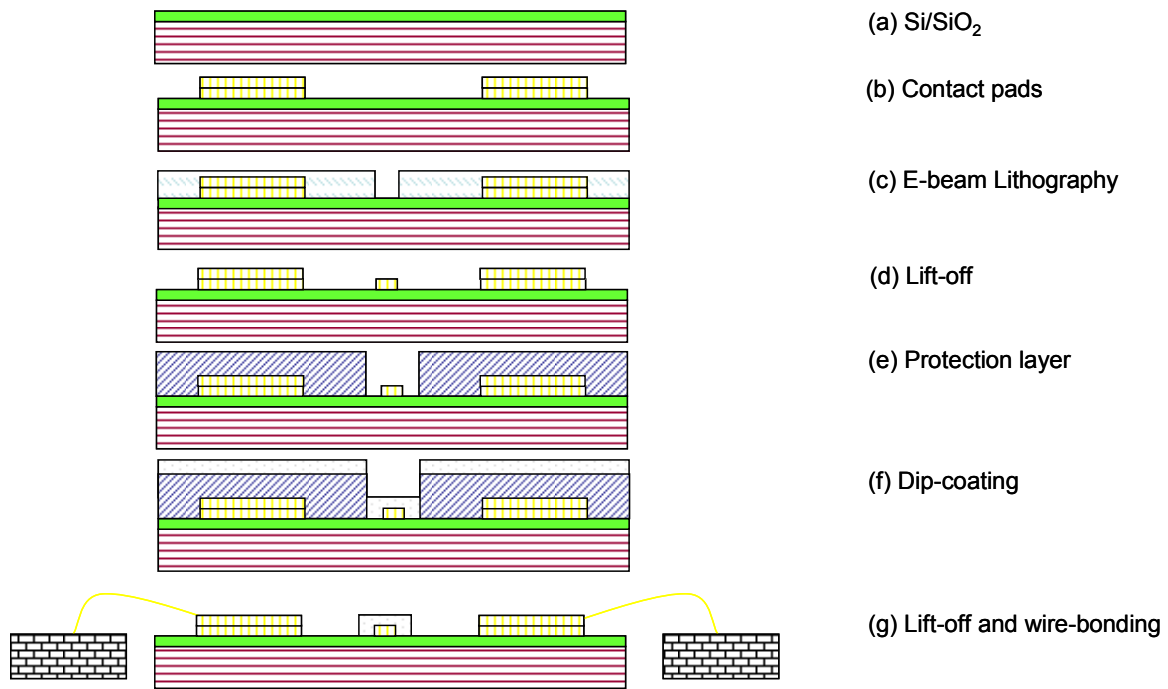


Figure 47: Fabrication steps of nano-gap sensors: (a) SiO<sub>2</sub> grown, (b) fabrication of contact pads, (c) e-beam writing, (d) Au/Cr deposition and lift-off, (e) protection layer coating, (f) In-doped SnO<sub>2</sub> coating, and (g) lift-off and wire-bonding.



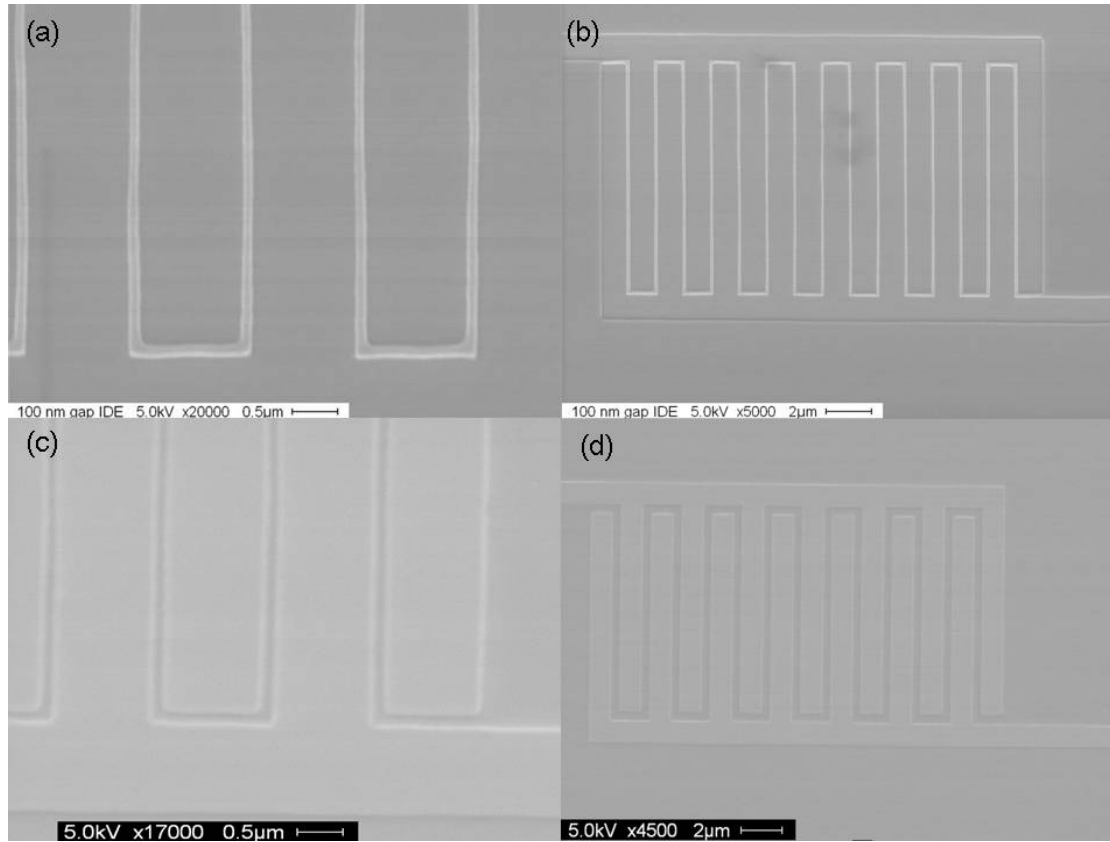


Figure 48: SEM images of PMMA patterns (a) in detail and (b) overview, and images of Au/Cr electrodes (c) in detail and (d) overview.

## 4.2 Testing of the sensor response

### 4.2.1 Sensitivity, repeatability and response time

The testing condition are the same as that for the micro-gap sensor testing. Figure 49 shows the testing result of a 200-nm gap sensor. Upon admission of the hydrogen into the chamber, the resistance of the sensor dropped from an initial value of 74 M $\Omega$ , to 6.7M $\Omega$  in 35 seconds. The resistance change rate is as large as 1.92 M $\Omega$ /second. This result clearly shows room temperature hydrogen detection with fast response as expected. After attaining a steady state condition, the chamber pressure was restored to 760 Torr. The sensor signal was recovered after measurement as shown in the graph (Fig. 49).

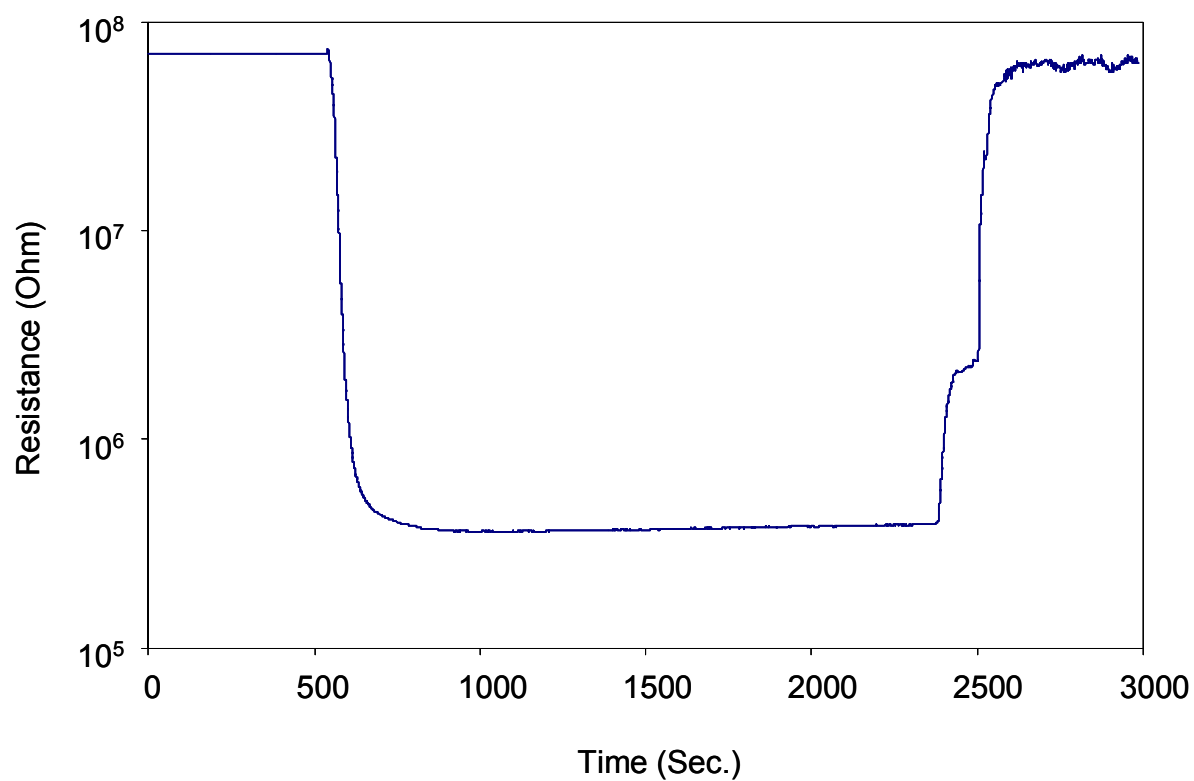


Figure 49: Resistance variation of the 200-nm gap hydrogen sensor in response to 900 ppm hydrogen at room temperature.

Figure 50 shows the gap effects on the nano-gap sensors. As expected, the sensitivity increased, with the gap size exhibiting the same trend found in the micro-gap sensors (See Fig. 37).

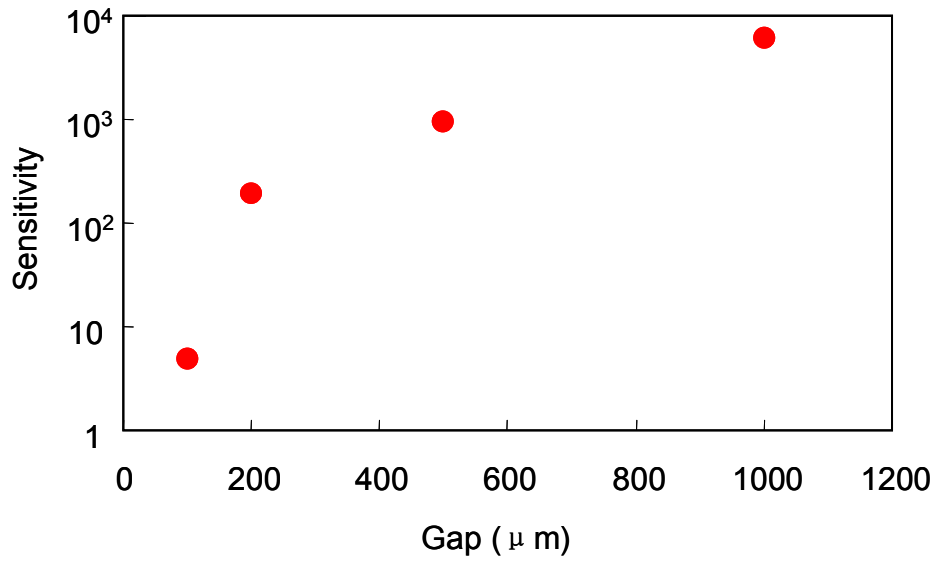


Figure 50: Effect of gap size on the sensitivity of the nano-gap sensors.

The repeatability has been tested to confirm the sensor performance under dynamic operating conditions as shown in Fig. 51. The device showed recovery at each run, which proved the repeatability of the nano-gap sensors.

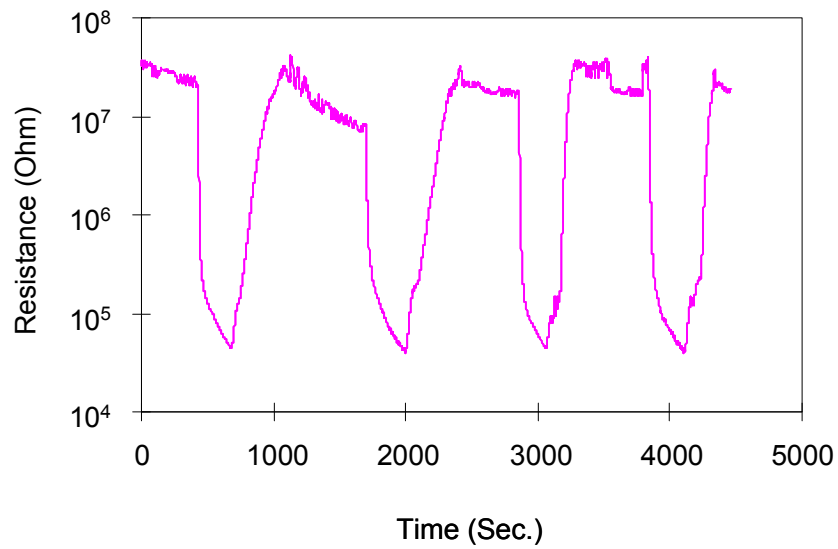


Figure 51: Multi-circle testing to test the repeatability of the nano-gap sensors in 900 ppm H<sub>2</sub> at room temperature.

The fastest response of 35 seconds was observed from the 200 nm gap sensor. It is related to the high electric field, which assists Pt to dissociate the hydrogen as explained in Section 2.3.1. It is postulated that a larger population of electrons transferred to conduction band in a short time interval, thus contributing to the quickly reduced resistance.

#### 4.2.2 Effect of the applied voltage

The testing of the sensor response under various applied voltages was carried out on the nm-gap sensors. Significant changes in the sensor response were observed on the 100-nm gap sensor as shown in Fig. 52.

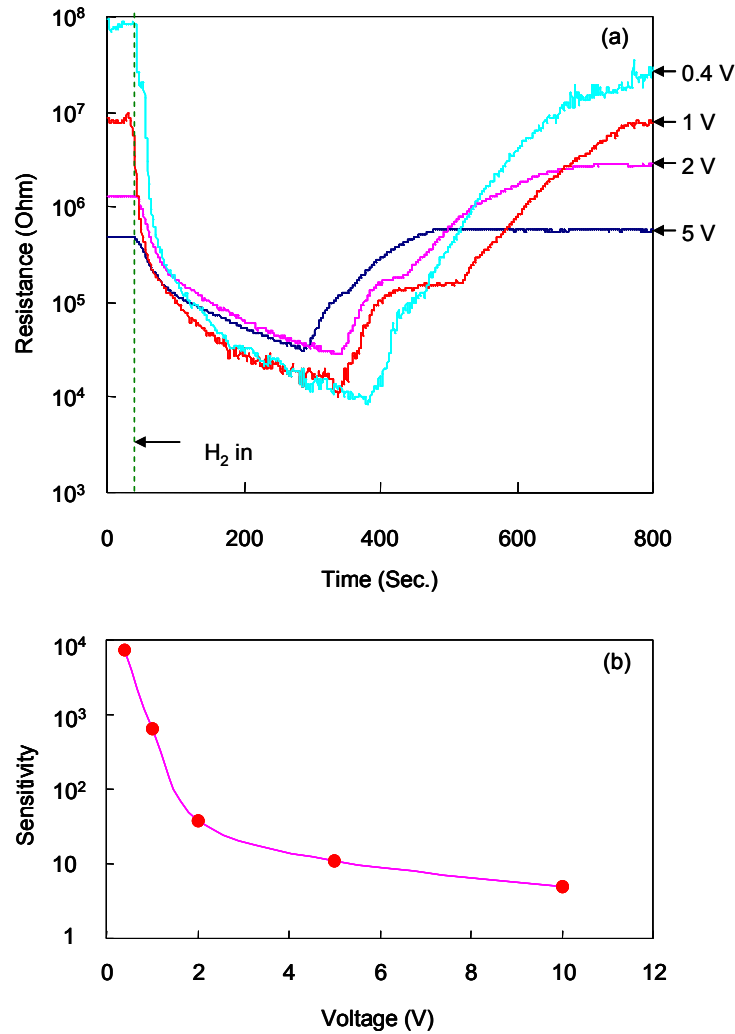


Figure 52: Effect of applied voltage on the sensor performance (a) resistance change and (b) sensitivity change with applied voltages.

Figure 52 (a) shows the resistance changes with various applied voltages. The response of the sensor varied with the applied voltages. The sensor exhibited the highest initial resistance at the lowest applied voltage (0.4 volt) and decreased with the increasing applied voltage. The calculated sensitivities were shown in Fig. 52 (b). The sensitivity dropped with the applied voltages from 7224 at 0.4 volt to 5 at 10 volts. Similar phenomena was observed on 200-nm gap sensor as shown in Fig 53, though the sensitivity drop of the 200 nm-gap

sensor is not as much as that of the 100-nm gap sensor. For the 500-nm gap and 1000-nm gap sensors, the trend in which the resistance (sensitivity) varies with the change in applied voltages is not obvious, as showed in Fig 54. When the applied voltage changed from 10 volts to 0.4 volt, the resistance of the 100 nm-gap sensor increased sharply, while that of the 500-nm and 1000-nm gap sensors did not change much. The resistances recovered when the applied voltage changed back to 10 volts. In repeated runs, all of the sensors were working in the same way, and the trend was repeatable.

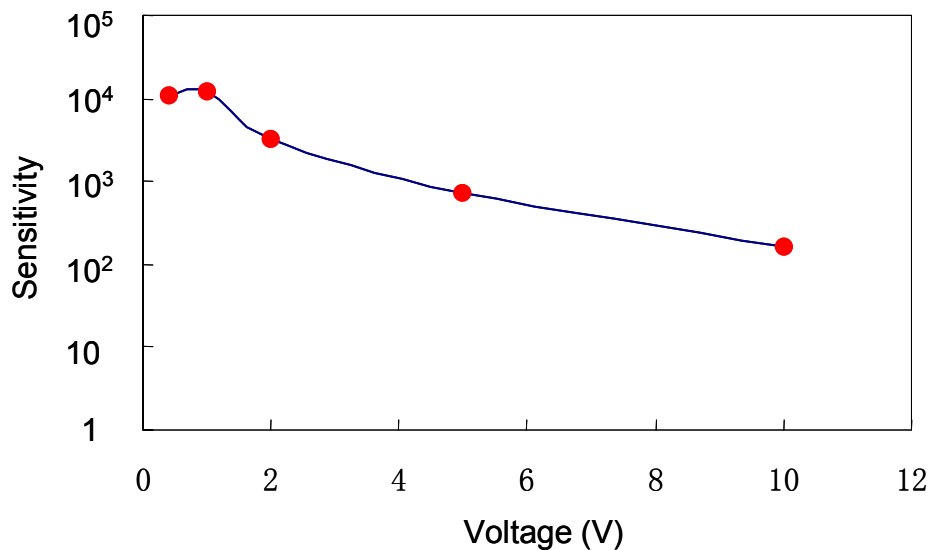


Figure 53: Sensitivity change with applied voltages on a 200 nm-gap sensor.

A focus was placed on the 100-nm gap sensor. Table 2 lists the initial resistances and currents, saturated resistances and currents in H<sub>2</sub> and response time of the 100-nm gap sensor at various applied voltages.

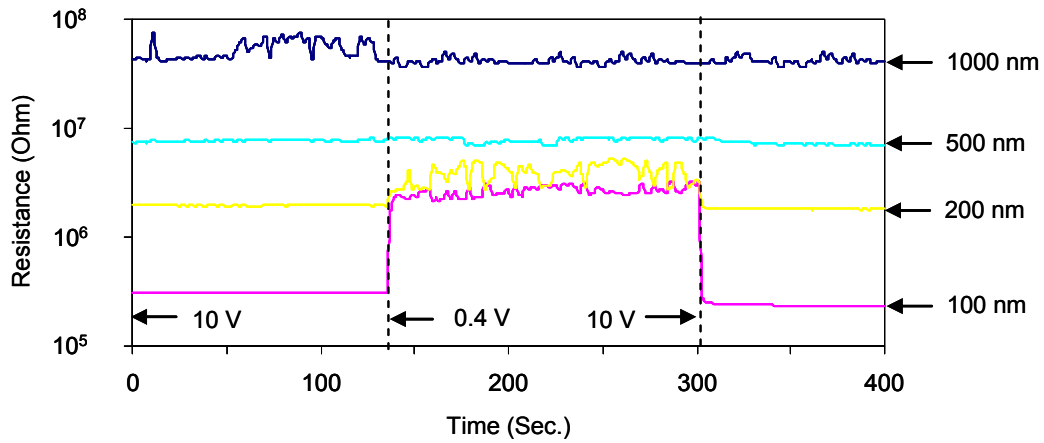


Figure 54: Changes of Initial resistance of nano-gap sensors with applied voltages.

Table 2 Sensitivity and response time of 100-nm gap sensors

Applied voltage (volt)	0.4	1	2	5	10
Initial resistance (M $\Omega$ )	83	11	1.3	0.47	0.21
Initial current (nA)	5	91	1561	10486	48161
Saturated resistance (K $\Omega$ )	12	19	34	42	42
Saturated current ( $\mu$ A)	33	50	59	119	238
Response time (Sec.)	7	15	88	217	1048

Based on the data listed in Table 2, I/V curves of the sensor before being exposed to H<sub>2</sub> and in H<sub>2</sub> are shown in Fig 55. In Fig. 55 (a), initial current (I) was as small as 5 nA at 0.4 volt, and increased exponentially. At higher voltages, the current increased linearly. This I/V curve is similar to that of a Schottky diode followed by a pure resistor. This is reasonable because of the presence of Schottky contacts at the electrode/material interfaces due to the different work functions [128-132]. At the low applied voltage, current (I) was controlled by

the Schottky barriers at the electrode/material interfaces. With the increase of the applied voltage,  $I$  increased, but was constrained by the resistance of the sensing material showing the linear trend. In Fig. 55 (b),  $I$  increased linearly with the applied voltages, which implies the Schottky barriers are weakened with the present of  $H_2$  [72, 74]. To explain this phenomenon, a new conduction model is proposed as shown in Fig 56.

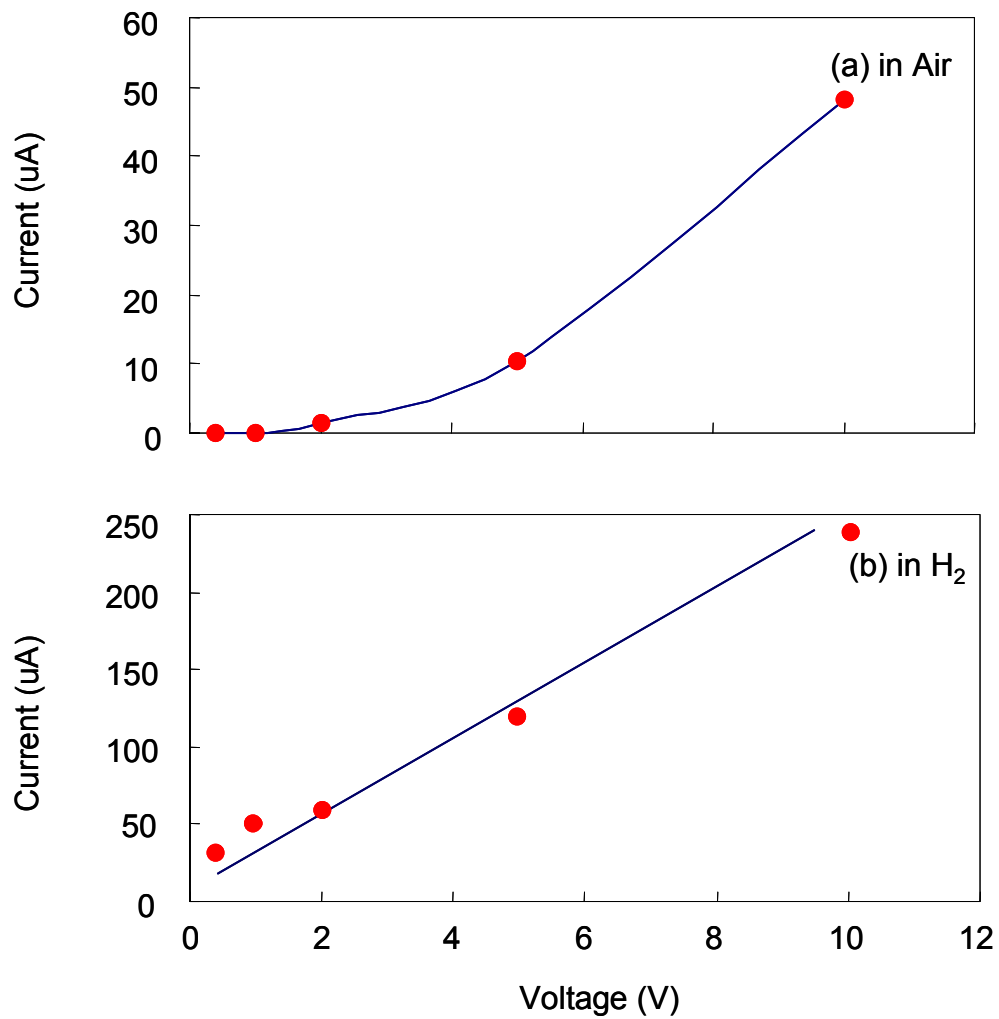


Figure 55: I/V curves of the 100-nm gap sensor (a) before exposed to  $H_2$  (in Air) and (b) in  $H_2$ .



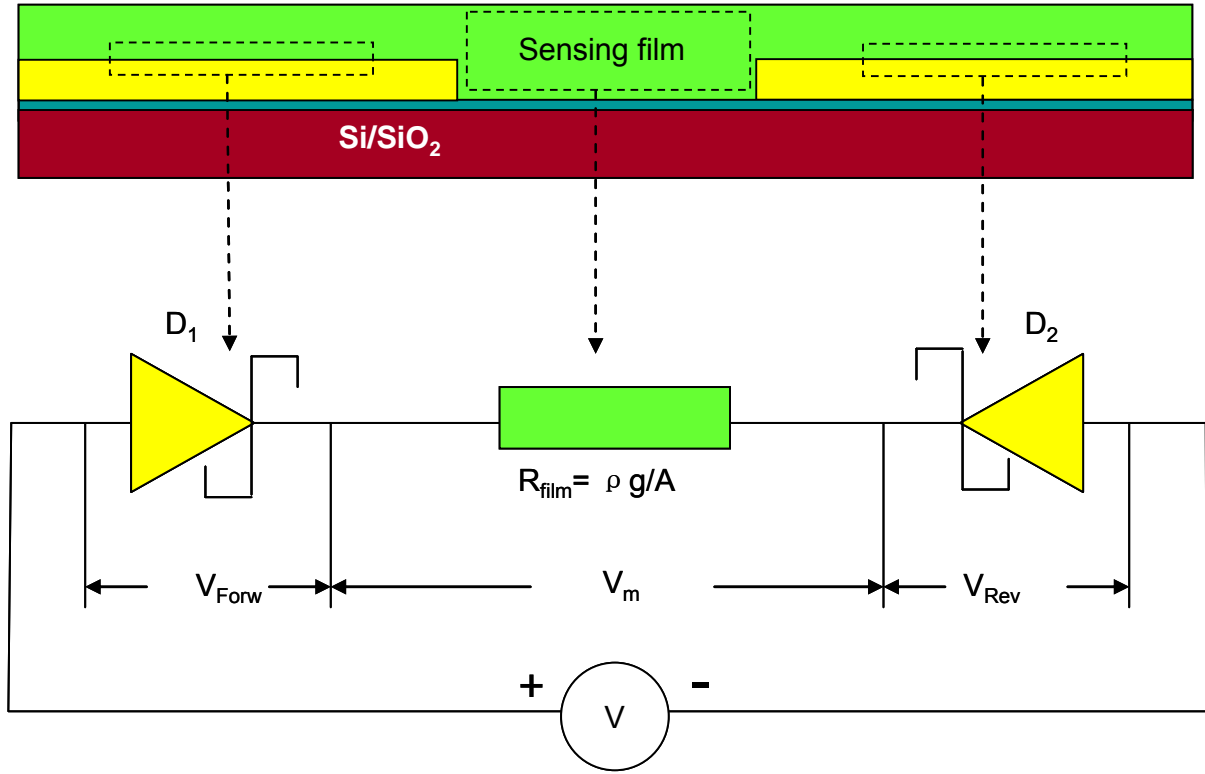


Figure 56: A proposed model based on the Schottky diode assumption. The electrode/material interfaces are considered as Schottky diodes and the sensing film (In-doped SnO<sub>2</sub>) is considered as a uniform varistor.  $V_{\text{Forw}}$ ,  $V_m$  and  $V_{\text{Rev}}$  are the potential drop over the left Schottky diode (D<sub>1</sub>), the sensing material and the right Schottky diode (D<sub>2</sub>), respectively.  $V$  is the applied voltage.  $R_b$  is the bulk resistance of In-doped SnO<sub>2</sub>.  $\rho$  is the resistivity of In-doped SnO<sub>2</sub>.  $g$  and  $A$  are the gap and area of the cross-section, respectively.

In this model, the contacts at the electrode/material interfaces are considered Schottky diodes, and the device is considered to be two Schottky diodes (D<sub>1</sub> and D<sub>2</sub>) connected back-to-back with a series resistance from In-doped SnO<sub>2</sub> in between. When the voltage ( $V$ ) is applied, D<sub>1</sub> is forward biased and the potential drop,  $V_{\text{Forw}}$ , is assumed to be small. D<sub>2</sub> is reverse biased, and  $V_{\text{Rev}}$  is determined by  $R_b$ . The governing equations of this model are:

$$V = V_{Forw} + V_m + V_{Rev} \quad (4.1)$$

$$I = I_{Forw} = I_m = I_{Rev} \quad (4.2)$$

$$V_m = \rho \frac{g}{A} I_m \quad (4.3)$$

$$I = \frac{V}{R} \quad (4.4)$$

Assume  $V_b$  is the breakdown voltage of the Schottky diode, The current  $I_{Rev}$  of  $D_2$  could be expressed as:

$$I_{Rev} = K_1 \exp[K_2 (V_{Rev} - V_b)] \quad \text{when } V_{Rev} > V_b \quad (4.5)$$

$$I_{Rev} = K_3 \quad \text{when } V_{Rev} < V_b \quad (4.6)$$

where  $I$  and  $R$  are the total resistance and current, respectively.  $I_{Forw}$ ,  $I_m$  and  $I_{Rev}$  are the current that flow through  $D_1$ , sensing material and  $D_2$ , respectively.  $K_1$ ,  $K_2$  and  $K_3$  are constant.  $K_3$  is assumed to be very small.

Case (I): If the applied voltage is small, such as 0.4 volt, and  $V_{Rev} < V_b$  (breakdown does not happen in  $D_2$ ), current ( $I$ ) is constrained to be a very small value ( $K_3$ ), and the initial resistance ( $R_a$ ) could be very large regardless the resistance of  $R_b$ :

$$R_a = \frac{V}{K_3} \quad (4.7)$$

When  $H_2$  is introduced, the resistance of the sensing film reduces dramatically. The breakdown of  $D_2$  can happen.  $I_{Rev}$  increases dramatically with  $V_{Rev}$ .  $V_m$  also becomes larger due to the existence of  $R_b$  and the sharp increase of  $I$  or  $I_{Rev}$ . The increase in  $V_m$  constrains the  $V_{Rev}$  or  $I_{Rev}$  to satisfy the governing Equation 4.1 and 4.2. In this case, the current is controlled by both sensing material resistance ( $R_b$ ) and  $V_{Rev}$ . To simplify the analysis, the forward bias voltage ( $V_{Forw}$ ) over  $D_1$  is ignored and  $I_{rev}$  is rewritten as:

$$I_{Rev} = K(V_{Rev} - V_b) \quad (4.8)$$

where  $K$  is a constant and assumed to be large.

Equation 4.2 becomes:

$$I = \frac{V - V_{Rev}}{\rho \frac{g}{A}} = K(V_{Rev} - V_b) \quad (4.9)$$

By solving Equation 4.9,  $V_{Rev}$  and  $I$  are expressed as:

$$V_{Rev} = \frac{V - V_b}{1 + K\rho\left(\frac{g}{A}\right)} + V_b \quad (4.10)$$

$$I = \frac{K}{1 + K\rho_g \left( \frac{g}{A} \right)} (V - V_b) \quad (4.11)$$

The minimum resistance ( $R_g$ ) in  $H_2$  and sensitivity ( $S_1$ ) are calculated as:

$$R_g = \frac{V}{I_g} = \frac{V}{\frac{K}{1 + K\rho_g \left( \frac{g}{A} \right)} (V - V_{b-g})} = \frac{1 + K\rho_g \left( \frac{g}{A} \right)}{K} \cdot \frac{V}{V - V_{b-g}} \quad (4.12)$$

$$S_1 = \frac{R_a}{R_g} = \frac{V/K_3}{\frac{1 + K\rho_g \left( \frac{g}{A} \right)}{K} \cdot \frac{V}{V - V_{b-g}}} = \frac{K}{K_3} \cdot \frac{V - V_{b-g}}{1 + K\rho_g \left( \frac{g}{A} \right)} \quad (4.13)$$

where  $\rho_g$  is the resistivity of the sensing material in  $H_2$  and  $V_{b-g}$  is the breakdown voltage of  $D_2$  in  $H_2$ .

Due to the very small  $K_3$  (such as 5 nA at 0.4 volt in the case of the 100-nm gap sensor), the sensitivity would be huge at low voltage.

Case (II): If  $V$  is large enough to make  $V_{Rev}$  larger than  $V_b$  in air, both the current ( $I_a$ ) and current in  $H_2$  ( $I_g$ ) are governed by Equation 4.9 due to the breakdown of  $D_2$ , and the sensitivity is calculated as:

$$\begin{aligned}
S_2 &= \frac{R_a}{R_g} = \frac{I_g}{I_a} = \frac{\frac{K}{1 + K\rho_g \left(\frac{g}{A}\right)} (V - V_{b-g})}{\frac{K}{1 + K\rho_a \left(\frac{g}{A}\right)} (V - V_{b-a})} = \frac{1 + K\rho_a \left(\frac{g}{A}\right)}{1 + K\rho_g \left(\frac{g}{A}\right)} \cdot \frac{V - V_{b-g}}{V - V_{b-a}} \\
&= \frac{\rho_a}{\rho_g} \left( 1 - \frac{\rho_a - \rho_g}{\rho_a + K\rho_a \rho_g \frac{g}{A}} \right) \left( 1 + \frac{V_{b-a} - V_{b-g}}{V - V_{b-a}} \right)
\end{aligned} \tag{4.14}$$

where  $\rho_a$  and  $\rho_g$  are the resistivity of the sensing material in air and in  $H_2$ , respectively.  $V_{b-a}$  is the breakdown voltage of  $D_2$  in air.  $V_{b-a}$  is assumed to be larger than  $V_{b-g}$  because the introduction of hydrogen can reduce the Schottky barrier at the electrode/material interface [72, 74, 156].

Equation 4.14 shows the effects of both the parameters of IDEs and the applied voltages on the sensitivity. The larger gap ( $g$ ), the larger the sensitivity and the larger applied voltage, the smaller the sensitivity.

The 100 nm-gap sensor showed a huge sensitivity of 7224 and fast response of 7 seconds with an applied voltage of 0.4 volt. At this small voltage, the breakdown did not happen in air (Case (I)) and current ( $I_a$ ) was constrained by the Schottky barriers at the electrode/material interfaces. When  $H_2$  was introduced, not only was the resistance of the sensing material reduced, but the height of Schottky barriers was also lowered [72, 74]. The total resistance drop came from both the material and device (interfaces). The extra resistance drop at the interfaces contributed to the high sensitivity and fast response. Under a high voltage, breakdown happened in air and sensitivity was controlled by the material, the geometry of the IDEs and the applied voltage. As discussed above (Case (II)), the sensitivity

decreases with the applied voltage as shown in Fig. 57. Figure 57 (a) and (b) show the relationship between the sensitivity and the applied voltages obtained by the experiments (the same as Fig. 52 (b)) and by Equation 4.14, respectively.

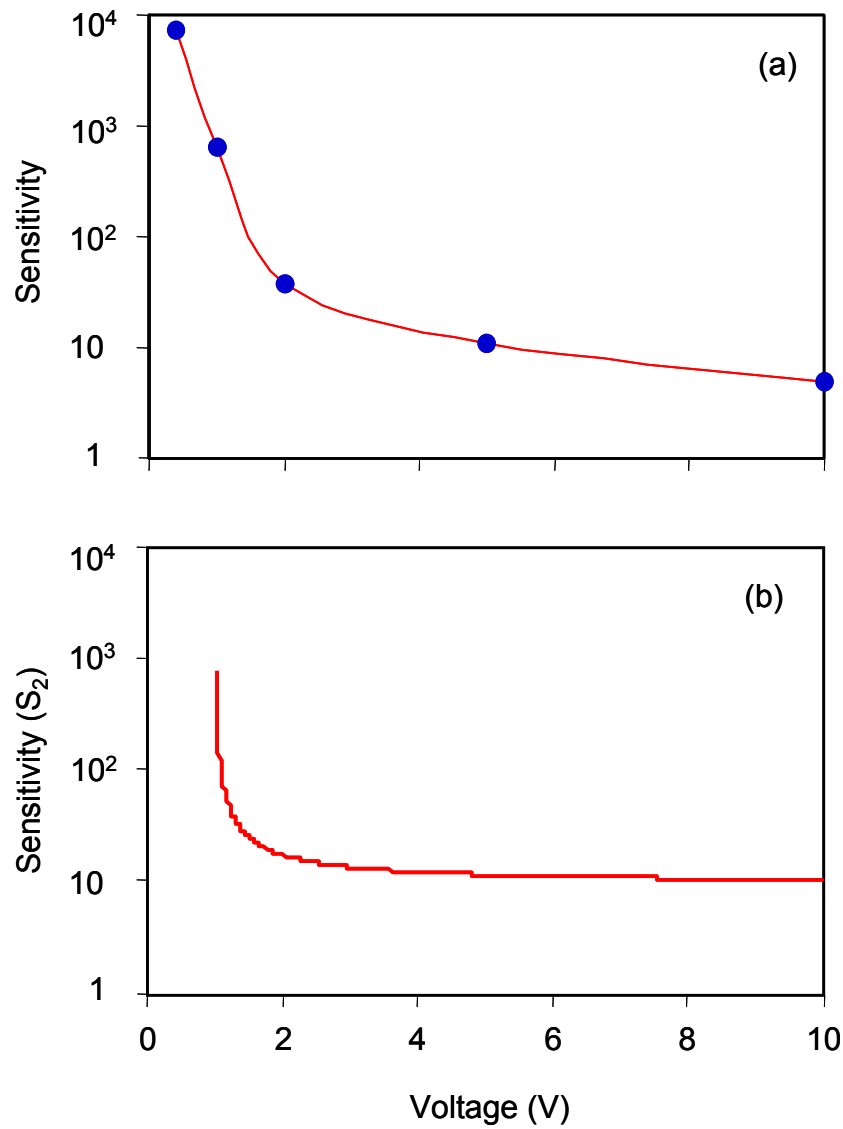


Figure 57: Sensitivity as a function of applied voltages: (a) experimental result of 100-nm gap sensor and (b) analytical prediction based on equation 4.14.

They exhibit a similar trend where the larger applied voltage, the smaller the sensitivity, which proves the model can explain the effect of the applied voltage on the response of 100 nm-gap sensor. In Fig. 57 (b), the  $V_{b-a}$  and  $V_{b-g}$  are assumed to be 1 volt and 0.2 volt, respectively.

This model can be applied to micro-gap sensors, though it was developed based on the response of the 100-nm gap sensor. For micro-gap sensors, due to the effect of humidity, the resistance ( $R_b$ ) of the sensing material might be low enough to cause breakdown to happen when the applied voltage is as large as 10 volts (Case (II)). As shown in Equation 4.14, when breakdown happens, the smaller gap ( $g$ ) is responsible for the smaller sensitivity. The comparison of test results of the micro sensors and Equation 4.14 is shown in Fig 58. In Fig. 58, the test results of the micro sensors and the numerical calculation of Equation 4.14 show a similar trend where the sensitivity is increased with the gap size. In the numerical calculation of Equation 4.14, the value of  $\rho_a/\rho_g$  is assumed to be  $10^5$ , considering the highest sensitivity obtained was 70,000 on the 20- $\mu\text{m}$  gap sensor;  $V_{\text{Forw}}$  and  $V_b$  are assumed to be 0.2 volt and 0.5 volt, respectively.  $V$  is 10 volts.

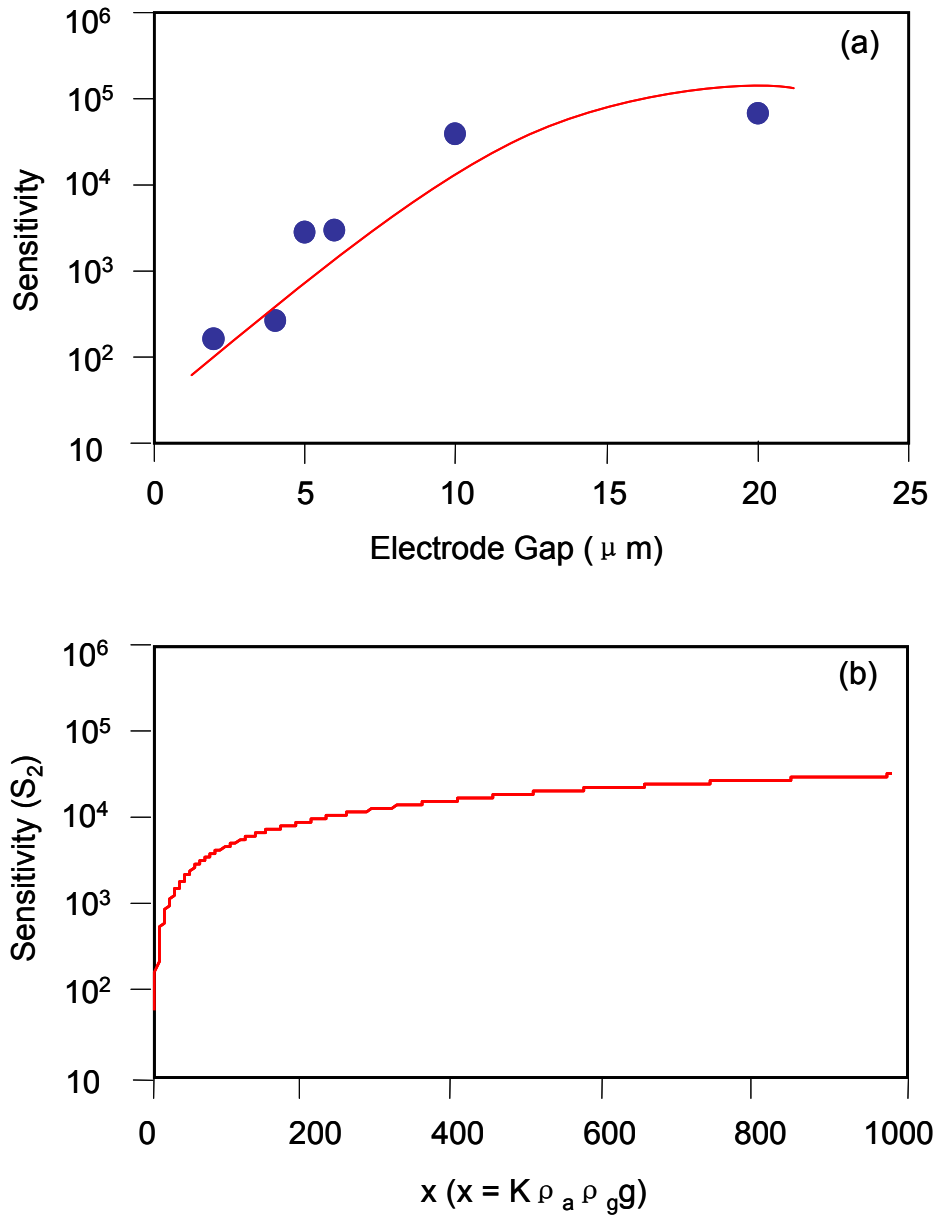


Figure 58: Sensitivity as a function of a gap parameter: (a) experimental result of micro sensors and (b) analytical prediction based on equation 4.14, where,  $x = K \rho_a \rho_g g$ , the variable  $x$  contains electrode gap ( $g$ ) and the constants  $K$  and  $\rho_g$  for given material and testing conditions.

For the sensors with a larger resistance, such as sensors with a large gap, breakdown will not happen even under the influence of humidity (Case (I)). The sensitivity might be



governed by Equation 4.13. The sensitivity will decrease with an increase of gap (g) size.

This could be another reason why the macro sensor showed low sensitivity.

## CHAPTER 5 CONCLUSION

In this work, the chemiresistor based hydrogen sensors integrating micro/nanofabricated IDEs (interdigitated electrodes) and In-doped SnO<sub>2</sub> nanoparticles were designed and tested. The analysis of the IDEs was carried out based on numerical calculations. Several design guidelines were obtained utilizing the analytical results. Sensor platforms with various electrode geometries from micro-scale to nano-scale were fabricated by MEMS techniques and e-beam lithography. In conjunction with In-doped SnO<sub>2</sub> nanoparticles, sensor characteristics were investigated under various conditions. A conduction model of the sensors was developed based on the testing results.

1. According to the potential distribution above IDEs, the intensity of electric field is considerably weakened with an increasing distance from the electrode surface. Most of the current flows through a thin layer near the IDEs surface. Therefore, a thin sensing film is preferred for fast response.

2. Response time is more dependent on chemical reaction on the sensor surface than the diffusion process for thin film hydrogen sensors. For the sensors with sensitivity larger than 100, it is predicted that resistance change of a single outermost layer exposed to hydrogen can induce a total resistance change by one order of magnitude.

3. The response time depends on the electrode gap. A smaller gap contributes to faster response. It is believed that this is due to a high electric field which assists hydrogen dissociation on Pt surface. Parameters such as the gap, finger length and width are closely related to the sensitivity. The smaller gap reduces the sensitivity by reducing the sensing area. Longer finger length enhances the sensitivity by increasing the sensing area. Wider electrode

width shows a higher sensitivity at the electrode/material interfaces and therefore contributes to higher sensitivity.

4. There is a cross-talk between moisture and hydrogen gas in hydrogen sensing. A humidity change can cause a variation of the sensor resistance and a false signal. PMMA coatings could significantly reduce the humidity effects and improve both the sensitivity and response time.

5. Micro sensors exhibited a linear response to concentration from 9 ppm to 900 ppm. The portable hydrogen detection instrument with an LCD and warning system was fabricated by implementing the micro sensors.

6. Nano sensors with 100-nm and 200-nm gap showed fast response at a tuned voltage. This confirms that fast detection hydrogen sensors could be achieved using nano-gap sensors

7. A conduction model based on Schottky diodes and a pure resistor was developed. According to this model, at a low measuring voltage, the breakdown of the Schottky diode (Schottky barrier at the electrode/material interface) does not happen. The initial current is constrained by the Schottky diode, resulting in a large resistance. When hydrogen is present, breakdown can happen and contribute to a large magnitude of resistance change, resulting in high sensitivity and short response time.

Based on the analysis and experiment, the hydrogen sensors were developed to have high sensitivity ( $10^5$ ), fast response time (10 seconds) and low energy consumption (19 nW) for room temperature hydrogen detection, which would contribute to the safe development of hydrogen energy for various applications.

## APPENDIX: PUBLICATIONS AND PRESENTATIONS

P. Zhang, A. Vincent, S. Seal, H. J. Cho, “A High Speed, Low Power Hydrogen Detector,” Proceedings of Eurosensors 2008, September 7-10, 2008, Dresden, Germany

P. Zhang, G. Londe, J. Sung, E. Johnson, M. Lee and H. J. Cho, “Microlens Fabrication Using an Etched Glass Master”, Microsystem Technologies, vol. 13, 2007, pp. 339-342

P. Zhang, S. Deshpande, P. J. Medelius, S. Seal and H. J. Cho, “Study Of Design Parameters In Hydrogen Microsensors Integrated With Metal Semiconductor Nanoparticles,” Proceedings of IMECE2007 2007 ASME International Mechanical Engineering Congress and Exposition November 11-15, 2007, Seattle, Washington USA, pp205-208

P. Zhang, S. Deshpande, S. Seal, P. J. Medelius, H. J. Cho, 2006, “Fast Detection of Hydrogen at Room Temperature Using a Nanoparticle-integrated Microsensor”, Proc. The 5th International Conference on Sensors (IEEE SENSORS 2006), Daegu, Korea, October 22-25, pp. 712-715

P. Zhang, S. Shukla, L. Ludwig, S. Seal, H. J. Cho , 2005, “A Room Temperature Hydrogen Sensor with High Sensitivity and Selectivity Using Nanocrystalline Semiconductor Particles”, Proceedings of IMECE 2005: 2005 ASME International Mechanical Engineering Congress and Exposition, Orlando, Florida, November 5-11, IMECE2005-82357, pp.1-4

P. Zhang, G. Londe, J. Sung, E. Johnson and H. J. Cho, “Microlens Fabrication Using an Etched Glass Mater”, Book of Abstract, The 6th International Workshop on High Aspect Ratio Micro Structure Technology (HARMST 2005), Gyeongju, Korea, June 10-13, 2005, pp.246-247

S. Shukla, P. Zhang, H. J. Cho, L. Ludwig and S. Seal, “Significance of electrode-spacing in hydrogen detection for tin oxide-based MEMS sensor,” International Journal of Hydrogen Energy, vol. 33, 2008, pp.470 – 475

S. Deshpande, P. Zhang, H. J. Cho, N. Posey and S. Seal, “Electrode architecture in tuning room temperature sensing kinetics of nano-micro integrated hydrogen sensor,” Appl. Phys. Lett., vol.90, 2007, pp. 073118

M. Pepper, N. S. Palsandram, P. Zhang, M. Lee and H. J. Cho, “Interconnecting Fluidic Packages and Interfaces for Micromachined Sensors”, Sensors and Actuators A, vol. 134, 2007, pp. 278-285

S. Shukla, P. Zhang, H. J. Cho, S. Seal and L. Ludwig, “Room Temperature Hydrogen Response Kinetics of Nano–micro-integrated doped Tin Oxide Sensor”, Sensors and Actuators B, vol. 120, 2007, pp. 573-583,

S. Shukla, P. Zhang, H. J. Cho, Z. Rahman, C. Drake, S. Seal, V. Craciun, and L. Ludwig, “Hydrogen-discriminating nanocrystalline doped-tin-oxide room-temperature microsensor”, J. Appl. Phys., vol. 98, 2005, pp. 104306-104315

## REFERENCES

- [1] <http://www.eia.doe.gov/environment.html>
- [2] [http://www.hydrogen.gov/whyhydrogen\\_environment.html](http://www.hydrogen.gov/whyhydrogen_environment.html)
- [3] I. MacIntyre, A.V. Tchouvelev, D.R. Hay, J. Wong, J. Grant, and P. Benard, "Canadian hydrogen safety program," *International Journal of Hydrogen Energy*, Vol. 32, 2007, pp. 2134-2143
- [4] S. Shukla, S. Patil, S. C. Kuiry, Z. Rahman, T. Du, L. Ludwig, C. Parish and S. Seal, "Synthesis and characterization of sol-gel derived nanocrystalline tin oxide thin film as hydrogen sensor," *Sensors and Actuators B*, vol. 96, 2003, pp. 343-353
- [5] J. Kim, S. D. Han, C. H. Han, J. Gwak, D. U. Hong, D. Jakhar, K.C. Singh and J. S. Wang, "Development of micro hydrogen gas sensor with  $\text{SnO}_2\text{-Ag}_2\text{O-PtO}_x$  composite using MEMS process", *Sensors and Actuators B*, vol. 127, 2007, pp. 441-446
- [6] S. Deshpande, P. Zhang, H. J. Cho, N. Posey and S. Seal, "Electrode architecture in tuning room temperature sensing kinetics of nano-micro integrated hydrogen sensor," *Appl. Phys. Lett.*, vol.90, 2007, pp. 073118.
- [7] A. S. Ryzhikov, A. N. Shatokhin, F. N. Putilin, M. N. Rumyantseva, A. M. Gaskov, M. Labeau, "Hydrogen sensitivity of  $\text{SnO}_2$  thin films doped with Pt by laser ablation," *Sensors and Actuators B*, vol. 107, 2005, pp. 387-391
- [8] J. E. Dominguez, L. Fu, and X. Q. Pan, "Electrical properties of doped tin dioxide thin films deposited using femtosecond pulsed laser ablation," *Mat. Res. Soc. Symp. Proc.*, vol. 654, pp. AA.7.3.1-AA.7.3.6
- [9] B. Guo, A. Bermak, P. C. H. Chan, G. Yan, "Characterization of integrated tin oxide gas sensors with metal additives and ion implantations," *IEEE Sensors Journal*, vol. 8, 2008, pp. 1397-1698
- [10] G. De, R. Kohn, G. Xomeritakis, and C. J. Brinker, "Nanocrystalline mesoporous palladium activated tin oxide thin films as room-temperature hydrogen gas sensors," *Chem. Commun.*, 2007, 1840-1842
- [11] G. De, R. Kohn, G. Xomeritakis and C. J. Brinker, "Nanocrystalline mesoporous palladium activated tin oxide thin films as room-temperature hydrogen gas sensors," *Chem. Commun.*, 2007, pp. 1840-1842
- [12] I. P. Matushko, V. K. Yatsimirskii, N. P. Maksimovich, N. V. Nikitina, P. M. Silenko, V. P. Ruchko, and V. B. Ishchenko, "Sensitivity to hydrogen of sensor materials based on

- SnO<sub>2</sub> promoted with 3D metals,” Theoretical and Experimental Chemistry, vol. 44, 2008, pp. 128-133
- [13] B. Panchapakesan, R. Cavicchi, S. Semancik and D. L. DeVoe, “Sensitivity, selectivity and stability of tin oxide nanostructures on large area arrays of microhotplates,” Nanotechnology, vol.17, 2006, pp. 415-425
- [14] D. C. Meier, S. Semancik, B. Button, E. Strelcov, and A. Kolmakov, “Coupling nanowire chemiresistors with MEMS micro hotplate gas sensing platforms,” Applied Physics Letters, vol. 91, 2007, pp. 063118
- [15] L. L. Fields and J. P. Zheng, “Room-temperature low-power hydrogen sensor based on a single tin dioxide nanobelt,” Applied Physics Letters, vol. 88, 2006, pp. 263102.
- [16] J. Gong, J. Sun, Q. Chen, “Micromachined sol-gel carbon nanotube/SnO<sub>2</sub> nanocomposite hydrogen sensor,” Sensors and Actuators B, vol. 130, 2008, pp.829-835
- [17] M. Shafiei, W. Wlodarski, K. Kalantar-zadeh, E. Comini, S. Bianchi and G. Sberveglieri, “Pt/SnO<sub>2</sub> nanowires/SiC based hydrogen gas sensor,” Proc. The 6th International Conference on Sensors (IEEE SENSORS 2007), Atlanta, USA, October 28-31, 2007, pp. 166-169
- [18] B. Wang L. F. Zhu, Y. H. Yang, N. S. Xu, and G. W. Yang, “Fabrication of a SnO<sub>2</sub> nanowire gas sensor and sensor performance for hydrogen,” J. Phys. Chem. C, vol. 112, 2008, pp. 6643-6647
- [19] Y. T. Cheng, Y. Li, D. Lisi and W. M. Wang, “Preparation and characterization of Pd/Ni thin films for hydrogen sensing,” Sensors and Actuators B, vol. 30, 1996, pp. 11-16
- [20] D. Ding and Z. Chen, A Pyrolytic, “Carbon-stabilized, nanoporous Pd film for wide-Range H<sub>2</sub> sensing,” Adv. Mater., vol. 19, 2007, pp. 1996-1999
- [21] K. Baba, U. Miyagawa, K. Watanabe, Y. Sakamoto, “Electrical resistivity changes due to interstitial hydrogen in palladium-rich substitutional alloys,” J. Mater. Sci., vol. 25, 1990, pp. 3910-3916.
- [22] K. Yoshimura, S. Nakano, S. Uchinashi, S. Yamaura, H. Kimura and A Inoue, “A hydrogen sensor based on Mg-Pd alloy thin film,” Meas. Sci. Technol., vol. 18, 2007, pp. 3335-3338
- [23] L. Huang, H. Gong, D. K. Peng, G. Y. Meng, “Pd-Ni thin film grown on porous Al<sub>2</sub>O<sub>3</sub> substrates by metalorganic chemical vapor deposition for hydrogen sensing,” Thin Solid Films, vol. 345, 1999, pp. 217-221
- [24] R. C. Hughes and W. K. Schubert, “Thin films of Pd-Ni alloys for detection of high hydrogen concentrations,” J. Appl. Phys. vol. 71, 1992, pp. 542-548.



- [25] Y. T. Cheng, Y. Li, D. Lisi and W. M. Wang, "Preparation and characterization of Pd/Ni thin films for hydrogen sensing," *Sensors and Actuators B*, vol. 30, 1996, pp. 11-16
- [26] M. Wang and Y. Feng, "Palladium–silver thin film for hydrogen sensing," *Sensors and Actuators B*, vol. 123, 2007, pp. 101-106
- [27] X. M. H. Huang, M. Manolidis, C. J. Seong and J. Hone, "Nanomechanical hydrogen sensing," *Applied Physics Letters*, vol. 86, 2005, pp. 143104.
- [28] F. Favier, E. C. Walter, M. P. Zach, T. Benter and R. M. Penner, "Hydrogen sensors and switches from electrodeposited palladium mesowire arrays," *Science*, vol. 293, 2001, pp. 2227-2231
- [29] J. V. Lith, A. Lassesson, S. A. Brown, M. Schulze, J. G. Partridge and A. Ayes, "A hydrogen sensor based on tunneling between palladium clusters," *Applied Physics Letters*, vol. 91, 2007, pp. 181910
- [30] K. T. Kim, S. J. Sim, and S. M. Cho, "Hydrogen Gas Sensor Using Pd Nanowires Electro-Deposited Into Anodized Alumina Template," *IEEE Sensors Journal*, vol. 6, 2006, pp. 509-513
- [31] S. Iijima, "Helical microtubules of graphitic carbon," *Nature*, vol. 354, 1991, pp. 56-58.
- [32] D. R. Kauffman and A. Star, "Carbon nanotube gas and vapor sensors," *Angew. Chem. Int. Ed.*, vol. 47, 2008, pp. 6550-6570
- [33] Y. Sun and H. H. Wang, "Electrodeposition of Pd nanoparticles on single-walled carbon nanotubes for flexible hydrogen sensors," *Applied Physics Letters*, vol. 90, 2007, pp. 213107
- [34] M. K. Kumar and S. Ramaprabhu, "Nanostructured Pt functionalized multiwalled carbon nanotube based hydrogen sensor," *J. Phys. Chem. B*, vol. 110, 2006, pp. 11291-11298.
- [35] D. Ding, Z. Chen, S. Rajaputra and V. Singh, "Hydrogen sensors based on aligned carbon nanotubes in an anodic aluminum oxide template with palladium as a top electrode," *Sensors and Actuators B*, vol. 124, 2007, pp. 12-17.
- [36] J. Suehiro, S. Yamane, and K. Imasaka, "Carbon nanotube-based hydrogen gas sensor electrochemically functionalized with palladium," *Proceedings of IEEE SENSORS 2007 Conference*, Atlanta, Georgia, USA, pp. 554-557
- [37] U. Schlecht, K. Balasubramanian, M. Burghard, and K. Kern, "Electrochemically decorated carbon nanotubes for hydrogen sensing," *Applied Surface Science*, vol. 253, 2007, pp. 8394-8397
- [38] M. K. Kumar, A. L. M. Reddy, and S. Ramaprabhu, "Exfoliated single-walled carbon nanotube-based hydrogen sensor," *Sensors and Actuators B*, vol. 130, 2008, pp. 653-660

- [39] S. Mubeen, T. Zhang, B. Yoo, M. A. Deshusses and N. V. Myung, "Palladium nanoparticles decorated single-walled carbon nanotube hydrogen sensor," *J. Phys. Chem. C*, vol. 111, 2007, pp. 6321-6327.
- [40] Y. Sun and H. H. Wang, "High-performance, flexible hydrogen sensors that use carbon nanotubes decorated with palladium nanoparticles," *Adv. Mater.*, vol. 19, 2007, pp. 2818-282
- [41] M. Krishna Kumar, S. Ramaprabhu, "Palladium dispersed multiwalled carbon nanotube based hydrogen sensor for fuel cell applications," *International Journal of Hydrogen Energy*, vol. 32, 2007, pp. 2518-2526
- [42] A. Z. Sadek, S. Choopun, W. Wlodarski, S. J. Ippolito, and K. Kalantar-zadeh, "Characterization of ZnO nanobelt-based gas sensor for H<sub>2</sub>, NO<sub>2</sub>, and hydrocarbon sensing," *IEEE Sensors Journal*, vol. 7, 2007, pp. 919-924
- [43] L. Bie, X. Yan, J. Yin, Y. Duan, and Z. Yuan, "Nanopillar ZnO gas sensor for hydrogen and ethanol," *Sensors and Actuators B*, vol.126, 2007, pp. 604-608
- [44] J. Jun, B. Chou, J. Lin, A. Phipps, X. Shengwen, K. Ngo, D. Johnson, A. Kasyap, T. Nishida, H. T. Wang, B. S. Kang, F. Ren, L. C. Tien, P. W. Sadik, D. P. Norton, L. F. Voss and S. J. Pearton, "A hydrogen leakage detection system using self-powered wireless hydrogen sensor nodes," *Solid-State Electronics*, vol. 51, 2007, pp. 1018-1022
- [45] O. Lupana, G. Chaic and L. Chow, "Fabrication of ZnO nanorod-based hydrogen gas nanosensor," *Microelectronics Journal*, vol. 38, 2007, pp. 1211-1216
- [46] C. S. Rout, A. R. Raju, A. Govindaraj and C. N. R. Rao, "Hydrogen sensors based on ZnO nanoparticles," *Solid State Communications*, vol. 138, 2006, pp.136-138
- [47] G. K. Mor, M. A. Carvalho, O. K. Varghese, M. V. Pishko and C. A. Grimes, "A room-temperature TiO<sub>2</sub>-nanotube hydrogen sensor able to self-clean photoactively from environmental contamination", *Journal of Materials Research*, vol. 19, 2007, pp. 628-634.
- [48] O. K. Varghese, G. K. Mor, M. Paulose, and C. A. Grimes, "A Titania Nanotube-Array Room-Temperature Sensor for Selective Detection of Low Hydrogen Concentrations," *Mater. Res. Soc. Symp. Proc.*, vol. 835, 2005, pp. K.4.1.1/A3.1.1-K4.1.9/A3.1.9
- [49] G. K. Mor, O. K. Varghese, M. Paulose, K. G. Ong, and C. A. Grimes, "Fabrication of hydrogen sensors with transparent titanium oxide nanotube-array thin films as sensing elements," *Thin Solid Films*, vol. 496, 2006, pp. 42-48
- [50] C. Hana, D. Honga, I. Kima, J. Gwak, S. Hana, K. C. Singh, "Synthesis of Pd or Pt/titanate nanotube and its application to catalytic type hydrogen gas sensor," *Sensors and Actuators B*, vol.128, 2007, pp. 320-325

- [51] O. K. V., D. Gong, M. Paulose, K. G. Ong and C. A. Grimes, "Hydrogen sensing using titania nanotubes," *Sensors and Actuators B*, vol. 93, 2003, pp. 338-344
- [52] Z. H. Chen, J. S. Jie, L. B. Luo, H. Wang, C. S. Lee and S. T. Lee, "Applications of silicon nanowires functionalized with palladium nanoparticles in hydrogen sensors," *Nanotechnology*, vol. 18, 2007, pp. 345502
- [53] P. K. Sekhar, A. Sine and S. Bhansali, "Effect of varying the nanostructured porous-Si process parameters on the performance of Pd-doped hydrogen sensor," *Sensors and Actuators B*, vol. 127, 2007, pp. 74-81
- [54] W. Lim, J. S. Wright, B. P. Gila, J. L. Johnson, A. Ural, T. Anderson, F. Ren, and S. J. Pearton, "Room temperature hydrogen detection using Pd-coated GaN nanowires," *Applied Physics Letters*, vol. 93, 2008, pp. 072109
- [55] G. N. Chaudhari, A. M. Bende, A. B. Bodade, S. S. Patil and V. S. Sapkal, "Structural and gas sensing properties of nanocrystalline TiO<sub>2</sub>:WO<sub>3</sub>-based hydrogen sensors," *Sensors and Actuators B*, vol. 115, 2006, pp. 297-302
- [56] L. Al-Mashat, H. D. Tran, W. Wlodarski, R. B. Kaner, and K. Kalantar-Zadeh, "Conductometric hydrogen gas sensor based on polypyrrole nanofibers," *IEEE Sensors Journal*, vol. 8, 2008, pp. 365-370
- [57] A. Z. Sadek, W. Wlodarski, K. Kalantar-Zadeh, C. Baker and R.B. Kaner, "Doped and dedoped polyaniline nanofiber based conductometric hydrogen gas sensors," *Sensors and Actuators A*, vol.139, 2007, pp. 53-57
- [58] K. Hirao Y. Tsukada, S. Suzuk, H. Takahashi, and J. Mizuguchi, "Anomalous phenomenon in hydrogen gas sensors based upon pyridylimidazopyrylene or pyridylimidazonaphthalene," *Journal of Applied Physics*, vol.103, 2008, pp. 053706
- [59] C. Cheng, Y. Tsai, K. Lin, H. Chen, C. Lu, W. Liu, "Hydrogen sensing characteristics of a Pt-oxide-Al<sub>0.3</sub>Ga<sub>0.7</sub>As MOS Schottky diode," *Sensors and Actuators B*, vol. 99, 2004, pp. 425-430
- [60] Y. Tsai, K. Lin, H. Chen, I. Liu, C. Hung, T. Chen, T. Tsai, L. Chen, K. Chu, and W. Liu, "Hydrogen sensing properties of a Pt-oxide-GaN Schottky diode," *Journal of Applied Physics*, vol. 104, 2008, pp. 024515
- [61] S. Roy, C. Jacob, S. Basu, "Studies on Pd/3C-SiC Schottky junction hydrogen sensors at high temperature," *Sensors and Actuators B*, vol. 94, 2003, pp. 298-303
- [62] H. Chen, Y. Chou, and C. Chu, "A novel high-sensitive Pd/InP hydrogen sensor fabricated by electroless plating," *Sensors and Actuators B*, vol. 85, 2002, pp. 10-18
- [63] Y. Chou, C. Chen, W. Liu, and H. Chen, "A new Pd-InP Schottky hydrogen sensor

- fabricated by electrophoretic deposition with Pd nanoparticles,” IEEE Electron Device Letters, vol. 26, 2005, pp. 526-529
- [64] C. K. Kim J. H. Lee, Y. H. Lee, N. I. Cho, and D. J. Kim, “A study on a platinum–silicon carbide Schottky diode as a hydrogen gas sensor,” Sensors and Actuators B, vol. 66, 2000, pp. 116-118
- [65] Y. Y. Tsai, H. I. Chen, C. W. Hung, T. P. Chen, T. H. Tsai, K. Y. Chu, L.Y. Chen, and W. C. Liu, “A hydrogen gas sensitive Pt–In<sub>0.5</sub>Al<sub>0.5</sub>P metal-semiconductor Schottky diode,” Journal of The Electrochemical Society, vol.154, 2007, pp. J357-J361
- [66] A. Salehi and V. Nazerian, “Characterization of magnetic Ni/n-Si Schottky contact for hydrogen gas sensing applications,” Sensors and Actuators B, vol. 122, 2007, pp. 572–577.
- [67] F. K. Yam, Z. Hassan and A.Y. Hudeish, “The study of Pt Schottky contact on porous GaN for hydrogen sensing,” Thin Solid Films, vol. 515, 2007, pp. 7337-7341.
- [68] J. Huang, W. Hsu, H. Chen, W. Liu, “Comparative study of hydrogen sensing characteristics of a Pd/GaN Schottky diode in air and N<sub>2</sub> atmospheres,” Sensors and Actuators B, vol. 123, 2007, pp.1040-1048
- [69] S. N. Das and A. K. Pal, “Hydrogen sensor based on thin film nanocrystalline n-GaN/Pd Schottky diode,” J. Phys. D: Appl. Phys., vol. 40, 2007, pp. 7291-7297
- [70] F. K. Yam and Z. Hassan, “Schottky diode based on porous GaN for hydrogen gas sensing application,” Applied Surface Science, vol. 253, 2007, pp. 9525-9528
- [71] M. Ali, V. Cimalla , V. Lebedev, H. Romanus, V. Tilak, D. Merfeld, P. Sandvik and O. Ambacher, “Pt/GaN Schottky diodes for hydrogen gas sensors,” Sensors and Actuators B, vol.113, 2006, pp. 797-804.
- [72] T. Tsai, H. Chen, K. Lin, C. Hung, C. Hsu, L. Chen, K. Chu, W. Liu, “Comprehensive study on hydrogen sensing properties of a Pd–AlGaN-based Schottky diode,” International Journal of Hydrogen Energy, vol. 33, 2008, pp. 2986-2992
- [73] M. Miyoshi, Y. Kuraok, K. Asai, T. Shibata, and M. Tanak, “Electrical characterization of Pt/AlGaN/GaN Schottky diodes grown using AlN template and their application to hydrogen gas sensors,” J. Vac. Sci. Technol. B, vol. 25, 2007, pp. 1231-1235
- [74] C. Pandis, N. Brilis, E. Bourithis, D. Tsamakis, H. Ali, S. Krishnamoorthy, A. A. Iliadis and M. Kompitsas, “Low–temperature hydrogen sensors based on Au nanoclusters and Schottky contacts on ZnO films deposited by pulsed laser deposition on Si and SiO<sub>2</sub> substrates,” IEEE Sensors Journal, vol. 7, 2007. pp. 562-564
- [75] W. M. Tang, P. T. Lai, J. P. Xu and C. L. Chan, “Enhanced hydrogen-sensing characteristics of MISiC Schottky-diode hydrogen sensor by trichloroethylene

- oxidation,” *Sensors and Actuators A*, vol. 119, 2005, pp. 63-67
- [76] S. Nakagomi, K. Okuda and Y. Kokubun, “Electrical properties dependent on H<sub>2</sub> gas for new structure diode of Pt–thin WO<sub>3</sub>–SiC,” *Sensors and Actuators B*, vol. 96, 2003, pp. 364-371
- [77] W. Liu, P. Pan, H. Chen, K. Lin, S. Chen and K. Yu, “Hydrogen-sensitive characteristics of a novel Pd/InP MOS Schottky diode hydrogen sensor,” *IEEE Transactions On Electron Devices*, vol. 48, 2001, pp. 1938-1944
- [78] K. Lin, H. Chen, H. Chuang, C. Chen, C. Lu, C. Cheng, and W. Liu, “Characteristics of Pd/InGaP Schottky Diodes Hydrogen Sensors,” *IEEE Sensors Journal*, vol. 4, 2004, pp. 72-79
- [79] Y. Tsai, C. Cheng, P. Lai, S. Fu, C. Hong, H. Chen and W. Liu, “Comprehensive study of hydrogen sensing characteristics of Pd metal–oxide–semiconductor (MOS) transistors with Al<sub>0.24</sub>Ga<sub>0.76</sub>As and In<sub>0.49</sub>Ga<sub>0.51</sub>P Schottky contact layers,” *Sensors and Actuators B*, vol. 120, 2007, pp. 687-693
- [80] Y. Irokawa, Y. Sakuma, and T. Sekiguchi, “Effect of dielectrics on hydrogen detection sensitivity of metal–insulator–semiconductor Pt–GaN diodes,” *Japanese Journal of Applied Physics*, vol. 46, 2007, pp. 7714-7716
- [81] H. J. Pan, K. W. Lin, K. H. Yu, C. C. Cheng, K. B. Thei, W. C. Liu, and H. I. Chen, “Highly hydrogen-sensitive Pd/InP metal-oxide-semiconductor Schottky diode hydrogen sensor,” *Electronics Letter*, vol. 38, 2002, pp. 92-94
- [82] O. Weidemann, M. Hermann, and G. Steinhoff, H. Wingbrant and A. Lloyd Spetz, M. Stutzmann and M. Eickhoff, “Influence of surface oxides on hydrogen-sensitive Pd:GaN Schottky diodes,” *Applied Physics Letters*, vol. 83, 2003, pp. 773-775
- [83] S. Nakagomi, T. Shida, H. Hoshi and Y. Kokubun, “Field-effect hydrogen sensor device with floating gate exhibiting unique behavior,” *Sensors and Actuators B*, vol. 125, 2007, pp. 408-414
- [84] K. Tsukada, T. Yamaguchi, and T. Kiwa, “A Proton Pumping Gate Field-Effect Transistor for a Hydrogen Gas Sensor,” *IEEE Sensors Journal*, vol. 7, 2007, pp. 1268-1269
- [85] S. Kandasamy, W. Wlodarski, A. Holland, S. Nakagomi and Y. Kokubun, “Electrical characterization and hydrogen gas sensing properties of a n-ZnO/p-SiC Pt-gate metal semiconductor field effect transistor,” *Applied Physics Letters*, vol. 90, 2007, pp. 064103
- [86] K. Tsukada, T. Kiwa, T. Yamaguchi, S. Migitaka, Y. Goto and K. Yokosawa, “A study of fast response characteristics for hydrogen sensing with platinum FET sensor,” *Sensors and Actuators B*, vol. 114, 2006, pp. 158-163

- [87] K. Yokosawa, K. Saitoh, S. Nakano, Y. Goto and K. Tsukada, "FET hydrogen-gas sensor with direct heating of catalytic metal," *Sensors and Actuators B*, vol. 130, 2008, pp. 94-99
- [88] T. Yamaguchi, T. Kiwa, K. Tsukada, K. Yokosawa, "Oxygen interference mechanism of platinum-FET hydrogen gas sensor," *Sensors and Actuators A*, vol. 136, 2007, pp. 244-248
- [89] C. Cheng, Y. Tsai, K. Lin, H. Chen, W. Hsu, C. Hong, W. Liu, "Characteristics of a Pd-oxide-In<sub>0.49</sub>Ga<sub>0.51</sub>P high electron mobility transistor (HEMT)-based hydrogen sensor," *Sensors and Actuators B*, vol. 113, 2006, pp. 29-35
- [90] Y. Tsai, K. Lin, H. Chen, C. Hung, T. Chen, T. Tsai, L. Chen, K. Chu and W. Liu, "Comprehensive study of a Pd/Al<sub>0.24</sub>Ga<sub>0.76</sub>As-based field-effect-transistor-type hydrogen sensor," *Sensors and Actuators B*, vol. 133, 2008, pp. 128-134
- [91] Y. Y. Tsai, C. C. Cheng, P. H. Lai, S. Fu, C. W. Hong, H. I. Chen and W. C. Liu, "Comprehensive study of hydrogen sensing characteristics of Pd metal-oxide-semiconductor (MOS) transistors with Al<sub>0.24</sub>Ga<sub>0.76</sub>As and In<sub>0.49</sub>Ga<sub>0.51</sub>P Schottky contact layers," *Sensors and Actuators B*, vol. 120, 2007, pp. 687-693
- [92] P. Andrei, L. L. Fields, J. P. Zheng, Y. Cheng and P. Xiong, "Modeling and simulation of single nanobelt SnO<sub>2</sub> gas sensors with FET structure," *Sensors and Actuators B*, vol. 128, 2007, pp. 226-234
- [93] C. Hung, H. Chang, Y. Tsai, P. Lai, S. Fu, T. Chen, H. Chen, and W. Liu, "Study of a new field-effect resistive hydrogen sensor based on a Pd/Oxide/AlGaAs transistor," *IEEE Transactions on Electron Devices*, vol. 52, 2007, pp. 1224-1231
- [94] C. Hung, K. Lin, H. Chang, Y. Tsai, P. Lai, S. Fu, Tz. Chen, H. Chen and W. Liu, "Three-terminal-controlled field-effect resistive hydrogen sensor," *Sensors and Actuators B*, vol. 124, 2007, pp. 549-556
- [95] A. Z. Sadek, C. O. Baker, D. A. Powell, W. Wlodarski, R. B. Kaner and K. Kalantar-zadeh, "Polyaniline Nanofiber based surface acoustic wave gas sensors—effect of nanofiber diameter on H<sub>2</sub> response," *IEEE Sensors J.*, vol. 7, 2007, pp. 213-218.
- [96] W. Jakubik, M. Urbanczyk and E. Maciak, "Metal-free phthalocyanine and palladium sensor structure with a polyethylene membrane for hydrogen detection in SAW systems," *Sensors and Actuators B*, vol. 127, 2007, pp. 295-303
- [97] A. Z. Sadek, W. Wlodarski, K. Shin, R. B. Kaner and K. Kalantar-zadeh, "A polyaniline/WO<sub>3</sub> nanofiber composite-based ZnO/64° YX LiNbO<sub>3</sub> SAW hydrogen gas sensor," *Synthetic Metals*, vol. 158, 2008, pp. 29-32
- [98] A. Z. Sadek, W. Wlodarski, Y. X. Li, W. Yu, X. Li, X. Yu and K. Kalantar-zadeh, "A ZnO nanorod based layered ZnO/64° YX LiNbO<sub>3</sub> SAW hydrogen gas sensor," *Thin Solid*

- Films, vol. 515, 2007, pp. 8705-8708
- [99] S. J. Ippolito, S. Kandasamy, K. Kalantar-zadeh, W. Wlodarski and A. Holland, "Comparison between conductometric and layered surface acoustic wave hydrogen gas sensors," *Smart Mater. Struct.*, vol. 15, 2006, pp. S131–S136
  - [100] W. P. Jakubik, "Investigations of thin film structures of WO<sub>3</sub> and WO<sub>3</sub> with Pd for hydrogen detection in a surface acoustic wave sensor system," *Thin Solid Films*, vol. 515, 2007, pp. 8345-8350
  - [101] R. R. J. Maier, B. J. S. Jones, J. S. Barton, S. McCulloch, T. Allsop, J. D. C. Jones and I. Bennion, "Fiber optics in palladium-based hydrogen sensing," *J. Opt. A: Pure Appl. Opt.*, vol. 9, 2007, pp. S45-S59
  - [102] D. Luna-Moreno, D. Monzon-Hernandez, J. Villatoro and G. Badenes, "Optical fiber hydrogen sensor based on core diameter mismatch and annealed Pd–Au thin films," *Sensors and Actuators B*, vol. 125, 2007, pp. 66-71
  - [103] Z. Zhao, M.A. Carpenter, H. Xia and D. Welch, "All-optical hydrogen sensor based on a high alloy content palladium thin film," *Sensors and Actuators B*, vol. 113, 2006, pp. 532-538
  - [104] D. Luna-Moreno and D. Monzon-Hernandez, "Effect of the Pd–Au thin film thickness uniformity on the performance of an optical fiber hydrogen sensor," *Applied Surface Science*, vol. 253, 2007, pp. 8615-8619
  - [105] J. Villatoro and D. Monzon-Hernandez, "Fast detection of hydrogen with nano fiber tapers coated with ultra thin palladium layers," *Optics Express*, vol. 13, 2005, pp. 5087-5092
  - [106] Z. Zhao, M. Knight, S. Kumar, E. T. Eisenbraun and M. A. Carpenter, "Humidity effects on Pd/Au-based all-optical hydrogen sensors," *Sensors and Actuators B*, vol. 129, 2008, pp. 726-733
  - [107] D. Zalvidea, A. Diez b, J. L. Cruz and M.V. Andres, "Hydrogen sensor based on a palladium-coated fiber-taper with improved time-response," *Sensors and Actuators B*, vol. 114, 2006, pp. 268-274
  - [108] J. Villatoro, A. Diez, J. L. Cruz, and M. V. Andres, "In-Line Highly Sensitive Hydrogen Sensor Based on Palladium-Coated Single-Mode Tapered Fibers," *IEEE Sensors Journal*, vol. 3, 2003, pp. 533-537
  - [109] K. T. Kim, H. S. Song, J. P. Mah, K. B. Hong, K. Im, S. J. Baik, and Y. I. Yoon, "Hydrogen sensor based on palladium coated side-polished single-mode fiber," *IEEE Sensors Journal*, vol. 7, no. 12, 2007, pp. 1767-1771

- [110] M. Buric, K. P. Chen, M. Bhattarai, P. R. Swinehart and M. Maklad, "Active fiber Bragg grating hydrogen sensors for all-temperature operation," IEEE Photonics Technology Letters, vol. 19, 2007, pp. 255-257.
- [111] C. Caucheteur, M. Debligny, D. Lahem, and P. Megret, "Catalytic fiber bragg grating sensor for hydrogen leak detection in air," IEEE Photonics Technology Letters, vol. 20, 2008, pp. 96-98
- [112] W. Hsu, C. Chan, C. Peng and C. Chang, "Hydrogen sensing characteristics of an electrodeposited WO<sub>3</sub> thin film gasochromic sensor activated by Pt catalyst," Thin Solid Films, vol. 516, 2007, pp. 407-411
- [113] M. Ranjbar , A. I. Zad and S M Mahdavi, "Gasochromic tungsten oxide thin films for optical hydrogen sensors," J. Phys. D: Appl. Phys., vol. 41, 2008, pp. 055405
- [114] D. Iannuzzi, S. Deladi, M. Slamaa, J. H. Rector, H. Schreuders and M. C. Elwenspoek, "A fiber-top cantilever for hydrogen detection," Sensors and Actuators B, vol. 121, 2007, pp. 706-708
- [115] Y. Chou, H. Chiang and C. Wang, "Study on Pd functionalization of microcantilever for hydrogen detection promotion," Sensors and Actuators B, vol.129, 2008, pp. 72-78
- [116] D. R. Baselt, B. Fruhberger, E. Klaassena, S. Cemalovic, C. L. Britton, S. V. Patel, T. E. Mlsna, D. McCorkle and B. Warmack, "Design and performance of a microcantilever-based hydrogen sensor," Sensors and Actuators B, vol.88, 2003, pp. 120-131
- [117] C. C. Lu, Z. Chen and K. Saito, "Hydrogen sensors based on Ni/SiO<sub>2</sub>/Si MOS capacitors," Sensors and Actuators B, vol. 122, 2007, pp. 556-559
- [118] L. Yadav, N. C. Gupta, R. Dwivedi, R. S. Singh, "Sensing behavior and mechanism of titanium dioxide-based MOS hydrogen sensor," Microelectronics Journal, vol. 38, 2007, pp.1226-1232
- [119] R. Loloee, B. Chorpening, S. Beer and R. N. Ghosh, "Hydrogen monitoring for power plant applications using SiC sensors," Sensors and Actuators B, vol. 129, 2008, pp. 200-210
- [120] F. Qiu, W. Shin, M. Matsumiya, N. Izu, I. Matsubara and N. Murayama, "Miniaturization of thermoelectric hydrogen sensor prepared on glass substrate with low-temperature crystallized SiGe film," Sensors and Actuators B, vol. 103, 2004, pp. 252-259
- [121] K. Tajima, F. Qiu, W. Shin, N. Izu, I. Matsubara and N. Murayama, "Micromechanical fabrication of low-power thermoelectric hydrogen sensor," Sensors and Actuators B, vol. 108, 2005, pp. 973-978



- [122] L. F. Houlet, W. Shin, K. Tajima, M. Nishibori, N. Izu, T. Itoh, I. Matsubara, "Thermopile sensor-devices for the catalytic detection of hydrogen gas," *Sensors and Actuators B*, vol. 130, 2008, pp. 200-206
- [123] K. Tajima, Y. Choi, W. Shin, N. Izu, I. Matsubara, and N. Murayama, "Micro-thermoelectric hydrogen sensors with Pt thin film and Pt/Alumina thick film catalysts," *Journal of The Electrochemical Society*, vol.153, 2006, pp. H58-H62
- [124] Ç. Kihc and A. Zunger, "Origins of coexistence of conductivity and transparency in  $\text{SnO}_2$ ," *Phys. Rev. Lett.*, vol 88, 2002, pp. 095501
- [125] A. K. Singh, A. Janotti, M. Scheffler, and C. G. Van de Walle, "Sources of electrical conductivity in  $\text{SnO}_2$ ," *Phys. Rev. Lett.*, vol. 101, 2008, pp. 055502,
- [126] M. N. Rumyantseva, O. V. Safonova, M. N. Boulova, L. I. Ryabova, and A. M. Gaskov, "Dopants in nanocrystalline tin dioxide," *Russian Chemical Bulletin, International Edition*, vol. 52, 2003, pp. 1217-1238
- [127] A Oprea, N Barsan and U Weimar, "Characterization of granular metal oxide semiconductor gas sensitive layers by using Hall effect based approaches," *J. Phys. D: Appl. Phys.*, vol. 40, 2007, pp. 7217-7237
- [128] W. Gopel, and K. D. Schierbaum, " $\text{SnO}_2$  sensors: current stats and future aspects," *Sensors and Actuators B*, vol. 26, 1995, pp. 1-12
- [129] N. Barsan, M. S. Berberich, and W. Gopel, "Fundamental and practical aspects in the design of nanoscaled  $\text{SnO}_2$  gas sensors: a status report," *Fresenius J, Anal Chem*, vol. 365, 1999, pp. 287-304
- [130] N. Barsan, D. Koziej and U. Weimar, "Metal oxide-based gas sensor research: How to?," *Sensors and Actuators B*, vol. 121, 2007, pp. 18-35
- [131] N. Barsan and U. Weimar, "Conduction model of metal oxide gas sensors," *Journal of Electroceramics*, vol. 7, 2001, pp.143-167
- [132] Patrick Reichel, "Development of a chemical gas sensor system", PhD Dissertation, 2005, pp. 25
- [133] A. Oprea, E. Moretton, N. Barsan, W. J. Becker, J. Wollenstein and U. Weimar, "Conduction model of  $\text{SnO}_2$  thin films based on conductance and Hall effect measurements," *Journal of Applied Physics*, vol. 100, 2006, pp. 033716
- [134] S. Shukla, P. Zhang, H. J. Cho, Z. Rahman, C. Drake, Sudipta Seal, V. Craciun and L. Ludwig, "Hydrogen-discriminating nanocrystalline-doped tin oxide room-temperature Microsensor," *Journal of Applied Physics*, vol, 98, 2005, pp. 104306

- [135] S. Shukla, P. Zhang, H. J. Cho, S. Seal, and L. Ludwig, "Room temperature hydrogen response kinetics of nano–micro-integrated doped tin oxide sensor," *Sensors and Actuators B*, vol. 120, 2007, pp. 573-583
- [136] Z. Ji, Z. He, Y. Song, K. Liu and Z. Ye, "Fabrication and characterization of indium-doped p-type SnO<sub>2</sub> thin films," *Journal of Crystal Growth*, vol. 259, 2003, pp. 282-285
- [137] Z. Ji, L. Zhao, Z. He, Q. Zhou and C. Chen, "Transparent p-type conducting indium-doped SnO<sub>2</sub> thin films deposited by spray pyrolysis," *Materials Letters*, vol. 60, 2006, pp.1387-1389
- [138] S. Shukla, S. Seal, L. Ludwig and C. Parish, "Nanocrystalline indium oxide-doped tin oxide thin film as low temperature hydrogen sensor," *Sensors and Actuators B*, vol. 97, 2004, pp. 256-265
- [139] C. Drake, A. Amalu, J. Bernard, and S. Seal, "Enhancing the low temperature hydrogen sensitivity of nanocrystalline SnO<sub>2</sub> as a function of trivalent dopants," *Journal of Applied Physics*, vol. 101, 2007, pp. 104307
- [140] S. Shukla, P. Zhang, Hyoungh J. Cho, L. Ludwig and S. Seal, "Significance of electrode-spacing in hydrogen detection for tin oxide-based MEMS sensor," *International Journal of Hydrogen Energy*, vol. 33, 2008, pp. 470-475
- [141] C. Drake, S. Deshpande, and S. Seal, "Determination of free carrier density and space charge layer variation in nanocrystalline In<sup>3+</sup> doped tin oxides using Fourier transform infrared spectroscopy," *Applied Physics Letters*. vol.89, 2006, pp.143116
- [142] C. Drake and S. Seal, "Band gap energy modifications observed in trivalent In substituted nanocrystalline SnO<sub>2</sub>," *Applied Physics Letters*, vol. 90, 2007, pp. 233117
- [143] J. Ding, T. J. McAvoy, R. E. Cavicchi and S. Semancik, "Surface state trapping models for SnO<sub>2</sub>-based micro hotplate sensors," *Sensors and Actuators B*, vol. 77, 2001, pp. 597-613
- [144] C. Xu, J. Tamaki, N. Miura, N. Yamazoe, "Relationship between gas sensitivity and microstructure of porous SnO<sub>2</sub>," *J. Electrochem. Soc. Jpn.*, vol. 58, 1990, pp. 1143-1148.
- [145] H. Ogawa, M. Nishikawa, A. Abe, "Hall measurement studies and an electrical conduction model of tin oxide ultrafine particle films," *Journal of Applied Physics*, vol. 53, 1982, pp. 4448-4455.
- [146] S. Capone, P. Siciliano, F. Quaranta, R. Rella, M. Epifani and L. Vasanelli, "Moisture influence and geometry effect of Au and Pt electrodes on CO sensing response of SnO<sub>2</sub> microsensors based on sol-gel thin film," *Sensors and Actuators B*, vol. 77, 2001, pp. 503-511

- [147] J. W. Gardner, "A diffusion-reaction model of electrical conduction in tin oxide gas sensor", *Semicond. Sci.*, vol. 4, 1995, pp. 345-350.
- [148] J. W. Gardner, "Intelligent gas sensing using an integrated sensor pair", *Sensors and Actuators B*, vol. 26-27, 1995, pp. 261-266.
- [149] X. Vilanova, E. Llobet, J. Brezmes, J. Calerer and X. Correig, "Numerical simulation of the electrode geometry and position effects on semiconductor gas sensor response," *Sensors and Actuators B*, vol. 48, 1998, pp. 425-431
- [150] W. M. Otter, "Approximate expressions for the capacitance and electrostatic potential of interdigitated electrodes," *Sensors and Actuators A*, vol. 96, 2002, pp. 140-144
- [151] J. Tamaki, A. Miyaji, J. Makinodan, S. Ogura, S. Konishi, "Effect of micro-gap electrode on detection of dilute NO<sub>2</sub> using WO<sub>3</sub> thin film microsensors," *Sensors and Actuators B*, vol. 108, 2005, pp. 202-206
- [152] H. Takahashi and J. Mizuguchi, "Carrier generation and carrier determination in dipyrroldiketopyrrolopyrrole-based H<sub>2</sub> gas sensors," *Journal of Applied Physics*, vol. 100, 2006, pp. 034908
- [153] J. Tamaki, A. Miyaji, I. Makinodan, S. Ogura, S. Konishi, "Effect of micro-gap electrode on detection of dilute NO<sub>2</sub> using WO<sub>3</sub> thin film microsensors", *Sensors and Actuators B*, vol. 108, 2005, pp. 202-206
- [152] S. Rosini and E. Eiebert, "Electrochemical sensors for detection of hydrogen in air: model of non-Nernstian potentiometric response of platinum gas diffusion electrodes," *Electrochimica Acta*, vol. 50, 2005, pp. 2943-2953
- [153] S. Capone, P. Siciliano, F. Quaranta, R. Rella, M. Epifani, L. Vasanelli, "Moisture influence and geometry effect of Au and Pt electrodes on CO sensing response of SnO<sub>2</sub> microsensors based on sol-gel thin film", *Sensors and Actuators B*, vol. 77, 2001, pp. 503-511,
- [154] M. Batzill and U. Diebold, "Characterizing solid state gas responses using surface charging in photoemission: water adsorption on SnO<sub>2</sub>(101)," *J. Phys.: Condens. Matter*, vol. 18, (2006, pp. L129-L134
- [155] Q. Kuang, C. Lao, Z. Wang, Z. Xie, and L. Zheng, "High-sensitivity humidity sensor based on a single SnO<sub>2</sub> nanowire," *J. AM. CHEM. SOC.*, vol. 129, 2007, pp. 6070-6071
- [156] Y. Shimizu, E. Kanazawa, Y. Takao, M. Egashir, "Modification of H<sub>2</sub>-sensitive breakdown voltages of SnO<sub>2</sub> varistor with noble metals," *Sensors and Actuators B*, vol. 52, 1998, pp. 38-44
- [157] T. D. Senguttuvan, R. Rai and S. T. Lakshmikumar, "Gas sensing properties of lead doped tin oxide thick films," *Materials Letters*, vol. 61, 2007, pp. 582-584